Imaging Interfaces in Epitaxial Heterostructures

by

Codrin N. Cionca

A dissertation submitted in partial fulfillment
of the requirements for the degree of
Doctor of Philosophy
(Applied Physics)
in The University of Michigan
2005

Doctoral Committee:

Professor Roy Clarke, Chair
Professor Brad Orr
Associate Professor Joanna Mirecki Millunchick
Associate Professor Çağliyan Kurdak
Associate Professor Fred L.Terry

ACKNOWLEDGEMENTS

If I wanted to be fair to all of you to whom, in one way or another, I owe a great deal of gratitude for helping me reaching this moment, I would have to dedicate a serious chapter just to mention it. Therefore, please don't take it as unkindness if the format constrains me to omit your names–I'm still gratefull for your support, wit and wisdom that were perhaps crucial at the right time.

I want to thank the members of my committee, Brad Orr, Joanna Mirecki Millunchick, Cağliyan Kurdak and Fred L.Terry for their effort, help and valuable suggestions. Gratitude is perhaps a too narrow concept to express what I owe my advisor, Roy Clarke, for the opportunities and chances he offered, for his faith in me and for making my PhD the experience that I will probably relish for the rest of my life.

I want to thank professor Yizhak Yacoby for his valuable help and, most important, for inspiring me. And special thanks to scientific staff of sector 7 at APS, especially Don Walko, for their knowledge, patience and sense of humor when most needed.

Use of the Advanced Photon Source was supported by the U. S. Department of Energy, Office of Science, Office of Basic Energy Sciences, under Contract No. W-31-109-Eng-38. This work was conducted at the MHATT-CAT insertion device beamline at the Advanced Photon Source and was supported in part by the U.S. Department of Energy, Grants No. DE-FG02-03ER46023.

TABLE OF CONTENTS

LIST OF FIGURES

Figure

LIST OF TABLES

Table

LIST OF APPENDICES

Appendix

CHAPTER I

Introduction

1.1 The Phase Problem

X–ray diffraction has been a major tool for determination of crystal structure for nearly one hundred years. However, there is no general solution whereby the scattering data can be directly inverted to determine the real space structure (i.e. atomic position). This is the so–called *phase problem* of x-ray scattering.

In this thesis we present the application of a novel solution to the phase problem for two–dimensional (2D) crystal structures. The class of 2D structures is important because it includes most of the materials that are relevant to electronic heterostructures such as epitaxial thin films and superlattices.

In many cases we only have access, through our measurements, to the squared magnitude of the Fourier transform of the structure factor. If the phase could be measured, the structural information could be obtained by a simple inverse Fourier transform. In crystallography, the quantity that we usually need to determine is the electron density (ED).

Unfortunately, in the vast majority of the situations, the phase values are not accessible experimentally. In the case of x-ray diffraction, the frequency of the scattered wave–$\sim 2.4 \times 10^{18}$ Hz for a photon with E=10 keV–makes the time-resolved solu-

tion several orders of magnitude beyond the present capabilities of coherent beam control [3, 4]. The question becomes, thus, whether the phase values of the scattered wave can be reconstructed relying on all the information that can be acquired experimentally.

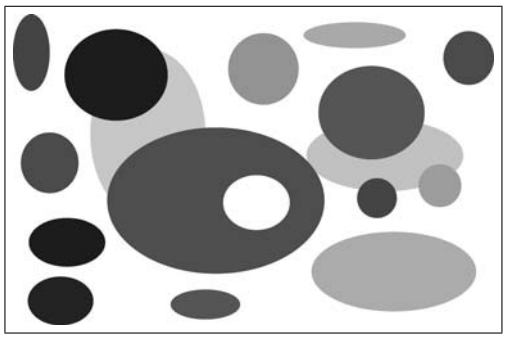

(a) Amplitudes of the circles and phases of circles

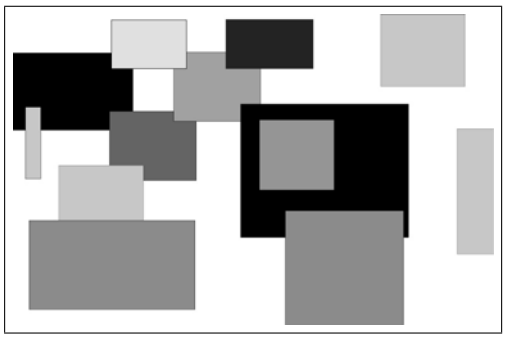

(b) Amplitudes of the rectangles and phases of rectangles

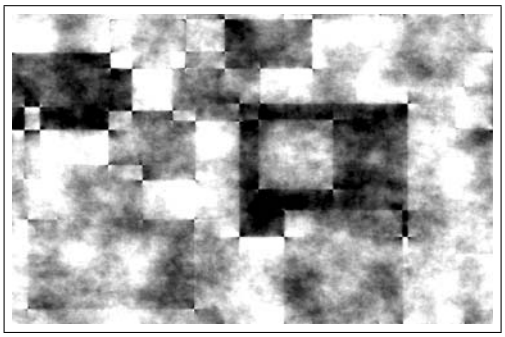

(c) Amplitudes of the circles and phases of rectangles

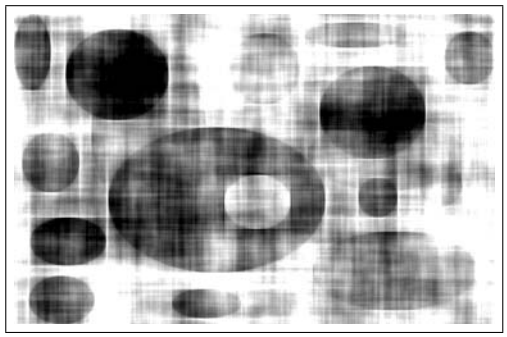

(d) Amplitudes of the rectangles and phases of circles

Figure 1.1: The initial (a,b) and phase swapped (c,d) images

A visual example that illustrates the importance of the phase in an experiment where data is only measured in the form of amplitude was described first in Ref. [5] and it is presented in Figures 1.1(a)–1.1(d). In Fig.1.1(a) and Fig.1.1(b) we have the initial images,*circles* and *rectangles*, both with same number of pixels. Next, we take the Fourier transform and separate the amplitudes from the phases.

$$\mathscr{F}(circles) = Amplitude(circles) \times e^{i\Phi(circles)} \tag{1.1}$$

$$\mathscr{F}(rectangles) = Amplitude(rectangles) \times e^{i\Phi(rectangles)} \tag{1.2}$$

With these results we build two images, as follows: in Fig.1.1(c)–the inverse Fourier transform of $Amplitude(circles) \times e^{i\Phi(rectangles)}$ and in Fig.1.1(d)–the back Fourier transform of $Amplitude(rectangles) \times e^{i\Phi(circles)}$.

It is obvious that most of the visual information follows the phase term and not the amplitude. Measuring the amplitude brings up a lot of information but the determinant factor seems, unfortunately, to be the unknown phase. The conundrum is more than graphical. It might be hard to accept, but the vast majority of the knowledge we have gotten through x-ray scattering since this technique was properly established by Bragg came only through amplitude measurements. In the case of simple structures, or where an *ansatz* is readily available, this proved to be sufficient to determine the atomic positions. But in the case of complex structures (biomolecules, for example) or when a relatively simple structure suffers a complicated local distortion-as in the case of ferroelectrics studied here, additional information is required to properly characterize the structure–thus motivating the need to solve the phase problem.

1.2 Solutions of the Problem

There are several ways of determining the phase of a scattered x-ray in crystallography. For their impact on structural science, a few of them were awarded the Nobel prize. Ironically, none of the them was in Physics.

Historically, the first way of retrieving the phase values was by way of an educated guess. This method was employed in certain famous studies, like the discovery of the double helix structure of the DNA (Nobel Prize in Physiology/Medicine, 1962) [6].

Patterson maps are the Fourier transform of the intensity of the diffraction pattern. Corroborated with Harker's observation on the centrosymmetry of the unit

cell [7, 8], their use allowed the identification of the positions of certain atoms in the crystal (usually the heavy ones), easy to spot due to their high scattering factor. The requirement was that at least one atom was much heavier than the rest. Examples might be organic molecules with one or more metals or S, Cl or Br. The Patterson maps were used to locate the heavy atoms and calculate the complex structure factors (CSFs) of the structures generated with them only. Because the heavy ions contributed most in setting the phase, the remaining atoms usually appeared in the electron density (ED) maps obtained after the inverse Fourier transform using the complete amplitudes. The method was used by Hodgkin (Nobel Prize in Chemistry, 1964) to determine the structure of the vitamin B12, a real *tour de force* for the capabilities of those times [9, 10, 11, 12]. Cobalt was successfully used for the calculation of phases [13].

A method for phase retrieval was developed by Max Perutz and John Kendrew, in Cambridge (Nobel Prize in Chemistry, 1962). In this method, a macromolecule crystal is prepared in the normal way (the parent) and next with a small number of heavy atoms bound to the molecules in a very specific and reproducible way that also preserves the crystallinity of the sample (the derivative). This method is usually referred to as *isomorphous replacement* . The structure factor of the derivative is the sum of the structure factor F_{ph} of the parent F_p and the structure factor of the heavy atoms, as depicted in Fig.1.2. To find the total complex structure factor Perutz used the Harker diagrams–the first use of the complex plane graphic representation in the phase problem–in a very original way. He constructed a circle centered at the origin with radius F_p, known from the intensity of the scattered wave on the *parent* crystal. The complex value of F_h was determined using the Patterson map algorithm. Another circle centered at the end of the complex F_h was constructed,

Figure 1.2: Isomorphous scattering diagram

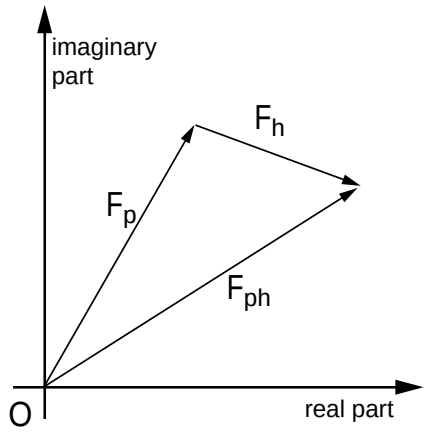

Figure 1.3: Perutz solution using isomorphous replacement

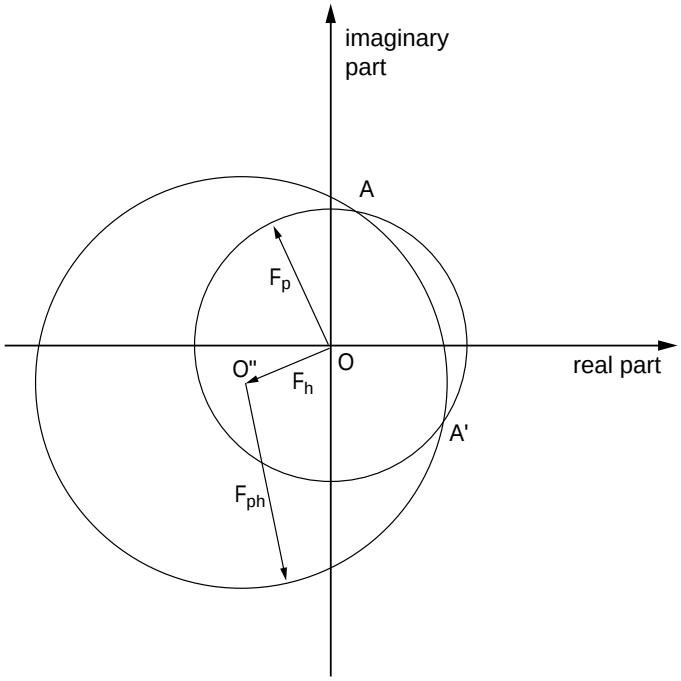

with radius F_{ph}, known from scattering on the *derivative* crystal. The complex value of the parent structure factor is given by one of the intersections of the circles in A and A'. The ambiguity is usually resolved using double or multiple isomorphous replacements.

X-ray sources have evolved greatly over time and the capability of tuning the photon energy offered by the synchrotron sources allowed measurements above and below the atomic absorption edge for heavier atoms in the molecule. Since the scattering factors vary dramatically around the absorption edge, the case is similar to that of a substitution. The anomalous scattering data is treated in the same way as in the case of isomorphous replacement.

Direct structure determination methods emerged as more computational power became accessible to x–ray researchers. The central concept is to assign an entropy value to a structure and then, of all possible configurations, to chose the one with that maximizes the entropy. The method works well for bulk structure with moderate unit cell sizes (up to a few thousand atoms) but computation becomes difficult when the molecular size increases beyond that. For their work on the direct method, Hauptman and Karle were awarded the Nobel Prize in Chemistry in 1985.

Given the focus of this thesis, we must mention that there have also been attempts to use Bayes theorem and the maximum entropy approach in solid state diffraction [14]. Structural biology nowadays uses various methods of phase retrieval, all of them integrating one or more of the following: direct method, anomalous scattering and/or isomorphous replacements [15, 16].

1.3 Holographic Reference

Of particular interest to the study presented in this thesis is the concept of a *holographic reference*. The idea originates back in the late forties when Gabor discovered holography [17]. It assumes that the scattering of the structure to be determined can interfere with the scattered wave from a known structure–which becomes, thus, the reference wave:

$$A_{total} = A_{ref} + A_{unknown} \tag{1.3}$$

The concept was translated to atomic resolution [18, 19] and attempts have been made to employ this method using both electron [20, 21] and X-ray diffraction. As a reference, fluorescence photons generated in atoms with known positions can be used [22, 23, 24, 25]. The recorded signal represents the interference function of the reference wave and the wave scattered from the unknown structure. Starting from the known positions of the fluorescence atoms it is possible to extract structural information about surface reconstruction or atomic displacements in the unit cell.

1.4 Synchrotron Radiation

At the present time, it is impossible to imagine a serious x–ray surface diffraction experiment without at least considering the possibility of using synchrotron radiation. Theorists postulated the mechanisms involved in generation of synchrotron radiation toward the end of the nineteenth century. However, the first machine capable of generating x-ray synchrotron radiation appeared only after World War II with the development of the charged particle accelerators. High energy electron accelerators have emerged as reliable synchrotron light sources. As the speed of charged particles approaches the speed of light, the radiation is emitted in a narrow, forward oriented cone [26]. In the early stages, the synchrotron light sources used photons created

as an otherwise undesired effect in handling high energy particles. As a significant advance, the development of *storage rings* has to be mentioned as they constitute the basis of the modern sources. In a storage ring, the beam circulates continuously at a fixed energy for a large period of time (hours). This means much longer beam times, higher beam currents and thus higher photon fluxes. The use of synchrotron radiation was a parasitic activity for a very long time as the main purpose of the rings was particle physics rather than synchrotron radiation. But this showed such promise–for example [27]–that eventually triggered the initiative to build accelerators for the sole purpose of generating synchrotron radiation. These were the second generation sources.

Their impact was enormous. Angle-resolved photoemission, extended x-ray absorption fine-spectroscopy (EXAFS) and high resolution protein crystallography defined themselves as distinct research directions due to the access to very bright x–ray beams.

The next generation was marked by the invention of insertion devices, wigglers and undulators. This triggered the construction of third generation sources, giant machines with a diameter of ~ 1 km [28]. The Advanced Photon Source, where much of this thesis research was carried out, is one of these third generation synchrotron light sources.

CHAPTER II

Coherent Bragg Rod Analysis

2.1 Surface Diffraction and Bragg Rods

In general, using the current crystallographic techniques mentioned in section 1.2, it is almost trivial to solve bulk structures with 100–200 atomic sites. The phases do not need to be known with a very high accuracy; a root-mean-square error of $10-20^{\circ}$ allows a precision of the order of the 0.1 Å in the final electron density (ED) map [29]. These techniques rely primary on locating the position of the Bragg points of a three dimensional (3D) periodic structure.

Surface diffraction, however, is a totally different story. The amount of material is infinite and periodic in only two directions (in–plane). In the third direction (normal to the surface), the sample is in general confined and lacks a periodic structure. Therefore, the intensity of the scattering pattern along this direction is expected to be significantly weaker than that of Bragg peaks, commonly by 8 orders of magnitude or more.

In this type of reconstruction, the morphology of adsorbates is an important factor in surface diffraction experiments. A bulk sample only rarely changes structure over time; unfortunately, the same thing cannot be said about the surface. Thin film or surface samples are also very sensitive to monolayer contamination, where the

Figure 2.1: Sample structure

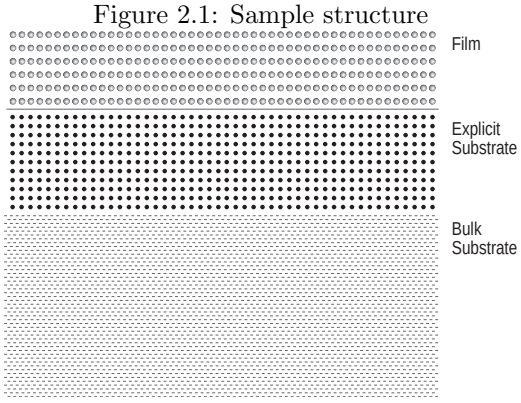

contaminant is usually poorly, if at all, ordered.

Epitaxially grown thin films have emerged as a class of materials with properties significantly different than those of the bulk materials. Obtaining structural information thus becomes crucial in understanding their behavior. In spite of the aforementioned difficulties, several methods have been developed to investigate them.

The structure factor [30] of an atomic assembly can be written as:

$$\mathcal{F}(\vec{q}) = \int_V \rho(\vec{r}) e^{i\vec{q}\cdot\vec{r}} d^3r \tag{2.1}$$

where ρ is the electronic density, $\vec{r}$ is the position vector in real space, $\vec{q}$ the position vector in the reciprocal space and the integral is over the whole volume of the sample. The experimental configuration we want to consider is that of a semi-infinite crystal (substrate) with a thin film deposited on top. Three regions can be distinguished: the film, the top part of the substrate and the remaining part of the bulk substrate. The film and the upper layers of the substrate are regarded as an assembly of explicitly described individual atoms. For the remaining bulk substrate, the structure factor is calculated regarding it as a semi infinite crystal with atoms in the ideal lattice.

$$\mathcal{F}_{total} = \mathcal{F}_{bulk} + \mathcal{F}_{exp\_subs} + \mathcal{F}_{film} \tag{2.2}$$

In general, a crystal can be represented as a regular lattice. If we consider the

structural behavior in the presence of an interface, we must allow a certain amount of distortion such as broadening of the ED, splittings in the atomic positions due to domain formation, partial occupancy, and modified atomic scattering factors as due to diffusion and lattice disorder. If we assume that a system with lattice constant $\vec{a} = [a_x, a_y, a_z]$ is infinite in the x and y directions and confined (N_{uc} unit cells) along z, the general form for the ED will be:

$$\rho(\vec{r}) = \sum_{jx,jy=-\infty}^{+\infty} \sum_{jz=1}^{N_{uc}} \sum_{j_{uc}=1}^{n} [\delta(\vec{R}_{j_x j_y j_z} + \vec{r}_{i_{uc}} - \vec{r}) \circ F_{j_x j_y j_z j_{uc}}(\vec{r})] g(\vec{r} \cdot \vec{e}_z) \tag{2.3}$$

where $\vec{r}$ is the translation vector,

$$\vec{R}_{j_x j_y j_z} = j_x a_x \vec{e}_x + j_y a_y \vec{e}_y + j_z a_z \vec{e}_z \tag{2.4}$$

is the position vector of the lattice cell, n is the number of atoms in the unit cell, $r_{j_{uc}}$ is the position of the i^{th} atom in the unit cell, $F_{j_x j_y j_z j_{uc}}(\vec{r})$ is a general function that describes the ED for each atom and $g(\vec{r} \cdot \vec{e}_z)$ a function that describes the roughness.

In general, when there are no atomic distortions in the lattice, as in the case of the bulk substrate, the form of F is:

$$F_{j_x j_y j_z j_{uc}}(\vec{r}) = f_{j_{uc}} \cdot \delta(\vec{R}_{j_x j_y j_z} + \vec{r}_{j_{uc}} - \vec{r}) \tag{2.5}$$

and thus the electron density becomes:

$$\rho(\vec{r}) = \sum_{jx,jy=-\infty}^{+\infty} \sum_{jz=1}^{N_{uc}} \sum_{j_{uc}=1}^{n} f_{j_{uc}} \delta(\vec{R}_{j_x j_y j_z} + \vec{r}_{i_{uc}} - \vec{r}) g(\vec{r} \cdot \vec{e}_z) \tag{2.6}$$

where $f_{j_{uc}}$ is the atomic scattering factor of the atom j_{uc} in the unit cell.

Since the crystal is infinite in x and y directions, this study will assume that all distortions in the ED will occur along the direction perpendicular to the interface (z). Mathematically, this means:

$$F_{j_x j_y j_z j_{uc}}(\vec{r}) = F_{j_z j_{uc}}(\vec{r} \cdot \vec{e}_z) \tag{2.7}$$

The ED of the film and top part of the substrate for the structure involved in our experiment will be given by Eq.2.3 with $F_{j_x j_y j_z j_{uc}}(\vec{r})$ specified by Eq.2.7. The bulk will follow the particular form of ED described in Eq.2.6. Also, we need to consider the contributions of the Debye–Waller factor.

For a cubic structure, we can express the vectors in the reciprocal space as:

$$\vec{q} = \frac{2\pi}{a_x} Q_x \vec{e}_x + \frac{2\pi}{a_y} Q_y \vec{e}_y + \frac{2\pi}{a_z} Q_z \vec{e}_z; \tag{2.8}$$

with Q_x, Q_y and Q_z the coordinates relative to the reciprocal space unit cell value.

Thus, the expression of the structure factor becomes:

$$\mathcal{F}(Q_x, Q_y, Q_z) = \int_V d^3r \sum_{j_x, j_y = -\infty}^{+\infty} \sum_{j_z=1}^{N_{uc}} \sum_{j_{uc}=1}^{n} [f_{j_{uc} j_z}(\vec{r} \cdot \vec{e}_z) \times \\ \times e^{2\pi i (x_{j_{uc}} Q_x + y_{j_{uc}} Q_y + z_{j_{uc}} Q_z)}] \cdot e^{-\frac{4\pi^2 Q^2}{a^2} <u^2>} \tag{2.9}$$

Because of the infinite size in the x and y directions the scattering is sharp whereas along z the diffraction intensity of the finite size crystal has diffuse streaks between the Bragg points. This scattering pattern is referred to as *Bragg Rod* or *Crystal Truncation Rod (CTR)*. Bragg rods studies can give information about roughness [31], lattice spacing [32], stoichiometry etc.

The Debye–Waller factor will be expressed as:

$$e^{-\frac{4\pi^2 Q^2}{a^2} <u^2>} = e^{\frac{-(2\pi DW_{factor} |\vec{Q}|)^2}{2}} \tag{2.10}$$

with DW_{factor} expressed in reciprocal lattice units^{-1} (RLU^{-1}).

2.2 The COBRA Method

2.2.1 General Presentation of the Method

In a recent study by Yacoby [33] the Bragg rods were successfully used for phase reconstruction in an attempt to create a structural characterization method for thin

films. The Coherent Bragg Rod Analysis (COBRA) was used for characterization of the interfacial structure of a Gd_2O_3 passivation layer with GaAs [34, 35] and for the investigation of ferroelectric behavior of ultrathin films of $PbTiO_3$ epitaxially grown on $SrTiO_3$ [36].

Figure 2.2: Block diagram of analysis procedures

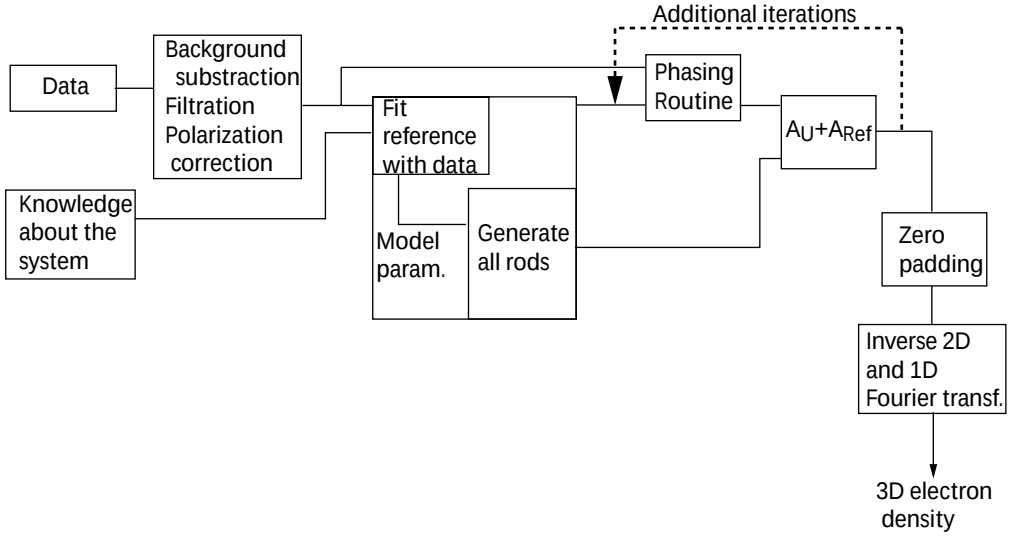

The method derived from the idea of the holographic reference discussed in Section 1.3. The starting point consists of an *ansatz* for the complex structure factor of the sample–which will be referred to as the reference–calculated employing all the information available. The Bragg rods are measured at high data sampling density (100–200 points RLU), and the unknown part of the structure factor is assumed to be slowly varying with reciprocal lattice coordinate relative to that of the reference. Based on this approximation discussed in detail in Section 2.4 the complex structure factor is calculated as the sum of the reference and the phasing correction.

Only a finite range on a finite number of rods can be measured. The indices of a Bragg rod are usually the coordinates of the point where it intersects the plane corresponding to $Q_z = 0$. These coordinates are, of course, integers. To be able to

extract the ED, a volume centered at the origin in reciprocal space is necessary, with a square horizontal profile. Each rod is thus a $Q_xQ_yQ_z$ family of points with indices Q_x, $Q_y \in [-no, no] \cap \mathbf{Z}$ and $Q_z \in [-Q_{z_{max}}, Q_{z_{max}}] \cap \mathbf{R}$. The values of no and $Q_{z_{max}}$ vary from case to case and depend primarly on the number of rods acquired and the maximum accessible range in the vertical direction.

For every point along the rod the value of the background is also measured (see Section 2.5.6) using a paddle assembly.

After the data acquisition is complete, the background is subtracted, and the signal corrected for polarization effects [37, 38]. A Hanning filter [39] is applied first to eliminate the high frequency noise, especially from the low signal regions.

The reference is built next using an iterative algorithm. With the optimized parameters, the complex structure factors of all the rods with indices in the interval to be analyzed are explicitly calculated.

Only a finite range in Q_z is measured on every rod. Since the considered volume is centered at the origin of the reciprocal space, the region corresponding to a negative region of Q_z cannot be measured directly. Therefore, it has to be obtained from symmetry operations. Since, in general, the unit cell is distorted, no assumptions can be made involving centrosymmetric behavior.

We can, however, make use of the following symmetry relation which is true for all types of structures:

$$\mathcal{F}(Q_x, Q_y, Q_z) = [\mathcal{F}(-Q_x, -Q_y, -Q_z)]^* \tag{2.11}$$

, where * indicates the complex conjugate. The inplane symmetry is specific to every type of system investigated and will be addressed separately.

To artificially increase the data sampling density, zero padding is used. However, because the boundaries between the rod domain and the zero domains are sharp,

additional windowing needs to be applied in order minimize artifacts. The window of choice is gaussian and will be referred to as the artificial Debye-Waller factor. As a consequence, all ED peaks will be convoluted with a gaussian function which thus artificially increases their widths in a known way while eliminating the artifacts generated by the sharp boundary. This gaussian window is applied to both the newly generated rods and the measured data (Figure 2.3).

Figure 2.3: Zero padding and the additional gaussian windowing

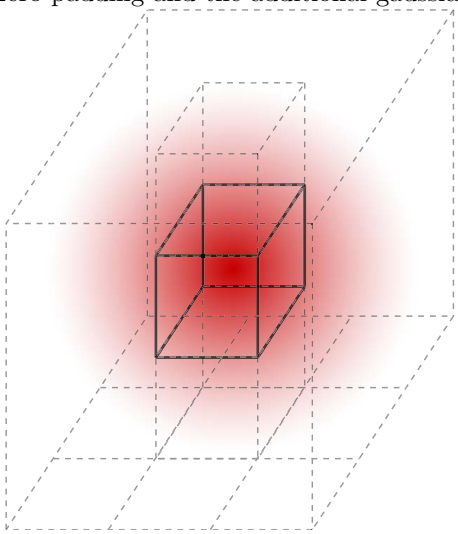

The following step is the 1D inverse Fourier transform of all the rods of reference along the vertical direction.

The phasing procedure is applied next; the result is filtered using a Hanning window on the Fourier transform. The regions corresponding to the Bragg peaks are removed from the calculated phasing term and replaced with interpolated values to avoid effects generated by the discontinuous behavior. Next, the inverse 1D Fourier transform is taken along the vertical direction and the result, after being copied in symmetry equivalent positions (see Figure 3.1 and Figure 4.2), is added to the inverse Fourier transform of the reference.

To increase the data sampling density in the horizontal direction, zero padding is

applied next, using, again, an additional artificial in-plane Debye-Waller factor. The final 3D ED is obtained at the end of the 2D inverse Fourier transform.

Depending on the quality of the fit, additional iterations are possible, feeding the value of the total complex structure factor as a reference.

2.3 Calculating the Reference

The reference is the best *ansatz* we can get for the structure to be investigated. In its calculation, all the information available about the sample has to be included. The true number of electrons must be used when generating the reference [40]. When the in–plane periodicity of the film is different than that of the substrate, the folded structure of the film has to be used. This is obtained by translating all the atoms of the film into vertical columns in the substrate unit cells with an integer number of substrate lateral unit cell vectors [37, 35]. The newly built unit cell is refered to as the *reduced unit cell*.

After the structural information is introduced, the CSF is calculated and the parameters optimized in a somewhat similar way to that described in [41]. Basically, the sum of squares of the differences between the data and the intensity corresponding to the generated CSF is minimized.

We assume as unknowns the following quantities: the multiplicative scale factor, the in–plane Debye-Waller factor of the bulk substrate, the out–of–plane Debye-Waller factor of the bulk substrate, the Debye–Waller factor of the explicit part of the substrate and the Debye-Waller factor of the film. The roughness of the vacuum interface has to be taken into account. To do that, the occupancy is considered 1 between the substrate and a certain position beyond which it is assumed gaussian. The position of the center of the gaussian and its width are subject to variation

during the fit. Additional distortions can be applied to the structure, subject to the fit optimization, especially as part of additional iterations.

2.4 Approximation Used for Phasing

If we consider two points along the same Bragg rod, corresponding to Q_z and $Q_z + \delta Q_z$, we can represent the summation of the amplitudes as in Fig.2.4(a)–Fig.2.4(b). If we write Eq.1.3 for each of these points we get:

$$A_T(Q_z) = A_{Ref}(Q_z) + A_U(Q_z) \tag{2.12}$$

$$A_T(Q_z + \delta Q_z) = A_{Ref}(Q_z + \delta Q_z) + A_U(Q_z + \delta Q_z) \tag{2.13}$$

Since the film is confined in the z direction it is natural to assume that, between

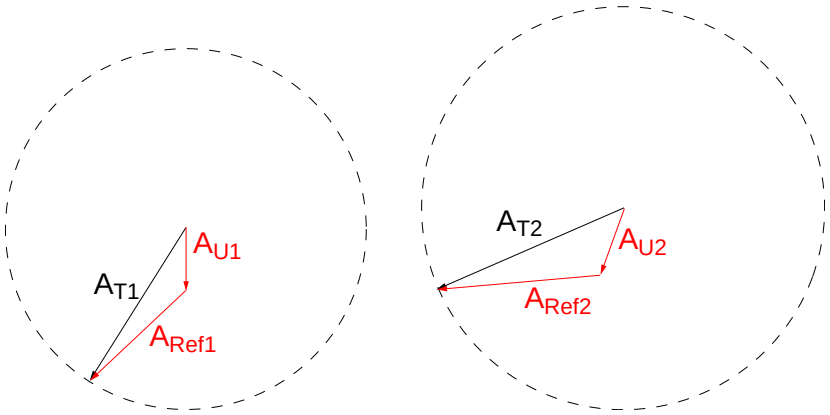

(a) The amplitude of scattered wave at Q_z

(b) The amplitude of scattered wave at $Q_z + \delta Q_z$

Figure 2.4: The Harker diagram for two sampling points along $\vec{Q}_z$

Bragg points, the amplitude is rather slowly varying. Also, since both the complex amplitude of the reference and the measured intensity are continuous between the substrate peaks, we can safely assume that the unknown component is continuous as well.

As the unknown component of the complex amplitude is small, for a reasonably small value of δQ_z–usually the distance between two consecutive sampling points along the rod–we can make the following approximation [33]:

$$A_U(Q_z + \delta Q_z) \approx A_U(Q_z) \tag{2.14}$$

If we represent both Harker plots in one figure using this approximation we get the diagram shown in Fig.2.5

Figure 2.5: The Harker diagram in the COBRA approximation

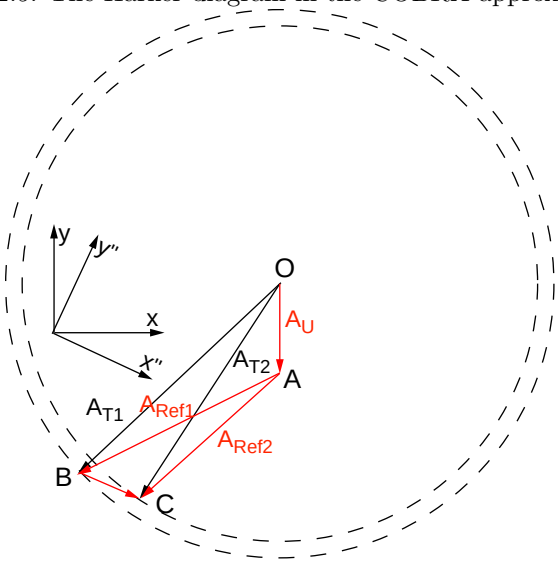

Since the intensities along the Bragg rods are measured, the absolute values of the total amplitudes are known:

$$I = \mid A_T \mid^2; \tag{2.15}$$

The complex amplitudes of the reference (A_{Ref}) are calculated through an iterative algorithm. Given these known quantities, it only takes some elementary geometry to calculate the complex value of A_U.

We start with a rotated reference system, $x'' - y''$, with the new x'' axis parallel

to BC. We can write:

$$OB^2 = OB_{x''}^2 + OB_{y''}^2 \tag{2.16}$$

with $OB_{x''}$ the real part and $OB_{y''}^2$ the imaginary part in a complex plane with the new coordinate system. In $\triangle OBC$ we can write:

$$OB \cdot \cos \angle OBC = \frac{BC^2 + OB^2 - OC^2}{2\,BC} \tag{2.17}$$

Thus, we get the value of $OB_{x"}$. From Eq.2.17 we get the other component:

$$OB_{y''} = \pm\sqrt{OB^2 - OB_{x''}^2} \tag{2.18}$$

There are two solutions and, at this point, we have to consider both of them. The newly determined complex value of the amplitude has to be transformed back to the initial coordinate system. A rotation needs to be performed and the multiplication factor is nothing but the phase factor of the x'' axis in the initial $x - y$ coordinate system:

$$A_{T1} = OB_{\text{x–y}} = OB_{\text{x"–y"}} \cdot \frac{BC}{\mid BC \mid} = OB_{\text{x"–y"}} \cdot \frac{A_{Ref2} - A_{Ref1}}{\mid A_{Ref2} - A_{Ref1} \mid} \tag{2.19}$$

Thus, the complex value of the amplitude of the scattered wave is determined.

2.4.1 Additional Phasing Iteration

Ideally, a real ED has non-negative values and is zero outside the sample. In general, this test will not be completely satisfied. A figure of merit of the quality of the fit is the magnitude of the negative ED. Successive iterations can be performed to minimize them. To do that, the reference needs to be modified. One type of iteration–referred to as a *small iteration*–defines the reference as the sum of the old reference and the phasing term. Another type of iteration–*large iteration*–can be performed doing another fit for the reference, this time with distortions like ED peaks shifts or splittings applied to the structure.

Figure 2.6: Experiment layout

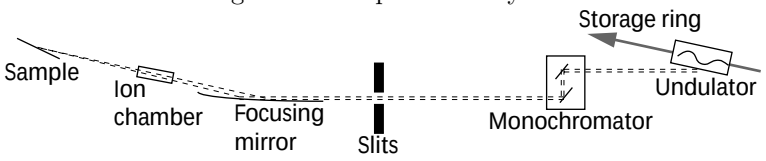

Repeating the phasing algorithm is a process that is not always convergent as additional noise is added with every step. As a general behavioral pattern, the fit converges with repeating the number of iterations until it starts to diverge due to the increase in noise.

2.5 Experimental Setup

2.5.1 General Layout

Since the Bragg rods usually involve a very high dynamic range measurement, all the experiments need to be performed using very bright x-ray sources. Additionally, the energy of the incident beam has to be adjusted according to the symmetry and chemical species present in the sample. These considerations make synchrotrons the only x-ray sources that meet the requirements for the Bragg rod data acquisition required for COBRA. Both studies that comprise the subject of this thesis were performed at ID beamline, Sector 7, Advanced Photon Source-Argonne National Lab.

The x-rays were generated when electrons pass through an undulator device (see Figure 2.6). The electrons travel between the poles of a series of magnets with alternating polarities. The gap separation can be adjusted to optimize the spectrum for a particular wavelength and the distance between two consecutive magnets is calculated in such a way that photons produced at two consecutive trajectory bends are in phase.

After x-rays are generated, they are monochromated using a Si (111) double crystal monochromator, situated 30m away from the insertion device. Because of the high incident intensity, the first crystal is continuously cooled with liquid nitrogen.

The x-ray beam path is kept in ultra high vacuum until the beam reaches the entrance of the hutches designed for user experiments. Inside the hutches, the beam is kept in flight paths filled with He, used because of the low scattering cross section given by its low Z.

The monochromated beam is then conditioned, both horizontally and vertically, using a set of slits. Next, a Rh mirror is used to focus the beam vertically. Downstream, the beam is first passed through an ion chamber used to monitor its intensity and next through an additional set of slits, mounted on the goniometer stage, used to keep track of the beam position.

The goniometer is positioned ∼55m away from the undulator. On its detector arm there is an assembly consisting of an XIA PF4 filter box, a paddle used to discriminate between the signal and background, the detector and the preamplifier.

All the equipment control and data acquisition instrumentation on the beamline can be handled through EPICS (*Experimental Physics and Industrial Control System*) [42] and SPEC [43, 44, 45]. For data acquisition, the Generalized Goniometer Control software (GGC), developed for Bragg rod analysis by Yacoby et al. [46] was used to control the EPICS server.

A few routines must be performed to ensure good data quality. Before the detector assembly is mounted, the goniometer alignment must be done using an autocollimator (see details in Section C and B). Next, the undulator must be tuned and the monochromator calibrated. The focusing mirror has to be tweaked. The center of the goniometer has to be found and marked on a video monitor and then moved

until the beam goes through the center of rotation. The orientation of the focused beam with respect to the reference system has to be measured. The position of the paddle used for background measurements must also be calibrated.

After mounting the sample, the first step is to align its normal along the $\vec{e}_\phi$ axis, and then roughly adjust its height. After that, one needs to obtain the orientation matrix. The signal to background ratio has to be measured and the filters calibrated. Before every scan, the detector offset must be measured.

2.5.2 Coordinate Reference System

It has to be mentioned that the acquisition software involves the use of a coordinate reference system that is not very intuitive and has to be described in detail.

The zero positions of the goniometer axis are defined as follows: at 0°, the 2θ arm is straight up. At 0°, the ψ and ν are approximately 45° to the beam direction, their precise orientation being dictated by the relatively arbitrary orientation of the goniometer. At this goniometer setting, the x axis of the lab frame coincides with the θ axis, with $\vec{e}_x = \vec{e}_\theta$ (see Figure 2.7); the y axis is in the plane of θ and ν axes and pointing downwards. The orientation of the z axis is given by $\vec{e}_z = \vec{e}_x \times \vec{e}_y$. The relative orientation of ϕ, ν, 2θ, ψ and χ (κ) are determined, one by one, using the autocollimator and a set of procedures which are specific for each of the geometries used (Kappa and Eulerian). The procedure assumes that all the axes point toward the center of the goniometer (within a reasonably small sphere of confusion) but assumes their orientation is unknown. For an ideal Eulerian geometry, when all the angles are set to zero, we have: $\vec{e}_\theta = \vec{e}_\phi = \vec{e}_{2\theta} = \vec{e}_x$, $\vec{e}_\psi = \vec{e}_\nu = \vec{e}_y$ and $\vec{e}_\chi = \vec{e}_z$. For an ideal Kappa, the axis orientation in the lab reference system will be: $\vec{e}_\theta = \vec{e}_\phi = \vec{e}_{2\theta} = \vec{e}_x$, $\vec{e}_\psi = \vec{e}_\nu = \vec{e}_y$ and $\vec{e}_\kappa = -\vec{e}_x \cos\kappa_0 + \vec{e}_z \sin\kappa_0$, where the κ_0 angle is specific to Kappa geometry and has a value of $\sim 50°$.

All the vectors explicitly describing beam orientation, sample normal, a fixed axis in the lab will be with respect to the reference described above. In the data analysis, and all the references made to the rod indices, reciprocal space etc., we will consider the commonly used reference system which assigns $\vec{e}_z$ along the surface normal.

2.5.3 Energy Setting

In combination with the undulator, the monochromator allows an energy setting between 5 keV and 50 keV. The accessible region in the reciprocal space is given by the radius of the Ewald sphere:

$$R_{Ewald} = \frac{2\pi}{\lambda} = \frac{E}{\hbar c} \tag{2.20}$$

As one can easily see, the larger the energy, the larger the radius. So, as the energy increases, the high limit of Q_z will increase on all rods. This defines one requirement, to choose an energy as high as possible.

Another factor that has to be considered is the chemical composition of the sample. In an x-ray diffraction experiment fluorescence is usually a nuisance which can be dealt with using energy discrimination. It becomes important whenever the energy of the incident beam is higher and of approximately the same value as the binding energy of an electronic shell. In the case of Bragg rod experiments, given the requirement for the high dynamic range and the fact that - because the detector is operated in DC mode–energy discrimination cannot be used, fluorescence is to be

Figure 2.7: The relative orientation of the incident beam and the reference system

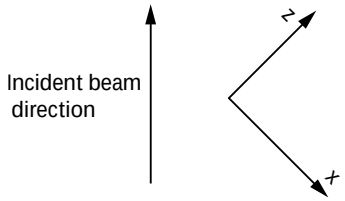

avoided at any cost.

So, as a rule, one can choose an energy setting as high as possible but below the lowest atomic binding energy of the elements present in the sample.

2.5.4 Goniometer Alignment

The first step is to rigourously determine the relative orientation of the goniometer axes. To achieve that, an autocollimator has to be used and, according to the type of goniometer geometry used (Eulerian or Kappa), a specific alignment procedure has to be followed (see Appendices B, C).

The GGC software offers the capability to control a goniometer in Kappa geometry as if it were an Eulerian one. This is done by the means of pseudomotors, routines that are able to calculate the position of Kappa motors as a function of the target angular value in Eulerian geometry. Therefore, throughout all the alignment routines the angular position considered Eulerian geometry and their implementation in Kappa was done using this feature.

To find the center of the goniometer we used a tungsten wire $100\mu m$ thick, set on a holder that fits on the goniometer head. The first step was to get it to overlap with the ϕ axis. A camera was focused on the wire and its position marked on the monitor for certain values of ϕ. The goniometer head allowed for translation on 2 perpendicular directions and angular adjustments about 2 axes parallel with them. The ϕ axis was rotated to have one translation axis perpendicular to the direction of the camera. The position and tilt were adjusted and then ϕ was rotated by 180°. The adjustment and the 180° rotation were repeated until no position/tilt changes were observed on the screen. Next, ϕ was rotated by 90° - to get the other translation axis of the goniometer head perpendicular to the optical axis of the camera. The ϕ rotation sequence was repeated until the wire image did not change its position and

or its tilt.

After the procedures described above were executed, the tungsten wire was along the ϕ axis. Its image on the monitor was marked for 2 values of χ, $-90°$ and $0°$. The intersection of the lines marks the center of the goniometer.

The next thing to be done after focusing the beam and identifying the center of the goniometer is to position it in the focused x-ray beam. χ was set first to $0°$. Downstream of the goniometer, an ion chamber was set, referred to as the *wall* ion chamber. The beam was turned on and the goniometer was scanned vertically. Since the tungsten wire was covered in fluorescent $ZnSO_4$, it was easy to spot when it passed through the beam. The goniometer height was scanned around that position and the intensity on the wall ion chamber was recorded. When the wire passed through the beam the intensity dimmed. The goniometer was moved to the corresponding position, bringing it thus to the same height as the beam.

χ was moved to $-90°$ to set the wire vertical. The goniometer was next translated horizontally until the beam illuminated on the fluorescent coating of the vertical reference wire. At this point, the goniometer horizontal position was scanned and finally set at the center of the dip registered in the *wall* ion chamber. At this moment, the beam passed through the center of the goniometer.

2.5.5 Determination of the Incident Beam Orientation

The focusing mirror changes the direction of the beam. Its orientation relative to the goniometer has to be accurately known in order to be able to have an accurat positioning in reciprocal space. To do that, the goniometer is set to $\chi = 0°$, $\theta = 0°$, $\psi = -45°$. A rod is mounted horizontally on the goniometer along the beam orientation and, perpendicular to it, is attached a piece of burn paper with a camera focused on it. A burn is taken and the position of the spot is marked on the monitor.

The acquisition software allows the rotation of the detector about any arbitrary axis passing through the center of the goniometer. Since the beam already satisfies this condition, this constraint can be used to determine the precise beam orientation. Given the geometry of the system, the beam direction will be close to the $[-\frac{\sqrt{2}}{2}, 0, \frac{\sqrt{2}}{2}]$ axis. A rotation of 180° is done about this axis and the orientation of the axis is tuned until the x-ray burn overlaps again with the marked spot on the monitor.

The orientation of the axis so determined represents the direction of the incident beam.

2.5.6 Detector Arm Alignment

The detector arm supports the attenuator box, the detector itself and an assembly used to discriminate between the background and signal. The attenuators are pneumatically activated and will be described in detail for each experiment.

We used a detector consisting of a plastic scintillator in front of a Hamamatsu RG47-04 photomultiplier tube, connected to a low-noise preamplifier. The signal was input in a voltage-to frequency converter and, from its TTL output, sent to a scaler.

The high intensity of the incident beam required a large dynamic range on the detection side as well. To achieve this, the detector was operated in DC mode. The preamplifier gain was set in such a way that the system required 9-10 filters for a reading on a Bragg peak. Under these conditions, the dark signal was of the order of $\sim 10^2$ counts$\cdot$s^{-1}.

The dynamic range of the electronics was limited by the length of the pulse at the output of the frequency converter. The behavior of the assembly was considered to be linear up to a counting rate of $\sim 10^5$ counts$\cdot$s^{-1}. Beyond that value, the finite pulse width at the output of the voltage–to–frequency converter ($\sim 1\,\mu$s) became a

limiting factor, making some of the pulses impossible to discriminate.

The paddle assembly consists of a paddle with a series of openings, formed by Pb masking tape. It rests on the axis of a stepper motor and, depending on its position, will allow either the signal or the background to be measured by the detector.

The detector and the paddle rest on an x–y translation stage used to align the paddle openings. The alignment procedure is done without the detector mounted, after the goniometer was aligned and the direction of the incident beam vector was determined. The rough alignment is done with the *signal* opening of the paddle centered. The 2θ arm has to be aligned along the direction of the incident beam vector. The x and y of the detector translation stage are scanned individually and, at the end of each scan, the position of the center of the peak is chosen as a coordinate for the corresponding axis.

Figure 2.8: The paddle

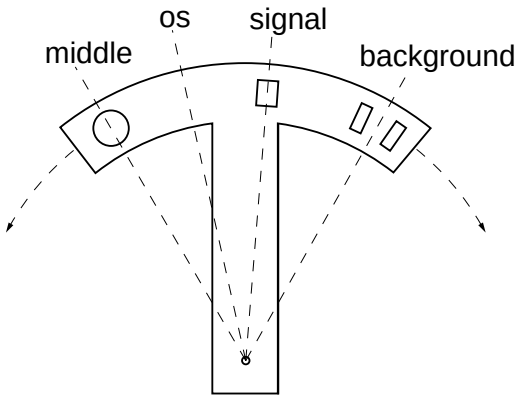

The paddle was designed to operate in one the four possible settings, referred to as: *signal*, *background*, *os* and *middle*.

signal opening is used for the measurement of the signal itself. It consists of a single opening, $\sim 3 \times 4$ mm.

background is an assembly of two openings, $\sim 2 \times 4$ mm each. When this position

is selected, the center of the region between the two signal openings should be on the optical axis of the detector arm. The diffracted signal is blocked by the Pb masking tape and only the signal on the side is allowed to reach the detector.

os is a setting used to determine the offset of the detector. When this position is chosen, no x-ray photon is allowed to reach the detector.

middle is used when the detector needs to be wide open, with no collimation from the paddle whatsoever.

2.5.7 Sample Alignment

The sample was attached with wax on an aluminium sample holder which was set on a goniometer head mounted on the ϕ axis. The ψ angle was set $-45°$. To adjust the tilt, a laser level was used. The χ value was set to $0°$ and the laser was incident on the sample in such a way that the positions of the reflected beam were observed on a wall approximately 10 feet away. The position of the spot was marked, ϕ was rotated through $180°$ and then the position marked again. To get the sample perpendicular on the ϕ axis, the tilt was adjusted using the arcs of the goniometer head until the reflection hit the center of the segment determined by the two marked positions.

To get the correct height we brought χ down to $90°$ and adjusted θ until the sample surface was parallel to the optical axis of the camera. The sample height was adjusted until the sample surface plane contained the center of the goniometer.

In order to be able to reach any point in the reciprocal space the orientation matrix of the sample with respect to the goniometer was needed. To ease this task, a known crystallographic direction of the substrate has to be roughly aligned with the direction of the incident beam. In the case of semiconductor samples, a common

property of the zincblende III-V crystals was considered: they cleave along {110} and {−110} crystallographic planes. The perovskites cleave along {010} and {100}. Given this information, a rough alignment would involve setting the sample along the right orientation at the zero position.

To find the orientation matrix it was sufficient to find two reflections with non-collinear diffraction vectors [47, 48, 49, 50]. For the ⟨001⟩ sample orientation, the first reflection is usually of $(00L)$ type, with L an integer. To find it, 2θ and θ are set to the calculated values for the reflection. With the x-ray beam on, the intensity of the diffracted beam is optimized tweaking the rest of the angles until the peak is reached. The next reflection is usually found after a rotation in ϕ. Optimizing these reflections will allow the calculation of the first orientation matrix. This is used next to roughly find other reflections. Optimized, they allow a more precise determination of the relative orientation of the sample with respect to the goniometer.

CHAPTER III

The Morphology of the GaSb-InAs Interface

3.1 Motivation of the Study

It is natural that electrons transported through a semiconductor heterostructure will cross at least one separation region between two materials, usually with different bandgaps. Moreover, it is common that the structure of an electronic device consists of a superlattice which will involve a significant number of interfaces. As the thickness of the epitaxial films involved decreases - in the case of short period superlattices (SPS) - the relative importance of the interface layers increases. These facts lead to the conclusion that a good understanding of the morphology of the transition region between two semiconductor films is essential for the level of reproducibility required to fabricate high performance $III - V$ devices.

Advances in deposition techniques over the past 20 years allow a thickness control with sub-monolayer precision. The Holy Grail of material growth - the creation of perfectly flat interfaces - is, unfortunately, still at large. Usually, a transition layer exists between two materials appearing as a disordered region. Two types of phenomena can generate it: morphological roughness - which originates in the surface kinetics during growth - and intermixing. The second phenomenon is material specific and its occurence can be anticipated, to some extent, by studying the phase diagrams

(although *bulk* phase diagram are, at best, only a guide).

From the electronic point of view, interfacial disorder can interfere with electron transport by introducing additional scattering centers [51] and band distortions in the separation regions [52].

InAs and GaSb have many features that make them attractive: their lattice constants–a_{InAs} = 6.0584 Å, a_{GaSb} = 6.0959 Å–are very similar; both have direct bandgaps that are quite low: E_{InAs} = 0.36 eV and E_{GaSb} = 0.72 eV at T = 300 K[53]. These features make them ideal candidates for infrared optoelectronics [54]. The low lattice mismatch creates the premises of heterostructures with a high critical thickness, allowing for a high number of SPS and thus for devices with a high quantum efficiency.

However, the epitaxial growth of compound $III-V$ semiconductors containing both arsenic and antimony is difficult because of the miscibility gap in the quaternary alloy InGaAsSb [55]. The phenomenon has an impact on the electronic properties; for example, a blueshift of the bandgap is expected [56].

The behavior of the interface has been investigated using other techniques. Cross section STM studies have been reported [57, 58, 59] with interesting results. However, the technique has a few significant limitations. The scan can only be done along the directions corresponding to the cleavage planes and, due to the structure of zincblende, not all atomic planes can be imaged. There are also difficulties relating to the interpretation of STM images.

This study uses Coherent Bragg Rod Analysis (COBRA) to characterize the InAs–GaSb interface, with each material as a substrate and the other as the deposited film. In both cases, the substrate surface was (001).

3.2 The Bragg Rods of the Zincblende System

The atomic positions in the unit cell for the III–V systems to be investigated are as follows (fractions of the unit cell): group III atoms are at $(0,0,0)$, $(\frac{1}{2},\frac{1}{2},0)$, $(0,\frac{1}{2},\frac{1}{2})$, $(\frac{1}{2},0,\frac{1}{2})$ and group V are at $(\frac{1}{4},\frac{1}{4},\frac{1}{4})$, $(\frac{3}{4},\frac{3}{4},\frac{1}{4})$, $(\frac{1}{4},\frac{3}{4},\frac{3}{4})$ and $(\frac{3}{4},\frac{1}{4},\frac{3}{4})$. Due to layer incompletion in the upper layers of the film and the zincblende structure, the intensity of the scattered wave does not preserve the four–fold symmetry of the bulk.

Thus, the expression of the structure factor given by the Eq.2.9 takes on the particular form:

$$\begin{aligned}\mathcal{F}(Q_x,Q_y,Q_z) = \int_V d^3r \sum_{j_x,j_y=-\infty}^{+\infty}\sum_{j_z=1}^{N_{uc}}[f_{1j_z}(\vec{r}\cdot\vec{e}_z)+ \\ + f_{2j_z}(\vec{r}\cdot\vec{e}_z)\cdot e^{2\pi i(\frac{1}{2}Q_x+\frac{1}{2}Q_y)} + f_{3j_z}(\vec{r}\cdot\vec{e}_z)\cdot e^{2\pi i(\frac{1}{2}Q_y+\frac{1}{2}Q_z)}+ \\ + f_{4j_z}(\vec{r}\cdot\vec{e}_z)\cdot e^{2\pi i(\frac{1}{2}Q_x+\frac{1}{2}Q_z)} + f_{5j_z}(\vec{r}\cdot\vec{e}_z)\cdot e^{2\pi i(\frac{1}{4}Q_x+\frac{1}{4}Q_y+\frac{1}{4}Q_z)}+ \\ + f_{6j_z}(\vec{r}\cdot\vec{e}_z)\cdot e^{2\pi i(\frac{3}{4}Q_x+\frac{3}{4}Q_y+\frac{1}{4}Q_z)} + f_{7j_z}(\vec{r}\cdot\vec{e}_z)\cdot e^{2\pi i(\frac{1}{4}Q_x+\frac{3}{4}Q_y+\frac{3}{4}Q_z)}+ \\ + f_{8j_z}(\vec{r}\cdot\vec{e}_z)\cdot e^{2\pi i(\frac{3}{4}Q_x+\frac{3}{4}Q_y+\frac{3}{4}Q_z)}]\cdot e^{\frac{-(2\pi DW_{factor}|\vec{Q}|)^2}{2}} \qquad (3.1)\end{aligned}$$

The Bragg peaks follow, of course, the rules for *fcc* structure: the three indices are integers and are either all odd or all even. We will refer to a rod as hkL, with the new indices given by:

$$Q_x = h;\ Q_y = k;\ Q_z = L, \qquad \text{where} \quad h,\ k \in \mathbf{Z}, \quad L \in \mathbf{R} \qquad (3.2)$$

A perusal of Eq.3.1 reveals a few interesting points. First, the intensity along the Bragg rods with mixed indices (even–odd or odd–even) is very low; they will not be measured as the features will be below the noise level.

Also, the measured intensity of the diffracted wave is:

$$I(\vec{Q}) = \mid \mathcal{F}(\vec{Q}) \mid^2 \qquad (3.3)$$

Figure 3.1: Symmetry equivalence for the Bragg rods of zincblende structure

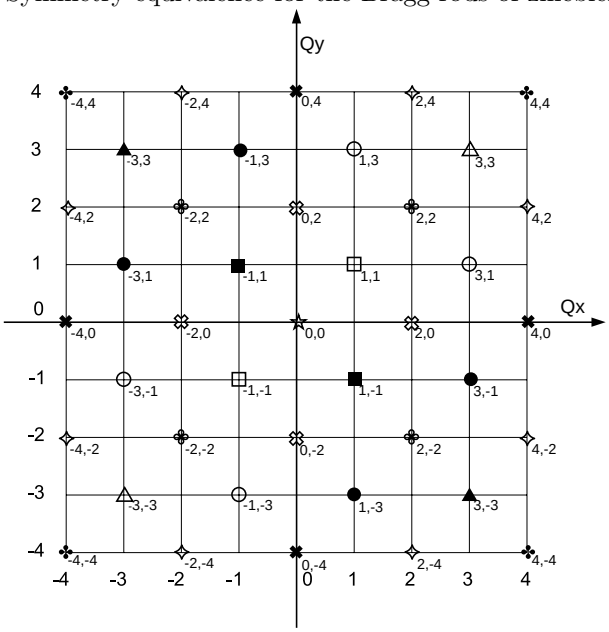

The symmetry equivalence for the rods with indices in the interval $[-4, 4]$ is shown in Fig.3.1.

For even indices (h,k), the symmetry equivalence works as follows:

$$hkL \equiv khL \equiv \overline{h}kL \equiv h\overline{k}L \equiv \overline{h}\,\overline{k}L \equiv \overline{k}hL \equiv \overline{h}L \equiv \overline{k}\,\overline{h}L \tag{3.4}$$

For odd indices, the symmetry relations are:

$$hkL \equiv khL \equiv \overline{h}\,\overline{k}L \equiv \overline{k}\,\overline{h}L \tag{3.5}$$

and

$$h\overline{k}L \equiv \overline{k}hL \equiv \overline{h}kL \equiv k\overline{h}L \tag{3.6}$$

but

$$hkL \not\equiv \overline{h}kL \tag{3.7}$$

To be able to completely cover all the 81 rods with (h,k) indices in the interval $[-4, 4]$, given the symmetry operations in Eq.3.5–3.7, 12 rods are needed. Those rods are: $00L$, $11L$, $20L$, $22L$, $31L$, $33L$, $40L$, $42L$, $44L$, $\overline{1}1L$, $\overline{3}1L$ and $\overline{3}3L$.

Figure 3.2: Transmission through 10 μm Cu [1]

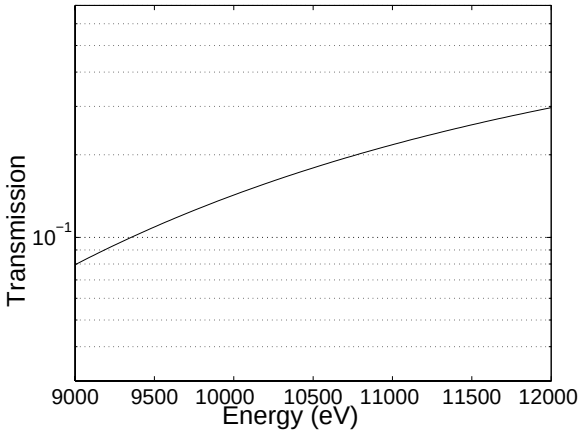

As a general remark, it must be mentioned that the rods in opposite quadrants (I–III and II–IV) are equivalent and in the adjacent ones are not. This asymmetry will vanish as the occupancy of the top layers will get close to 100% and the thickness of the film will tend to an integer multiple of unit cells.

3.3 The Experimental Setup

For this experiment, a six circle Huber goniometer was used. The value of ψ was set to $-45°$, bringing the χ circle plane approximately perpendicular to the incident beam. Once this value set, it and was not changed throughout the duration of the experiment. The distance between the detector and the center of the goniometer was 0.96 m.

3.3.1 Filters

The main consideration in choosing the filters in front of the detector was the absorption of the filter material at the energy we ran the experiment. As a general requirement, the transmission had to be around 15–20%. Figure 3.2 shows a plot of transmission of a 10 μm Cu foil in an energy interval that contains the value selected for our experiment. The XIA PF4 filter box handled 4 independent attenuators

which were all made of Cu with different thicknesses: 10, 20, 40 and 80 μm. This gave 16 independent settings which we will refer to as filters. The initial values of the transmission were estimated based on the properties of the Cu at 10.25 keV; after the whole setup was completed, the transmission values were measured as follows: we found a Bragg peak and then we moved the 2Θ arm away from the diffraction condition until the measured intensity required no filter in front of the detector. We measured the fluence and then repeated the measurement, this time with the first filter in. From the ratio of the fluences we calculated the transmission of the first filter. We moved the goniometer arm until 2 filters were required in front of the detector and measured the fluence again, this time with 1 and 2 filters in. Since we already had the transmission of the first filter we were able to calculate the transmission of the second filter as well. We repeated the whole procedure until we had 11 filters measured; the transmission of the remaining filters was calculated based on the previously measured values. The final filter settings are listed in Table 3.1.

Table 3.1: The attenuation values for the Cu filters at 10.25 keV

Filter #	Attenuators in	Thickness (μm)	Transmission at $10.25keV$	Transmission at $30.75keV$
0	none	0	1	1
1	I	10	$1.7990 \cdot 10^{-1}$	$9.1000 \cdot 10^{-1}$
2	II	20	$3.2376 \cdot 10^{-2}$	$8.2810 \cdot 10^{-1}$
3	$I + II$	30	$5.8769 \cdot 10^{-3}$	$7.5357 \cdot 10^{-1}$
4	III	40	$1.0728 \cdot 10^{-3}$	$6.8575 \cdot 10^{-1}$
5	$I + III$	50	$1.9440 \cdot 10^{-4}$	$6.2403 \cdot 10^{-1}$
6	$II + III$	60	$3.5192 \cdot 10^{-5}$	$5.6787 \cdot 10^{-1}$
7	$I + II + III$	70	$6.3705 \cdot 10^{-6}$	$5.1676 \cdot 10^{-1}$
8	IV	80	$1.1532 \cdot 10^{-6}$	$4.7025 \cdot 10^{-1}$
9	$I + IV$	90	$2.0876 \cdot 10^{-7}$	$4.2793 \cdot 10^{-1}$
10	$II + IV$	100	$3.7790 \cdot 10^{-8}$	$3.8942 \cdot 10^{-1}$
11	$I + II + IV$	110	$6.8408 \cdot 10^{-9}$	$3.5437 \cdot 10^{-1}$
12	$III + IV$	120	$1.2384 \cdot 10^{-9}$	$3.2248 \cdot 10^{-1}$
13	$I + III + IV$	130	$2.2417 \cdot 10^{-10}$	$2.9345 \cdot 10^{-1}$
14	$II + III + IV$	140	$4.0580 \cdot 10^{-11}$	$2.6704 \cdot 10^{-1}$
15	$I + II + III + IV$	150	$7.3459 \cdot 10^{-12}$	$2.4301 \cdot 10^{-1}$

One issue we needed to address is the amount of the third harmonic in the incident beam and its behavior after filtration. As mentioned before, the monochromator used is Si (111). After the undulator, the intensity corresponding to 3×10.25 keV is relatively small but not negligible. Because both (111) and (333) are allowed reflections, the diffraction conditions for the (111) reflection of the first harmonic and (333) of third harmonics will be satisfied simultaneously and all the photons corresponding to the latter will go through. This is why the incident beam will contain a high energy component that can not be completely neglected. The behavior of the Cu filters at different wavelengths varies. Table 3.1 shows also a comparison between the transmission of the filters at the two energies. This means that the ratio between the fluence of the third harmonic and the first harmonic will increase with increasing number of filters.

In a normal setup, where energy discrimination is used, this issue is properly solved since the pulses generated by the higher harmonic photons don't get counted. Because the requirements for a high dynamic range forced us to operate the detector in DC mode, energy discrimination was, as mentioned before, not available.

Fortunately, the only regions where a significant number of filters is required are in the vicinities of the Bragg peaks, which are excluded anyway from the analysis (see Section 2.2.1). The features on the Bragg rods don't usually require more than 2 filters and thus the spectral composition of the beam is not dramatically affected.

3.3.2 Energy Setting

The film and the substrate have a very small lattice constant mismatch ($\sim 0.6\%$), and thus we expect the strongest features of the Bragg rods in the regions around the Bragg points. Since the structure of the sample is zincblende, the Bragg peaks are far apart, at a distance of 2 reciprocal space units. To maximize the amount of

useful data it is vital to be able to scan between as many peaks as possible - meaning a requirement for a large radius of the Ewald sphere and thus a large energy.

As we can see in Table 3.2, the energy of the *K1s* shell of Ga is 10.367 keV. Any energy setting above it would result in a significantly increased fluorescence background which cannot be properly eliminated. This is why this value represents the upper threshold of the energy setting.

The energy of choice was 10.25 keV. To achieve that, the initial setting of the undulator gap corresponded to the energy of 10.305 keV as the undulator energy setting is usually ~ 50 eV higher than the desired monochromator value. To calibrate the energy of the monochromator, we scanned the energy and plotted the transmission through a thin foil of Ge. Features in the fine structure allowed us to calibrate the energy setting of the mono with a precision on the order ~ 1 eV.

Table 3.2: Binding energy [2] for the atomic species present in the sample (eV)

Element	Z	$K1s$	$L_1 2s$	$L_2 2p_{1/2}$	$L_3 2p_{3/2}$
Ga	31	10,367			
As	33	11,867			
In	49	27,940	4,238	3,938	3,730
Sb	51	30,491	4,698	4,380	4,132

3.3.3 Preparation of the Incident Beam

At the exit of the monochromator the beam has an elliptical cross section with a large axis on the order of ~ 0.5 mm. Since the angle of incidence will be relatively small ($\leq 5°$) and the sample normal will make a similar angle with the vertical, the beam footprint on the sample will be increased by a factor of $\frac{1}{\sin\alpha}$, where α is the angle made by the incident beam with the surface. It is, therefore, necessary to focus the beam at least in the vertical direction. To do that, a Kirkpatrick-Baez (KB) mirror was used. It consisted of a silicon plate covered with Rh. Two stepper motors

Figure 3.3: Calculated mirror reflectivity at $E = 10.25$ keV

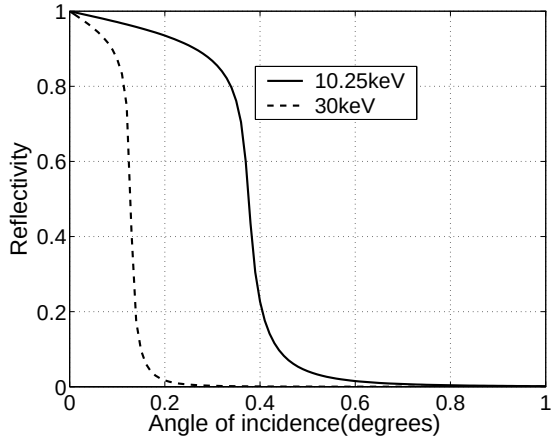

can control the bend, and thus the focal distance. In order to achieve reflection, the incidence angle on the mirror has to be below the critical angle. Since the critical angle decreases with increasing the energy, it is possible to set the incidence angle below the critical angle corresponding to $E = 10.25$ keV but above the one corresponding to $E = 30.75$ keV-the third harmonic(Fig.3.3). Thus, the $E = 10.25$ keV component will be totally reflected while the higher energy will penetrate the mirror, reducing the amount of third harmonic in the beam.

The vertical size of the beam was reduced down to $\sim$ 50 μm. For the other direction, the horizontal slit before the KB mirror was set to 400 μm, thus setting the horizontal size of the beam. Given the value of the incidence angle, the footprint of the x-ray is of the order of 500 μm$\times$400 μm.

To determine the sample height, after the normal was aligned with the θ axis, the goniometer was set to $\chi = 0^\circ$. The height was roughly adjusted to coincide the sample surface with the center of the goniometer. Next, fluorescent powder has been carefully sprinkled on the side of the sample and a high magnification camera focused on it. With the sample normal oriented roughly along the fixed axis used in the measurements, the height was scanned. The lowest and highest positions where

the beam hit the edges were recorded and the spots identified on the sample. Since the position of center of the sample was known, the height was determined based on the ratio of the distances to the points where the beam hit the edges.

3.4 Issues in the Analysis of Zincblende–Type Structures

The key to a good fit in the phasing stage is to have a reference as close as possible to the real structure. To do that, one must use all the information available about the sample such as exact layer sequence, surface roughness and Debye–Waller factors etc.

The zincblende symmetry of the sample requires some special considerations. As discussed in Section 3.2, the Bragg rods do not have a four–fold symmetry but only two–fold in the reciprocal plane corresponding to the sample surface. The bulk peaks, which are used for the sample alignment, have four–fold symmetry. Therefore, we are left with an ambiguity. After the orientation matrix was determined, there are two possible, non-equivalent ways of considering the quadrants and thus indexing the rods.

A realistic model of the probed surface would consider both types of symmetry, with different coverage area. This would lead to a termination type that would be dominant. To identify it, we try to fit the rods with the reference considering the rods in two adjacent quadrants. The best fit will determine the dominant symmetry and thus the dominant quadrant. The presence of the other surface symmetry will be disregarded from the calculation of the reference and the phasing procedure will correct for this approximation.

As far as multiple phasing iterations are concerned, the symmetry of the system is a severely limiting factor. Usually, as the phasing procedure is applied successively,

considering the results of the previous analysis as reference, a certain amount of noise is added due to the windowing process. When setting the highest limit of L (see Section 2.2.1) one thing to consider is the amplitude of the scattered wave at that particular value. In order to avoid artifacts due to abrupt termination followed by zero padding, apart from the artificial Debye–Waller factor added, one must make sure that the upper limit is set in such a way that the scattered amplitude is as low as possible at that particular point. In the case of perovskites, since for all the rods the anti-Bragg points are located at the same values of L, the choice is obvious. In the case of zincblende, anti-Bragg L values on the odd rods coincide with the values for Bragg points on even rods and therefore condition of minimum on the higher threshold is impossible to satisfy simultaneously on all rods. Attempts to define the upper limit at one of these points resulted in a very noisy final electron density. The value of choice was 5.5 RLU. It is neither the maximum nor the minimum on any of the rods but the amplitudes behave continuously near this value on all the rods. However, the finite non-zero value introduces a significant amount of noise with every repeated phasing iteration.

3.5 InAs Film Grown on GaSb Using As_4, Sample $r811$

3.5.1 The Sample

The sample was MBE grown in Prof. Mirecki–Millunchick's lab on a GaSb substrate with $\langle 001 \rangle$ orientation. In and Ga were evaporated from regular k-cells while In and Sb were evaporated from valved cracker effusion cells.

The Ga cell temperature was set to $t_{Ga} = 995°\text{C}$ corresponding to a Beam Flux Monitor (BFM) reading of 7.3×10^{-7} torr. The indium cell temperature was $t_{In} = 860°\text{C}$, giving a BFM readout out of 3×10^{-7} torr. The bulk temperature of the Sb cell was set at $t_{Sb}^{bulk} = 560°\text{C}$ and the cracker temperature at $t_{Sb}^{cracker} = 900°\text{C}$ giving

a BFM reading of 9.4×10^{-7} torr.

For As, the bulk temperature was set at $t_{As}^{bulk} = 401°C$ and the cracker temperature at $t_{As}^{cracker} = 600°C$, corresponding to a BFM reading of 3.5×10^{-6} torr. The As cracker temperature ensured a high concentration of As in the tetramer state (As_4).

A buffer layer of 0.3 μm of GaSb was grown on the substrate to ensure a controlled stoichiometry and a good surface quality. The buffer layer was terminated with one atomic layer of Sb (group V). 9 monolayers were deposited starting with In (group III), one monolayer of InAs consisting in one layer of In and one layer of As, corresponding to half of a unit cell. The sample was terminated with As (group V). During the growth the substrate temperature was set to 450°C.

3.5.2 Experiment

To find the matrix that describes the orientation of the sample with respect to the goniometer first the (400) and (202) reflections were found. Using them, a preliminary orientation matrix was calculated. With it, the following reflections were optimized: (206), (222), (244), (131), (311), (115) and (200). A precise determination of the orientation matrix was thus made possible.

Table 3.3 lists the rods acquired for this sample and the L limits. A data sampling density of 100 points/reciprocal space unit was used.

3.5.3 Data Analysis

In the calculation of the reference one must consider the sample structure described in Section 3.5.1. Since the zincblende structure of the sample does not allow a four fold symmetry, there is a quadrant indetermination that has to be resolved (see Section 3.4). To do that we assume successively that rods are in quadrants I and II. A fit with 1200 iterations is performed for every quadrant and the results

are compared with the data. As a figure of merit of the quality of the fit the sum of squares of the differences is used.

The start values of the fit parameters and the results after the fitting procedure are listed in Table 3.4.

After the fit, the sum of squares for the rods assumed in the first quadrant was 2.451. For the second quadrant, the sum value was 0.448. The reference considering rods in the second quadrant therefore gives a better fit than considering them in the other one. The analysis of this sample will, therefore, consider the rods as being in the second quadrant. The rods measured had the indices $00L$, $\overline{1}1L$, $\overline{2}0L$, $\overline{2}2L$, $\overline{3}1L$, $\overline{3}3L$, $\overline{4}0L$, $\overline{4}2L$ and $\overline{4}4L$.

After determining the reference, the phasing procedure was applied and a first result was found. The attempt to pass the new complex structure factor as reference resulted in an increased noise in the final fit. The results obtained after the first iteration were, therefore, the final one.

For the artificial Debye–Waller factor, for both inplane and vertical directions a value of 0.1 reciprocal unit cell^{-1}(rec.UC^{-1}) was used.

Figures 3.22–3.29 present the data, the reference and the final result after the phasing procedure. The result is in the form of a 3D electron density. A few plots,

Table 3.3: Rods measured for sample $r811$ and the corresponding L intervals(in reciprocal space units)

Rod index	L_{start}	L_{end}
$00L$	0.1	4.80
$11L$	0.5	3.80
$20L$	0.5	4.30
$22L$	0.5	4.80
$31L$	0.5	4.98
$33L$	0.5	5.25
$40L$	0.5	4.90
$42L$	0.5	5.00
$44L$	0.5	3.32

Table 3.4: Parameters used to generate the reference for sample $s811$, before and after the fit

	UC dist.	Mult. factor factor	in plane DW bulk subs.	vertical DW bulk subs.	DW film	DW explicit subs.	interf. gauss. position	interf. gauss. width
units		RLU^{-1}	RLU^{-1}	RLU^{-1}	RLU^{-1}	UC	UCs	
initial	1.000	3.00×10^{-4}	0.0500	0.0500	0.0500	0.0500	2.00	2.00
fit	0.998	3.73×10^{-4}	0.0322	0.0329	0.0332	0.0368	1.75	1.63

Figure 3.4: The total electron density profile along z in InAs film on GaSb, sample $r811$

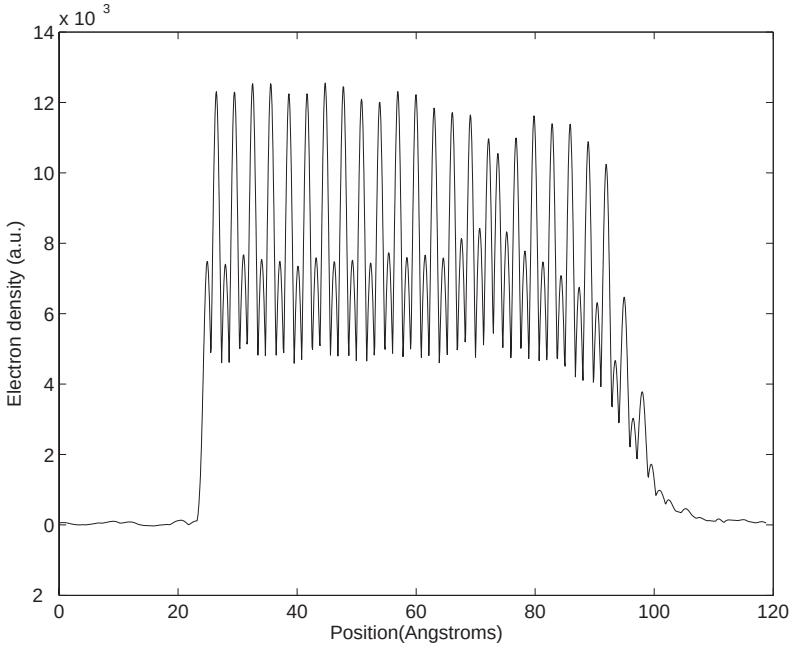

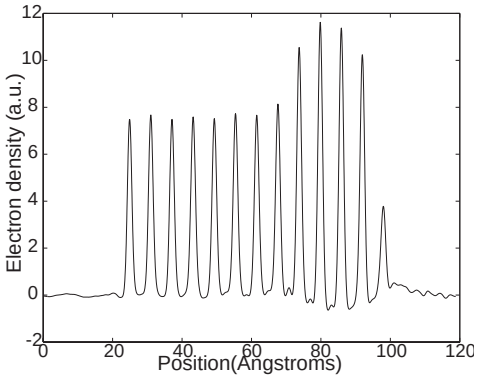

(a) Electron density profile through group III-plane 1

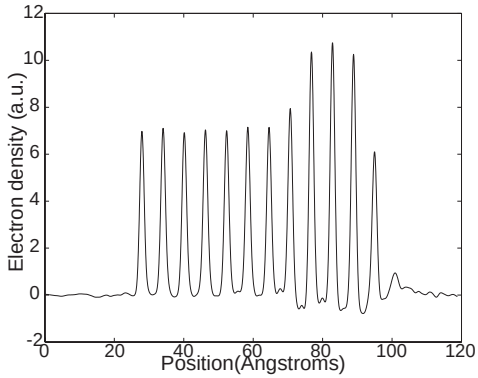

(b) Electron density profile through group III-plane 2

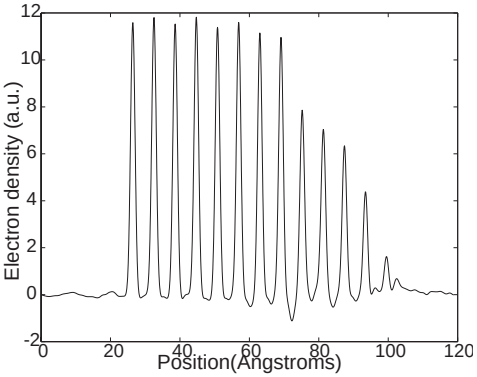

(c) Electron density profile through group V-plane 1

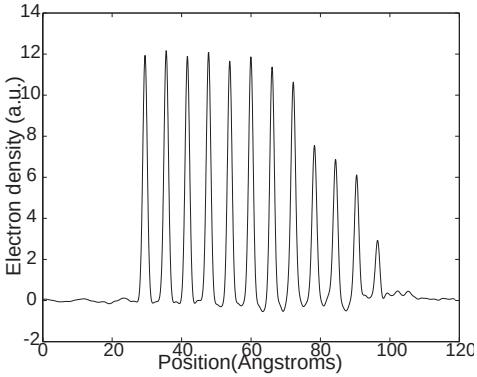

(d) Electron density profile through group V-plane 1

Figure 3.5: Electron density profiles for GaSb film on InAs, sample $r811$

Figure 3.6: Integrated electron density values for InAs film on GaSb, sample $r811$

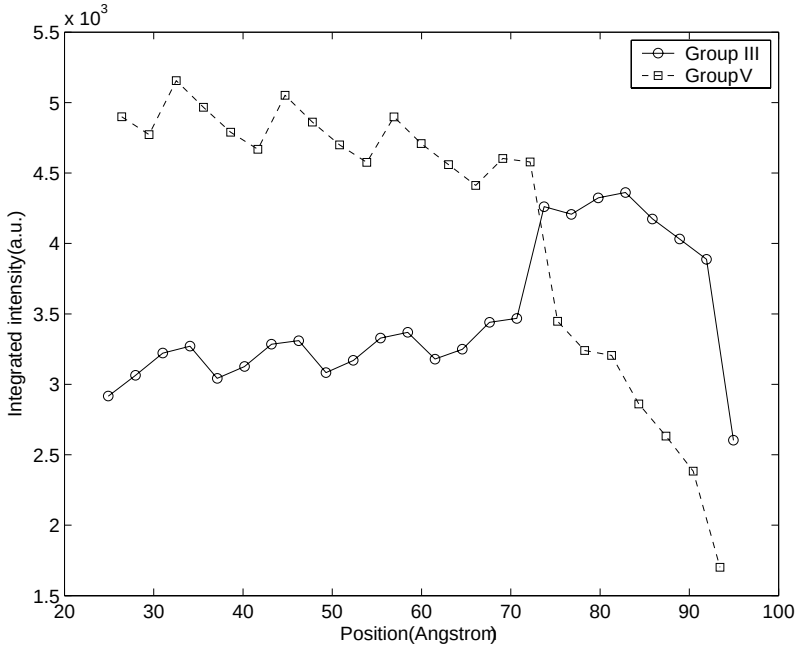

Figure 3.7: Distance between atomic layers of the same type in InAs film on GaSb, sample $r811$

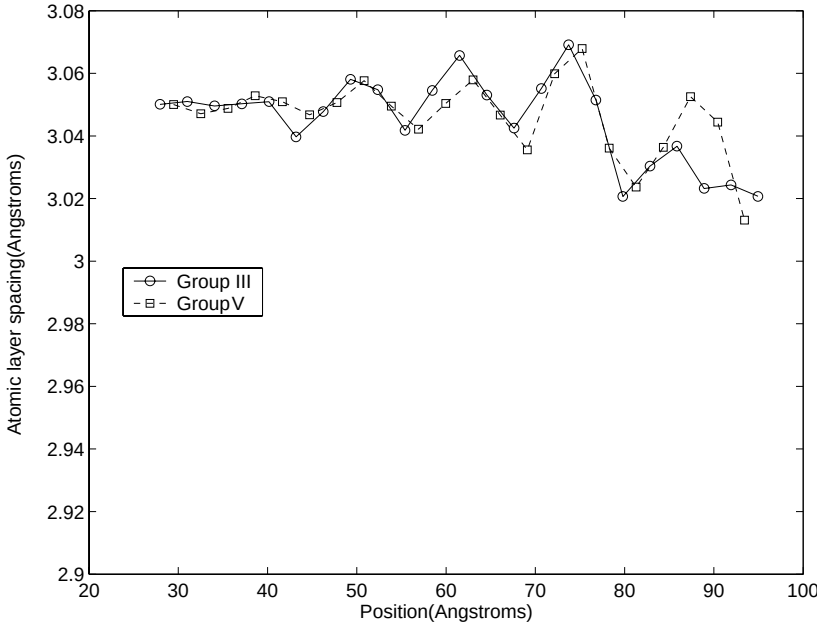

the most relevant, are presented. Only a volume containing 8 substrate unit cells and the film was considered and Figure 3.4 displays the total electron density along the vertical direction. In each unit cell there are two planes for each atomic species. The Figures 3.5(a)–3.5(d) represent vertical line profiles through the electron density containing different atomic sites. Figure 3.6 shows the integrated peak intensity for both group III and V atoms.

Figure 3.7 shows the vertical distance between the same species atomic layers. Since the lattice constant changes with the chemical composition (e.g., Vegard's law), this is an important plot for making assessments of the composition of the film. The correlated noise pattern can be attributed to artifacts introduced by the discontinuity at the borderline with the zero padding regions.

3.6 InAs Film Grown on GaSb Using As_2, Sample $s812$

3.6.1 The Sample

The sample was MBE grown on GaSb substrate with $\langle 001 \rangle$ orientation. The Ga cell temperature was set at $t_{Ga} = 990°\text{C}$ corresponding to a BFM reading of 7.3×10^{-7} torr. The In cell was set at $t_{In} = 855°\text{C}$, corresponding to a BFM value of 3×10^{-7} torr. The bulk temperature of the Sb cell was set at $t_{Sb}^{bulk} = 570°\text{C}$ and the cracker temperature at $t_{Sb}^{cracker} = 900°\text{C}$ giving a BFM reading of 9×10^{-7} torr.

For As, the bulk temperature was set at $t_{As}^{bulk} = 350°\text{C}$ and the cracker temperature was set at $t_{As}^{cracker} = 1000°\text{C}$ to determine a high concentration of As in the dimer state. The BFM reading was 6.3×10^{-6} torr.

A buffer layer of 0.3 μm of GaSb was grown on the substrate to ensure a controlled stoichiometry and a good surface quality. The buffer layer was terminated with one atomic layer of Sb (group V). A total of of 9 monolayers were deposited starting with In (group III). The sample was group V terminated (As). During the growth the

Table 3.5: Rods measured for sample $s812$ and the corresponding L intervals (in reciprocal space units)

Rod index	L_{start}	L_{end}
$00L$	0.1	4.80
$11L$	0.5	3.80
$20L$	0.5	4.30
$22L$	0.5	4.80
$31L$	0.5	4.98
$33L$	0.5	5.25
$40L$	0.5	4.90
$42L$	0.5	5.00
$44L$	0.5	4.60

substrate temperature was set, again, at 450°C.

3.6.2 Experiment

The (400) and (206) reflections were found first. With them, the preliminary orientation matrix was calculated. Next, the following reflections were located with high precision: (115), (202), (200), (244), (131), (311) and (333). Using them, the final orientation matrix was calculated with an optimization algorithm included in the acquisition software.

Table 3.5 lists the rods acquired for this sample and the L limits. A density of 100 points/reciprocal space unit was used, also.

3.6.3 Data Analysis

The reference was generated based on the information presented in Section 3.6. To determine the dominant quadrant, the sum of squares of the differences between the measured data and the intensities corresponding to the total structure factor were evaluated in a 1200 iterations fit for each quadrant configuration, I and II. After the fit, the sum of squares for quadrant I was 2.440 and for quadrant II, 0.541. Rods fit better the second quadrant and therefore the indices considered in the analysis were $00L$, $\bar{1}1L$, $\bar{2}0L$, $\bar{2}2L$, $\bar{3}1L$, $\bar{3}3L$, $\bar{4}0L$, $\bar{4}2L$ and $\bar{4}4L$. The start values of the fit

Table 3.6: Parameters used to generate the reference for sample $s812$, before and after the fit

	UC dist.	Mult. factor factor	in plane DW bulk subs.	vertical DW bulk subs.	DW film	DW explicit subs.	interf. gauss. position	interf. gauss. width
units		RLU^{-1}	RLU^{-1}	RLU^{-1}	RLU^{-1}	UC	UC	
initial	1.000	3.00×10^{-4}	0.0500	0.0500	0.0500	0.0500	2.00	2.00
fit	0.988	3.73×10^{-4}	0.0357	0.0305	0.0324	0.0355	1.75	1.99

parameters and the values that optimize the reference best are listed in Table 3.6.

Once the reference was generated, the phasing procedure was applied. With the new complex structure factor along the measured rods passed as a new reference a new iteration was tried. Unfortunately, the structure factor along the rods got significantly noisier so the result of the first iteration was also the final one. A value of 0.1 rec.UC^{-1} was used for the artificial Debye-Waller factor, for both inplane and vertical directions.

As in the case of the previous sample, the measured data, the reference and the total structure factor (*reference+phasing*) were displayed for all the rods measured experimentally (Figures 3.30–3.38).

Figure 3.8 presents a vertical profile through the total electron density. Figures 3.9(a) and 3.9(b) display the vertical ED profiles through the two group III atomic planes. Figures 3.9(c) and 3.9(d) display the same profiles for group V atoms. From these results, additional plots can be derived. Figure 3.10 represents the integrated values of the ED peaks for group III and group V atoms along a vertical direction. Figure 3.11 represents the evolution of the spacing between consecutive, same group, atoms. As we can see, the lattice parameter evolution along vertical direction (Figure 3.11) is consistent with the case of sample $r811$.

Both the integrated intensity and the atomic spacing plots show signs of correlated noise which can be attributed to the abrupt transition to the zero padding regions

Figure 3.8: The total electron density profile along z in InAs film on GaSb, sample $s812$

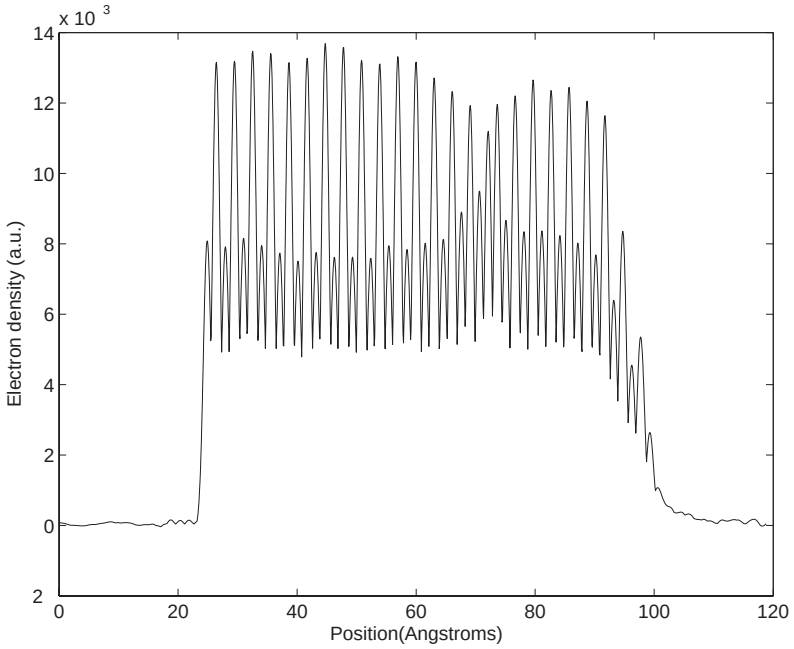

described in the previous chapters.

3.7 GaSb Film Grown on InAs, Sample $p768$

3.7.1 The Sample

The sample was MBE grown on InAs substrate with $\langle 001 \rangle$ orientation. The Ga cell temperature was set at $t_{Ga} = 980°\text{C}$ corresponding to a BFM reading of 7.3×10^{-7} torr. The In cell temperature was set at $t_{In} = 874°\text{C}$ corresponding to a BFM value of 8×10^{-7} torr. The bulk temperature of the Sb cell was set at $t_{Sb}^{bulk} = 600°\text{C}$ and the cracker temperature at $t_{Sb}^{cracker} = 900°\text{C}$ giving a BFM reading of 8×10^{-7} torr.

For As, the bulk temperature was set at $t_{As}^{bulk} = 401°\text{C}$ and the cracker temperature at $t_{As}^{cracker} = 1000°\text{C}$, corresponding to a BFM reading of 3×10^{-6} torr.

0.2 μm of InAs were homoepitaxially grown to ensure a controlled stoichiometry and a good surface quality. The buffer was terminated with one atomic layer of In (group III). 9 monolayers were next deposited starting with Sb (group V). The

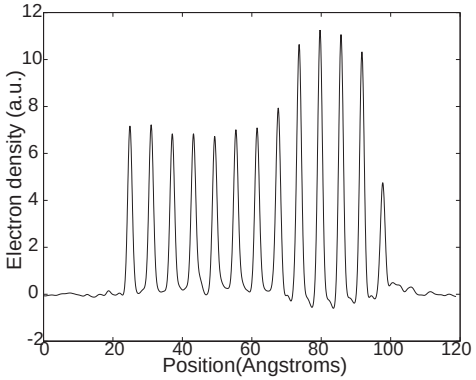

(a) Electron density profile through group III-plane 1

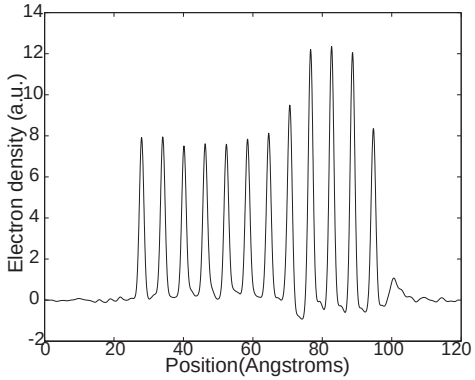

(b) Electron density profile through group III-plane 2

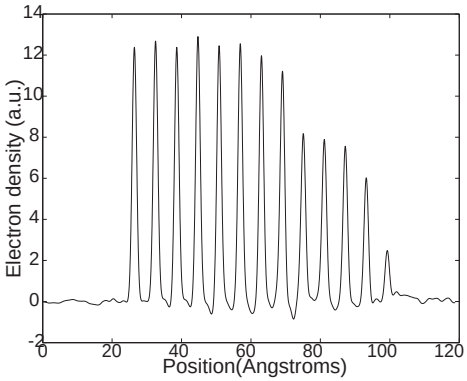

(c) Electron density profile through group V-plane 1

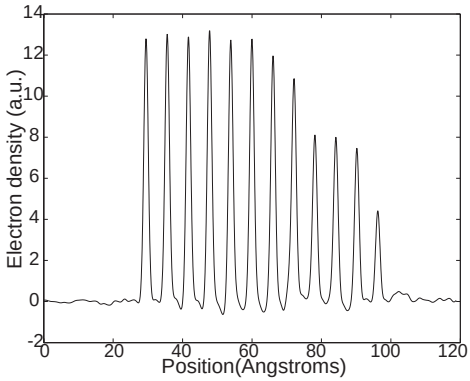

(d) Electron density profile through group V-plane 1

Figure 3.9: Electron density profiles for GaSb film on InAs, sample $s812$

Figure 3.10: Integrated electron density values for InAs film on GaSb, sample $s812$

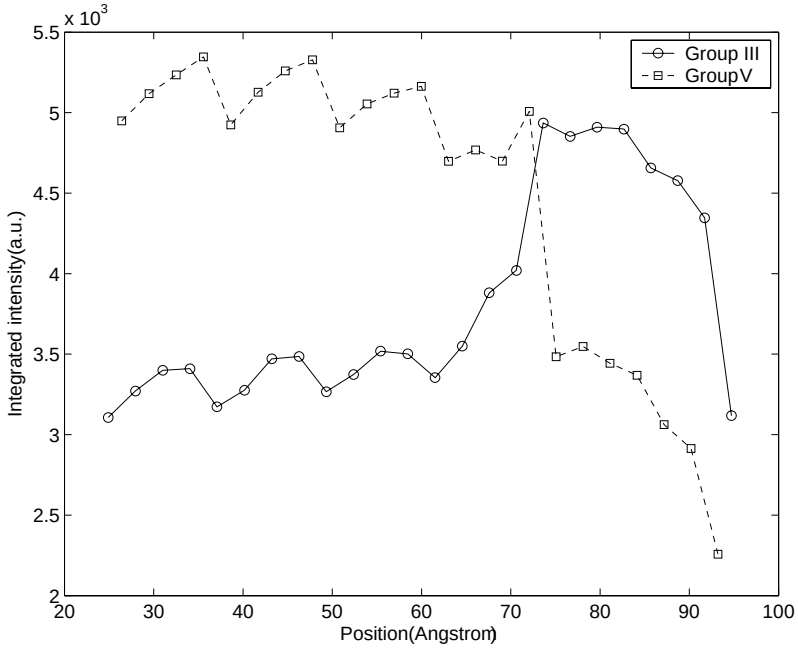

Figure 3.11: Distance between atomic layers of the same type in InAs film on GaSb, sample $s812$

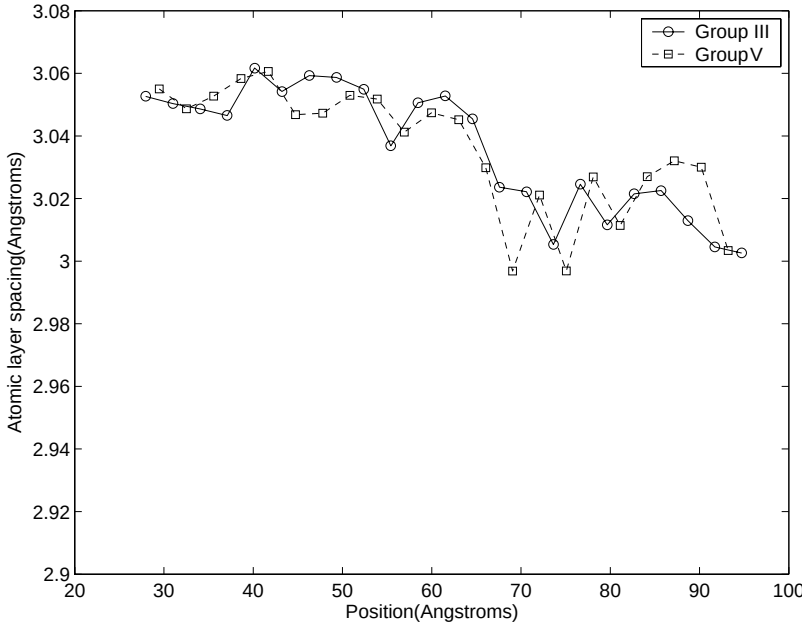

Table 3.7: Rods measured for sample $p768$ and the corresponding L intervals (in reciprocal space units)

Rod index	L_{start}t	L_{end}
$00L$	0.1	4.80
$11L$	0.5	3.80
$20L$	0.5	4.30
$22L$	0.5	4.80
$31L$	0.5	4.98
$33L$	0.5	5.25
$40L$	0.5	4.90
$42L$	0.5	5.00

sample was group V terminated (Sb). During the growth the substrate temperature was set to 450°C.

3.7.2 Experiment

The (400) and (202) reflections were found first. With the orientation matrix obtained the following reflections were optimized: (202) rotated 30° about the incident beam vector, (206), (2$\bar{2}$2), (244), (222), (131) and (311). Again, a precise determination of the orientation matrix was possible.

Table 3.7 lists the rods acquired for this sample and the L limits. Also, a density of 100 points/reciprocal space unit was used.

3.7.3 Data Analysis

To generate the reference, all sample growth information mentioned in Section 3.7 has to be used to describe the structure. To assign a quadrant, the fit was performed assuming the rods in the I and II quadrant successively. The sum of squares for the rods in quadrant I was 0.416 and for rods in quadrant II, 0.866. The rods minimize best the sum of squares when considered in the first quadrant. Therefore, the rod indices considered in the analysis are identical with those listed in Table 3.7. The fit parameters before and after the fits are listed in Table 3.8.

Table 3.8: Parameters used to generate the reference for sample $p768$, before and after the fit

	UC dist.	Mult. factor factor	in plane DW bulk subs.	vertical DW bulk subs.	DW film	DW explicit subs.	interf. gauss. position	interf. gauss. width
units		RLU^{-1}	RLU^{-1}	RLU^{-1}	RLU^{-1}	UC	UC	
initial	1.000	4.00×10^{-4}	0.0500	0.0500	0.0500	0.0500	2.00	2.00
fit	0.958	3.32×10^{-4}	0.0330	0.0345	0.0333	0.0531	3.00	1.52

Figure 3.12: The total electron density profile along z in GaSb film on InAs, sample $p768$

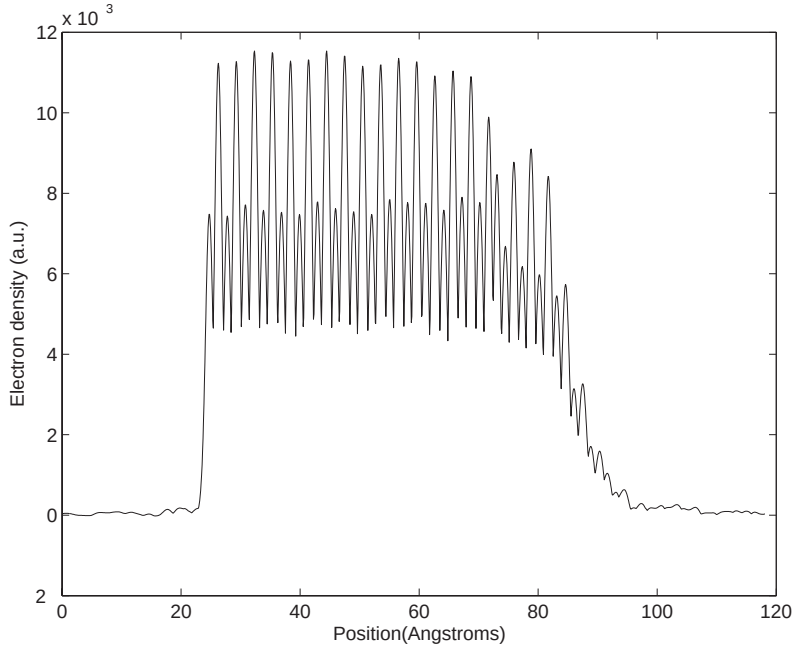

The result of the first phasing iteration is very good, no additional iterations were done. Both the inplane and vertical artificial Debye–Waller factors were set to 0.1 rec.unit cell^{-1}.

Figures 3.39–3.46 display the data and the intensity corresponding to the reference and the final result (phasing+reference). The vertical profile of the total electron density is plotted in Figure 3.12. The substrate–film interface can be evaluated using this plot. In every unit cell there are 2 distinct planes for every atomic species. Figure 3.13(a) and 3.13(b) show vertical ED profile through group III atoms sites on different unit cell planes. Figures 3.13(c) and 3.13(d) present the corresponding

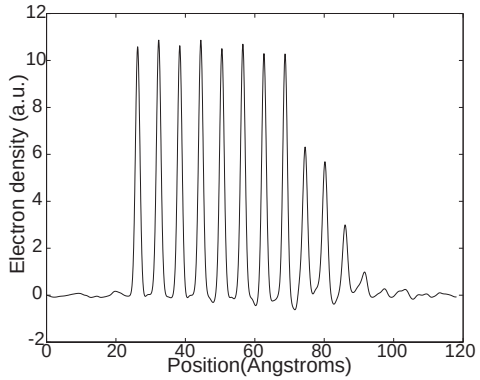

(a) Electron density profile through group III-plane 1

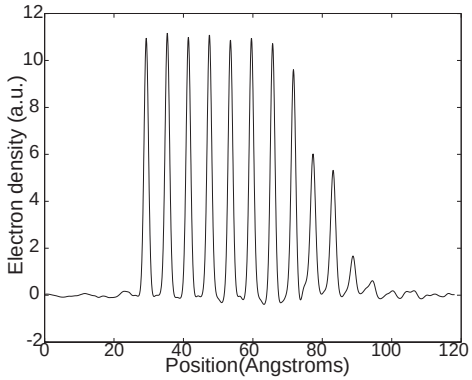

(b) Electron density profile through group III-plane 2

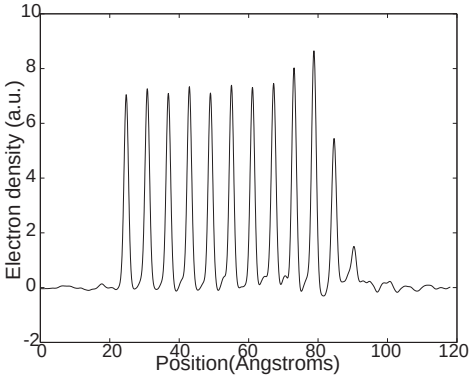

(c) Electron density profile through group V-plane 1

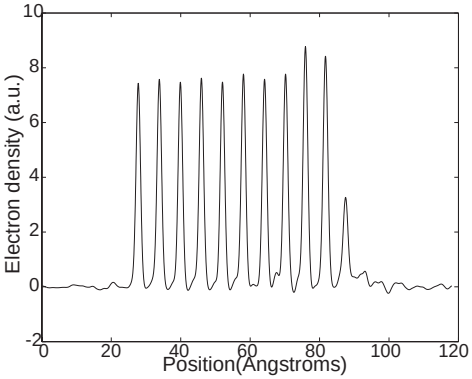

(d) Electron density profile through group V-plane 1

Figure 3.13: Electron density profiles for GaSb film on InAs, sample $p768$

Figure 3.14: Integrated electron density values for GaSb film on InAs, sample $p768$

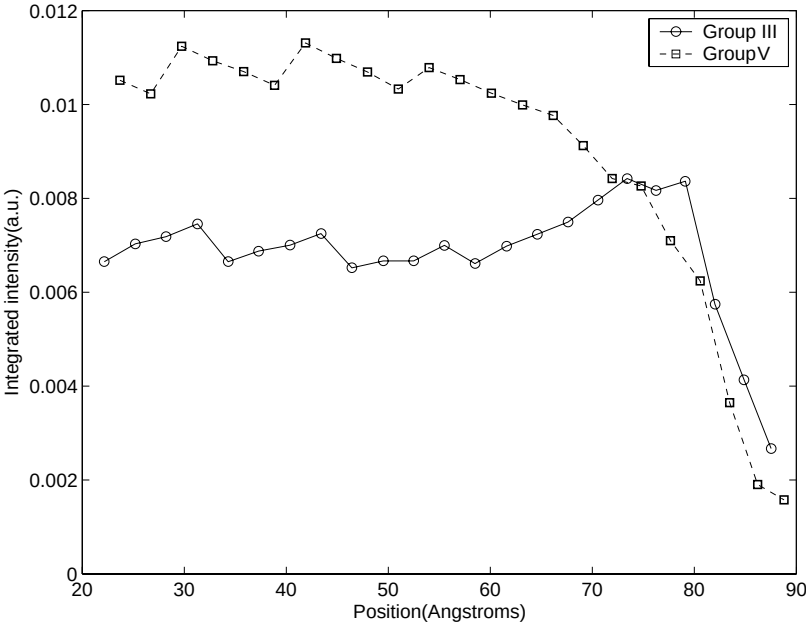

Figure 3.15: Distance between atomic layers of the same type in GaSb film on InAs, sample $p768$

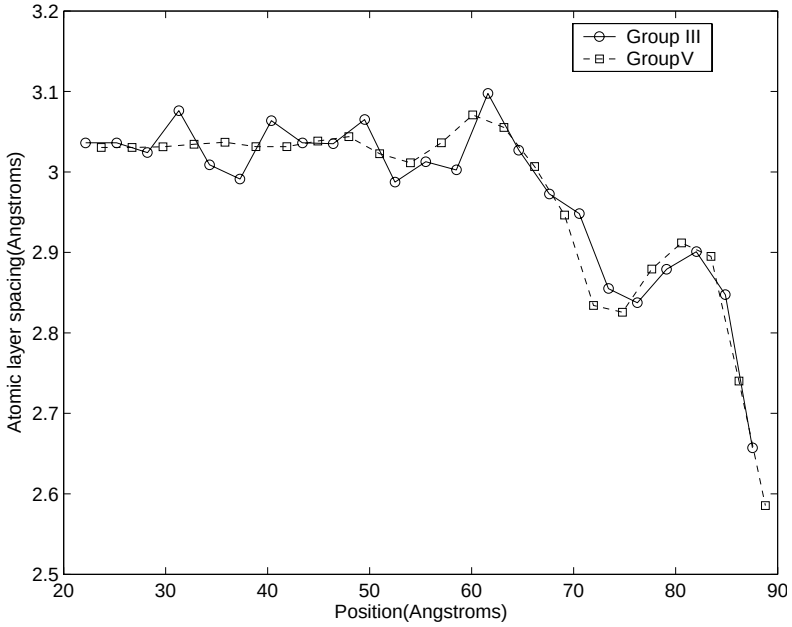

profiles through group V atoms. From the last 4 plots, additional information can be extracted. Figure 3.14 shows the values of the integrated peak intensities for both group III and group V atoms as a function of vertical position. Figure 3.15 displays the spacing between same species atomic planes.

The spacing evolution with vertical position shows a rather unexpected pattern. In the vicinity of the interface, the lattice parameter goes down significantly, below the values corresponding to InAs and GaSb. Considering Vegard's law, this behavior can be explained by the presence of significant amounts of As in the film and a non–uniform distribution profile. Given the high solubility in the quaternary InGaAsSb, the interface region can be thought of as an As rich region. The As concentration goes down toward the surface of the film while it is been replaced by Sb. It is also interesting to note that the lattice constant appears to exhibit a maximum approximately 1.5 unit cells under the surface.

3.8 GaSb Film Grown on InAs, Sample *s*814

3.8.1 The Sample

The sample was MBE grown on InAs substrate with ⟨001⟩ orientation. The Ga cell temperature was set at $t_{Ga} = 990°\text{C}$ corresponding to a BFM reading of 7.3×10^{-7} torr. The In cell temperature was set at $t_{In} = 855°\text{C}$ corresponding to a BFM value of 8×10^{-7} torr. The bulk temperature of the Sb cell was set at $t_{Sb}^{bulk} = 570°\text{C}$ and the cracker temperature at $t_{Sb}^{cracker} = 900°\text{C}$ giving a BFM reading of 9×10^{-7} torr.

For As, the bulk temperature was set at $t_{As}^{bulk} = 350°\text{C}$ and the cracker temperature at $t_{As}^{cracker} = 1000°\text{C}$, corresponding to a BFM reading of 2.6×10^{-6} torr and a flux consisting mainly in As_2.

A buffer layer of 0.2 μm of InAs was grown first. It was terminated with one atomic layer of In (group III). 9 monolayers were next deposited starting with Sb (group

Table 3.9: Rods measured for sample $s814$ and the corresponding L intervals(in reciprocal space units)

Rod index	L_{start}	L_{end}
$00L$	0.1	4.80
$11L$	0.5	3.80
$20L$	0.5	4.30
$22L$	0.5	4.80
$31L$	0.5	4.95
$33L$	0.5	5.25
$40L$	0.5	4.90
$42L$	0.5	4.90
$44L$	0.5	4.57

V). The sample was group V terminated (Sb). During the growth the substrate temperature was set to 450°C.

3.8.2 Experiment

The (400) and (206) reflections were found first. With the preliminary orientation matrix obtained, the following reflections were optimized: (115), (202), (200), $(1\bar{1}5)$, (244), (131), (311) and (333).

Table 3.9 lists the rods acquired for this sample and the L limits. The rods were scanned with a density of 100 points/reciprocal space unit.

3.8.3 Data Analysis

A reference was generated based on the growth and structural information described in detail in Section 3.8. To identify the quadrant, a fit was tried considering the rods in each quadrant, I and II. After 1200 iterations the sum of the squares of the differences between the data and the simulated reference were 0.704 for the rods in quadrant I and 0.532 for rods in quadrant II. Therefore, the reference considers all the rods in quadrant I and their indices are listed in Table 3.9. The start and final values for the reference parameters are listed in Table 3.10.

For the artificial Debye-Waller factors, a value of 0.07 rec.unit cell^{-1} was used.

Table 3.10: Parameters used to generate the reference for sample $s814$, before and after the fit

	UC dist.	Mult. factor factor	in plane DW bulk subs.	vertical DW bulk subs.	DW film	DW explicit subs.	interf. gauss. position	interf. gauss. width
units		RLU^{-1}	RLU^{-1}	RLU^{-1}	RLU^{-1}	UC	UC	
initial	1.000	4.00×10^{-4}	0.0500	0.0500	0.0500	0.0500	2.00	3.00
fit	0.984	2.55×10^{-4}	0.0291	0.0306	0.0303	0.0431	3.00	1.52

Figure 3.16: The total electron density profile along z in GaSb film on InAs, sample $s814$

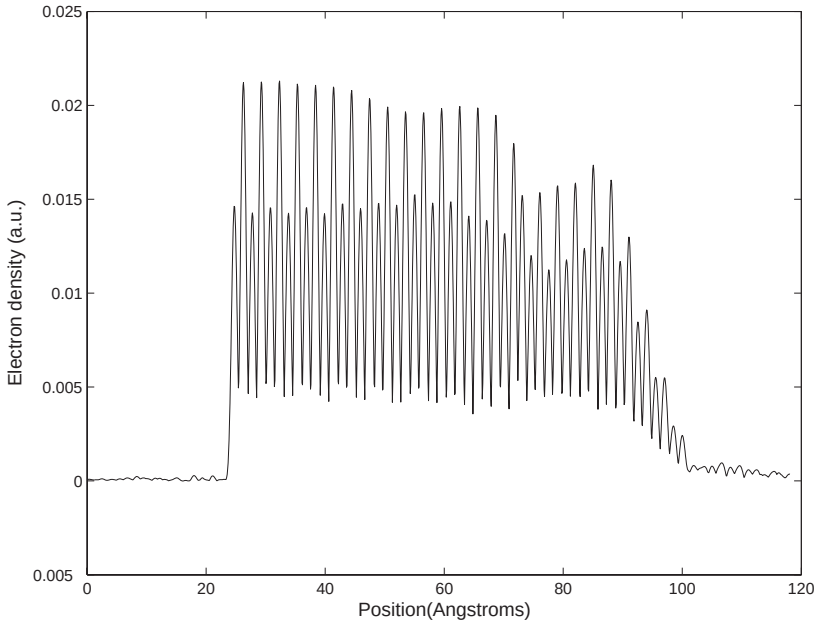

The complex structure factor obtained after the first phasing iteration was input as reference and another phasing iteration was performed to get the final result.

Figures 3.47–3.55 show the data, the reference and the intensity corresponding to the final structure factor. Figure 3.16 displays the total electron density profile along the vertical direction. Figures 3.17(a)–3.17(d) represent vertical profiles through different atomic sites in the unit cell; Figure 3.18 shows the values of the integrated electron density peaks and Figure 3.19–the spacing between same species atomic planes.

As in the case of previous sample, the atomic plane spacing exhibits a dip; the

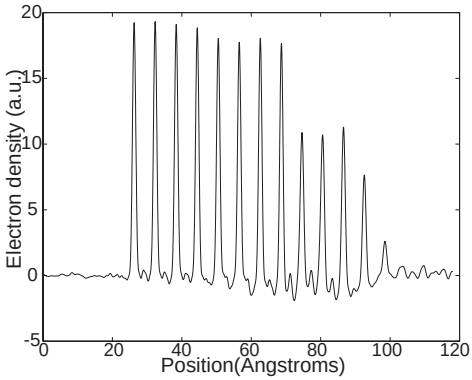

(a) Electron density profile through group III-plane 1

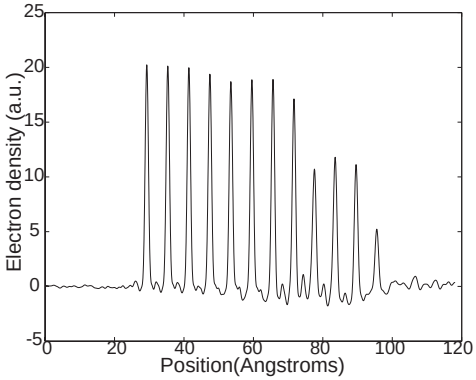

(b) Electron density profile through group III-plane 2

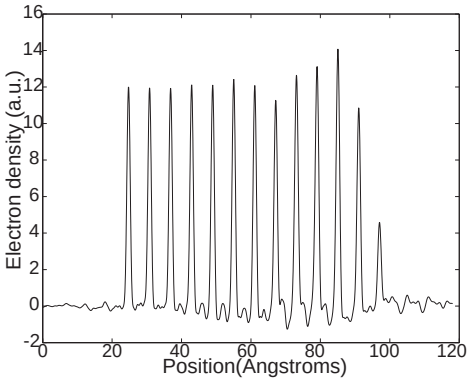

(c) Electron density profile through group V-plane 1

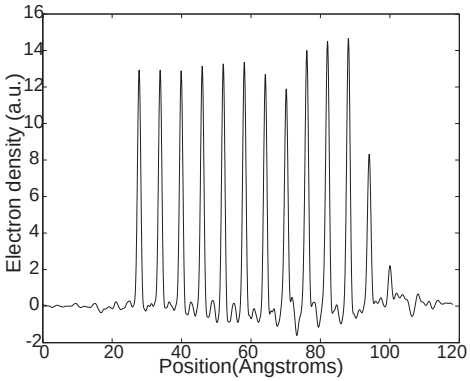

(d) Electron density profile through group V-plane 1

Figure 3.17: Electron density profiles for GaSb film on InAs, sample $s814$

Figure 3.18: Integrated electron density values for GaSb film on InAs, sample *s*814

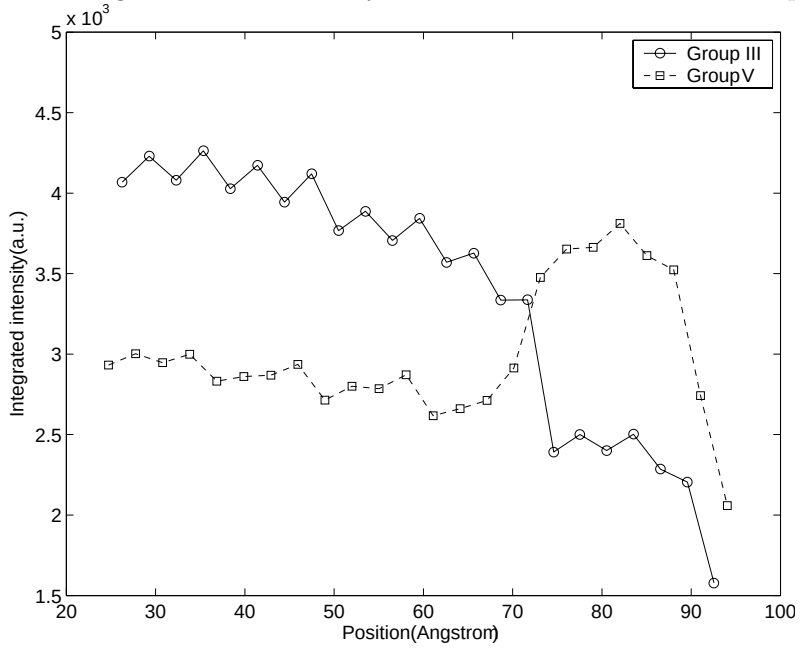

Figure 3.19: Distance between atomic layers of the same type in GaSb film on InAs, sample *s*814

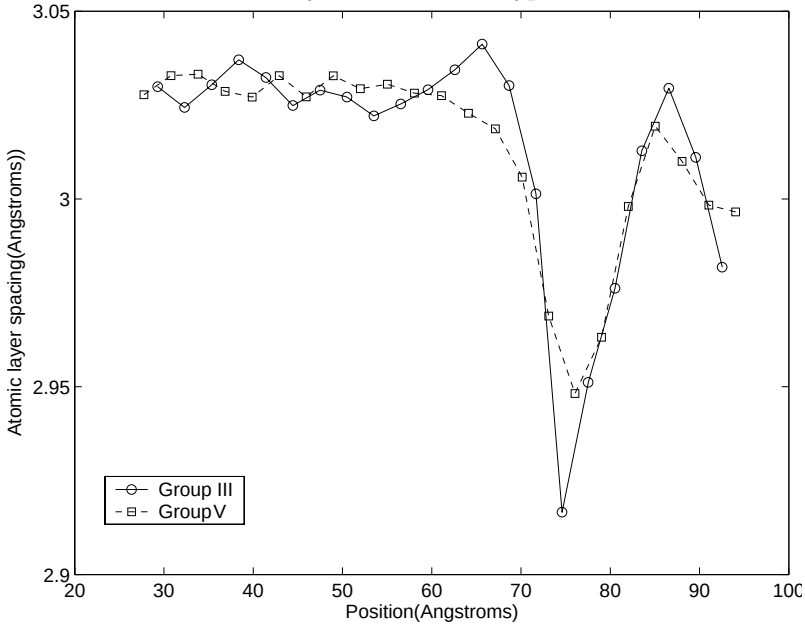

only chemical species that can induce such behavior is As. The lattice spacing is consistent with a quaternary film composition in the vicinity of the substrate. As in the case of the previous sample, it exhibits a maximum at 1.5 unit cells below the surface.

3.9 Algorithm Used to Extract the Stoichiometry

The outcome of the COBRA technique is the total electron density. Since the interfacial region is also affected by roughness, the integrated value of the ED peaks will have an additional factor to the Z value, given by the partial occupancy and intermixing. The last phenomenon is particularly important in the case of the materials investigated, due to their high solubility in the quaternary $Ga_mIn_{1-m}As_nSb_{1-n}$ [55], with $m, n \in [-1, 1]$.

The fit of the ED peaks returns the true value of the lattice constant. However, to be able to use Vegard's law, we need to calculate the values of the lattice constant corresponding to the fully relaxed film. To do the correction we rely on the assumption that the film is under elastic strain. We will, therefore, assume that the film will preserve the in–plane component of the substrate lattice constant. The corrected value of the unit cell will be given by:

$$a(z) = \sqrt[3]{a_{subs}^2 \cdot a_s(z)} \tag{3.8}$$

where $a(z)$ is the lattice value of the relaxed film, a_{subs}–the lattice constant of the substrate and $a_s(z)$–the measured lattice constant, of the stressed film.

An additional equation to use is given by Vegard's law. We will regard the whole volume of the sample considered explicitly as a quaternary, with $m = m(z)$ and $n = n(z)$ having a functional dependence on vertical position. Vegard's law can thus

be written as:

$$a(m,n) = a_{GaAs}\, mn + a_{InAs}(1-m)\, n + a_{GaSb}\, m(1-n) + a_{InSb}(1-m)(1-n) \quad (3.9)$$

where $a(m,n)$ is the lattice constant of the quaternary alloy at the particular position, $a_{GaAs} = 5.6533\,\text{Å}$ is the lattice constant of bulk GaAs, $a_{InAs} = 6.0584\,\text{Å}$ the lattice constant of InAs, $a_{GaSb} = 6.0959\,\text{Å}$ and $a_{InSb} = 6.0959\,\text{Å}$–the lattice constant of InSb.

As a general assumption for the quaternary alloy we will assume that intermixing occurs only between group III atoms (In, Ga) and only between group V atoms (As, Sb), but a group III atom will never go in a group V site. Also, we will consider that both atomic layers in a monolayer have the same occupancy. With these assumptions, the amplitudes of the ED peaks will satisfy:

$$m \cdot Z_{Ga} + (1-m) \cdot Z_{In} = \frac{A_{Gr_{III}}}{f} \quad (3.10)$$

and

$$n \cdot Z_{As} + (1-n) \cdot Z_{Sb} = \frac{A_{Gr_V}}{f} \quad (3.11)$$

The quantity $f \in [0,\, 1]$ is the effective value of the occupancy; $Z_{Ga} = 26.34$, $Z_{In} = 49.06$, $Z_{As} = 31.27$ and $Z_{Sb} = 51.06$– the effective number of electrons for the corresponding atoms at the energy of 11.40 keV; $A_{Gr_{III}}$ and A_{Gr_V}–the integrated amplitudes of the ED corresponding to the group III atoms and group V, respectively.

Using the ED yielded by the Coherent Bragg Rod Analysis we can determine the values of the lattice constant and the integrated amplitudes of the ED peaks for groups III and V. The unknown variables are the occupancy f and the fractions $m(z)$ and $n(z)$. Their values can be determined using Equations 3.9–3.11.

A common feature of all the plots in Figure 3.21 is that the results tend to be inaccurate toward the surface. This is particularly true in the case of sample $p768$

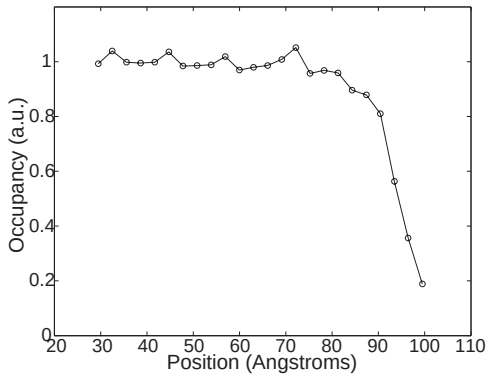

(a) InAs film on GaSb, grown with As_4, sample $r811$

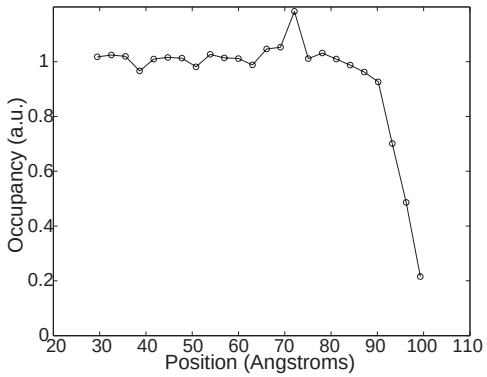

(b) InAs film on GaSb, grown with As_2, sample $s812$

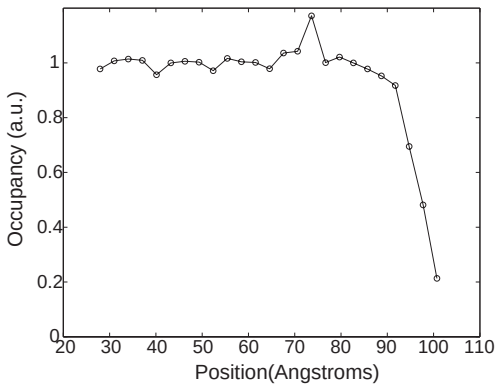

(c) GaSb film on InAs, sample $p768$

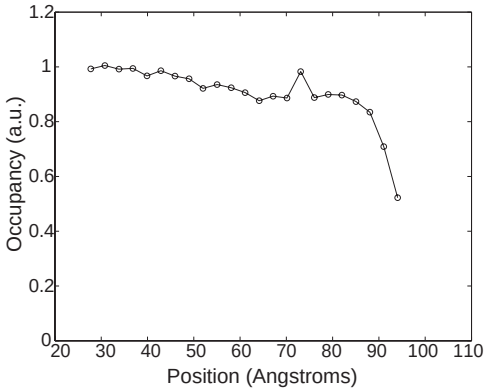

(d) GaSb film on InAs, sample $s814$

Figure 3.20: Vertical occupancy profiles

where the values of $m(z)$ become significantly higher than 1. This might be explained by the fact that the values of the amplitude and lattice constant needed to extract the chemical composition of the sample using Equations 3.9–3.11 are based on fitting the ED peaks that approach small amplitudes toward the surface due to roughness. The imprecision in evaluating the position and amplitude of the peaks increases dramatically as their amplitudes get close to the noise level.

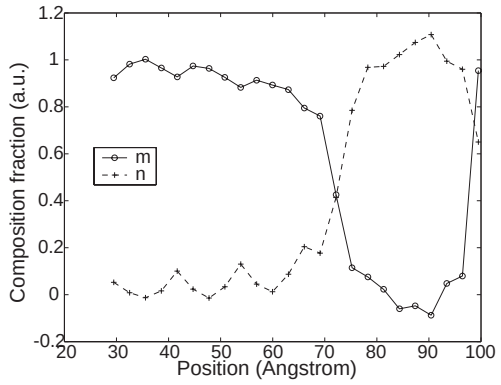

(a) InAs film on GaSb, grown with As_4, sample $r811$

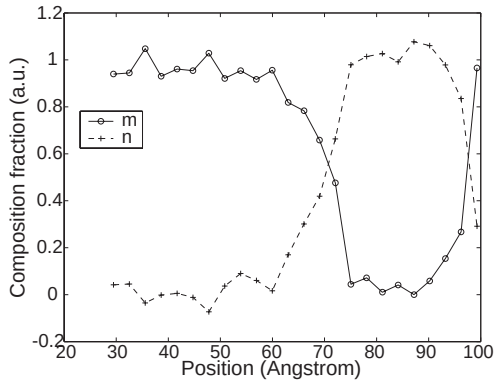

(b) InAs film on GaSb, grown with As_2, sample $s812$

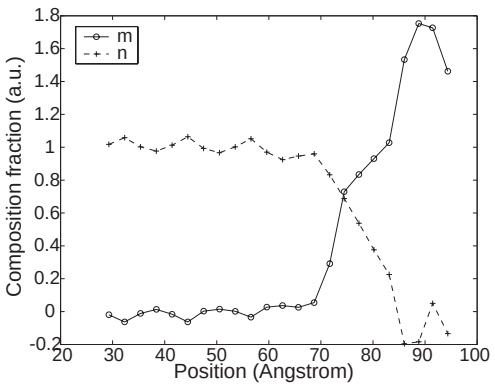

(c) GaSb film on InAs, sample $p768$

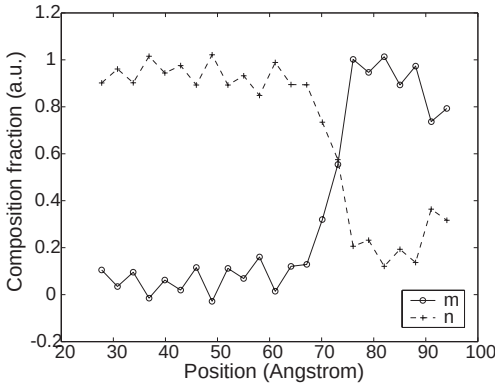

(d) GaSb film on InAs, sample $s814$

Figure 3.21: Composition of different samples regarded as $Ga_mIn_{1-m}As_nSb_{1-n}$

3.10 Calculation of the Roughness

The occupancy values for each monolayer can be extracted from the Equation 3.9–3.11. Surface scientists, however, do not commonly use this type of plot to describe the surface morphology. What is usually measured–using scanning probe microscopes–is the root mean square (RMS) surface roughness, defined as:

$$RMS = \sqrt{\overline{z^2} - \overline{z}^2} \tag{3.12}$$

where the average is taken over the sample surface considered. A function that described the area as a function of the height z can be defined as

$$\rho(z) = -\frac{dA}{dz} \tag{3.13}$$

and with it we can calculate the quantities used in the calculation of the RMS roughness in Equation 3.12:

$$\overline{z} = \int_{-\infty}^{+\infty} z\rho(z)dz, \quad \overline{z^2} = \int_{-\infty}^{+\infty} z^2\rho(z)dz \tag{3.14}$$

The increase in the occupancy, for a particular value of the vertical position z, is proportional to the increase of the surface area terminated at that particular value

$$df(z) = \frac{dA}{A} = -\rho(z)dz \tag{3.15}$$

and, therefore, we can extract the functional form of $f(z)$ that will, ultimately, characterize the surface roughness:

$$\rho(z) = -\frac{df(z)}{dz} \tag{3.16}$$

As described in Equation 3.16, the surface height distribution function can be characterized as the derivative of the occupancy profile along the vertical direction.

The sampling density of occupancy values is low, given by the monolayer spacing, and does not allow a complete reconstruction of the functional dependence of $\rho(z)$. A practical approach is to assume a known profile–gaussian, for example– and try to fit it in order to extract the significant parameters ($\overline{z}$ and the RMS, if the profile is assumed gaussian). However, the number of available points–in the vertical occupancy profile–relevant to this operation is small and the results are very likely to be inaccurate.

3.11 Interpretation of Results

The behavior of the InAs films grown on GaSb is consistent in both samples. Considering an elastic behavior, the expected value for the lattice parameter is 5.98 Å, corresponding to a spacing of between same species atomic planes of 2.99 Å. Thus, the lattice parameter the film aligns closely to the expected value for the InAs coherently grown on GaSb. In Figure 3.7 significant presence of correlated noise is observed. This is caused by the existence of the separation regions between the volume in which the rods were calculated explicitly and the zero padding volume. Unfortunately, data toward the surface are unreliable and the study can neither confirm nor deny the presence of the peak in In composition predicted by the kinetic model of Dehaese et al in Ref. [60].

The composition fractions $m(z)$ and $n(z)$ are relatively similar in both *r811* and *s812* samples, with the proviso that the group III profile (Ga–In) shows a somewhat larger transition region between film and substrate. In the case of the film grown with As_4, there is a slight tail of In in the substrate, perhaps due to the difference in As incorporation. The As content varies as expected, zero in the GaSb substrate, increases in the interfacial region and reaches unity in the InAs film. However, the

film appear to be less intermixed than the GaSb on InAs.

Both GaSb films grown on InAs exhibit significant As presence in the film. The effect is strong in the behavior of the lattice constant described by Figures 3.15 and 3.19. The concentration is proved to be significant in sample *s814*, for which the chemical composition was resolved (Figure 3.21). The origin of the As is most likely due to a high vapor pressure in the deposition chamber. As expected, the film composition near the substrate confirms the presence of the quaternary alloy GaInAsSb. The same composition is observed in the near-surface region. The fact is not surprising as In is known to surface segregate [60].

One of the effects of the lattice constant variation with z position is the stress nonuniformity. The interesting behavior comes from the fact that the value of the lattice constant reaches a minimum approximately 1.5 unit cells below the surface. The film is subject to tensile stress (the lattice constant in the film is smaller in the film than in the substrate) which is non–uniform. The maximum mismatch with the substrate is of the order of $\sim 2.4\%$ distributed across a few monolayers.

3.12 Data and Fits

3.12.1 InAs Film, Sample *r811*

For all the rods–except 00–the sample $\langle 100 \rangle$ axis was set along a fixed axis given by [0.05369, -0.99721, -0.05185]. This gave a fixed angle of 3.7° between the beam and the [100] plane. For rod $00L$ sample $\langle 010 \rangle$ axis was oriented along the fixed axis [0.707109, 0, 0.707104].

Figure 3.22: Rod $00L$ of InAs film on GaSb, sample r811

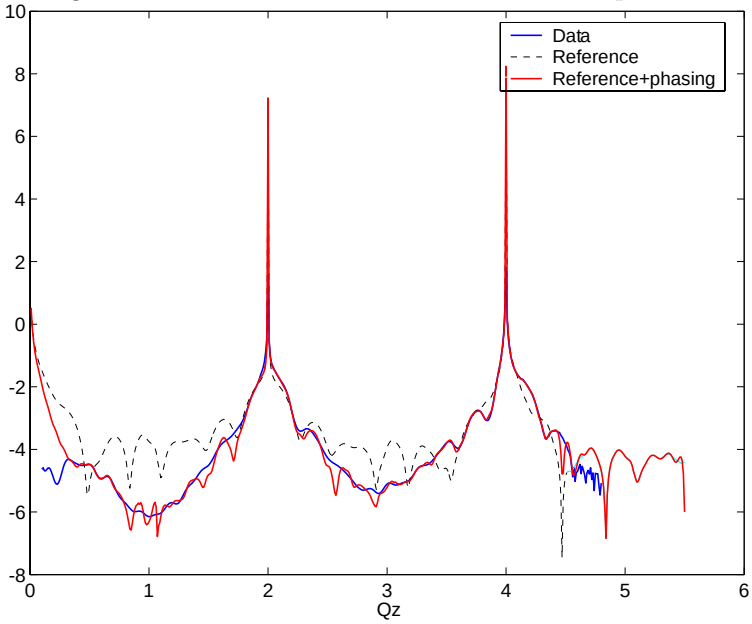

Figure 3.23: Rod $-11L$ of InAs film on GaSb, sample r811

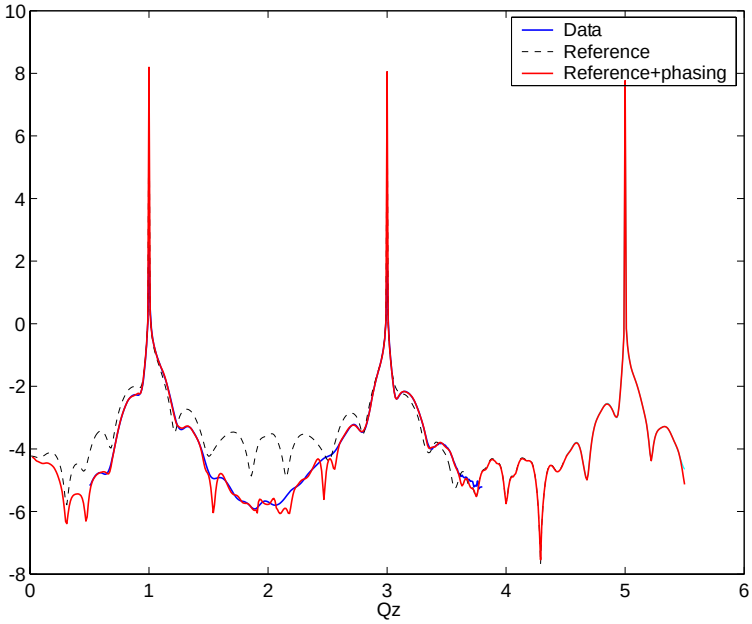

Figure 3.24: Rod $-20L$ of InAs film on GaSb, sample r811

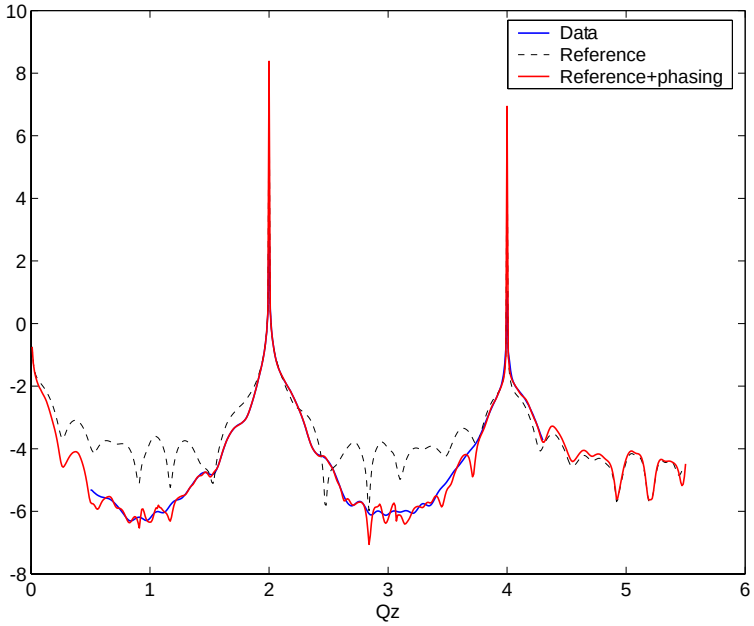

Figure 3.25: Rod $-22L$ of InAs film on GaSb, sample r811

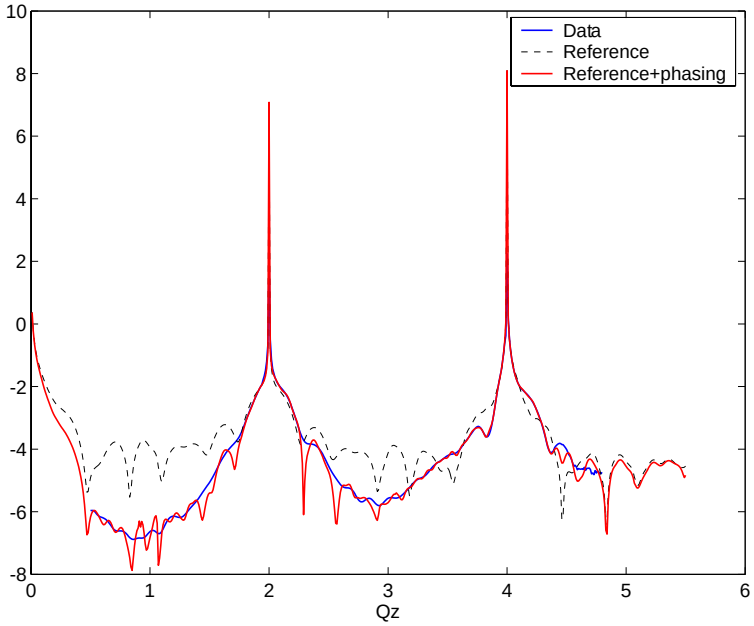

Figure 3.26: Rod $-31L$ of InAs film on GaSb, sample r811

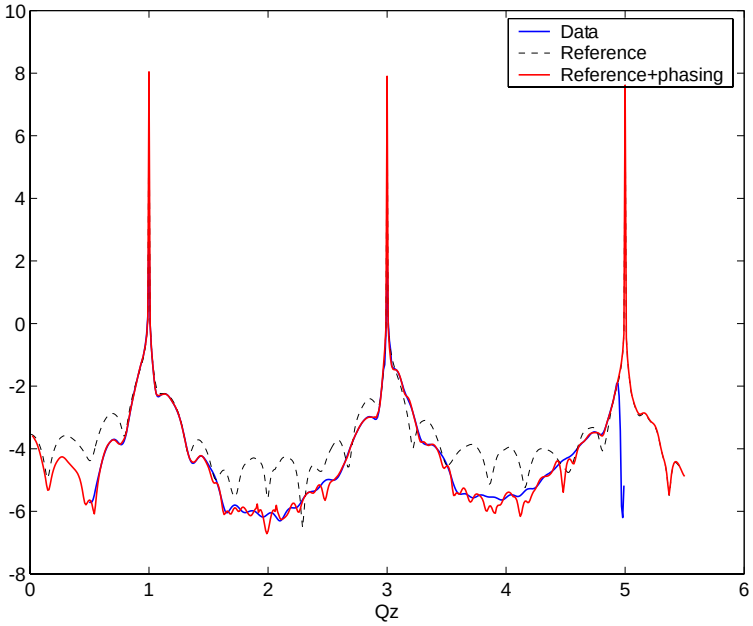

Figure 3.27: Rod $-33L$ of InAs film on GaSb, sample r811

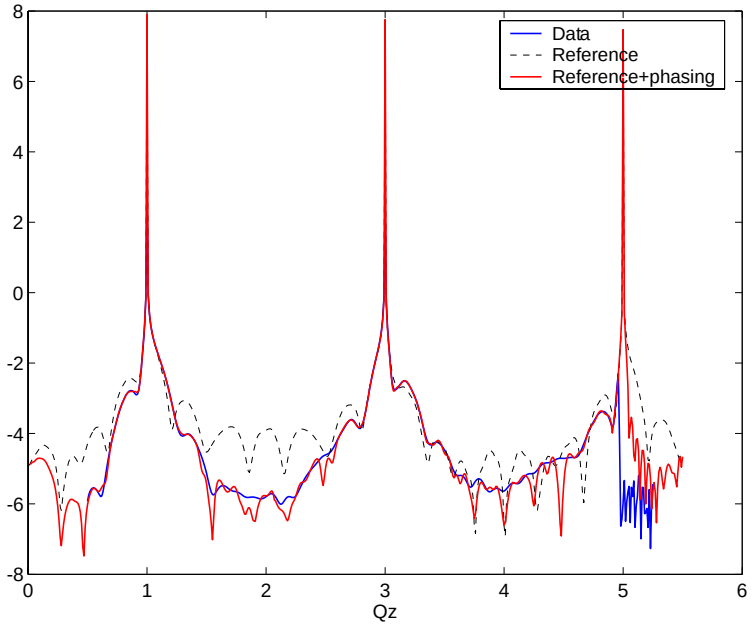

Figure 3.28: Rod $-40L$ of InAs film on GaSb, sample r811

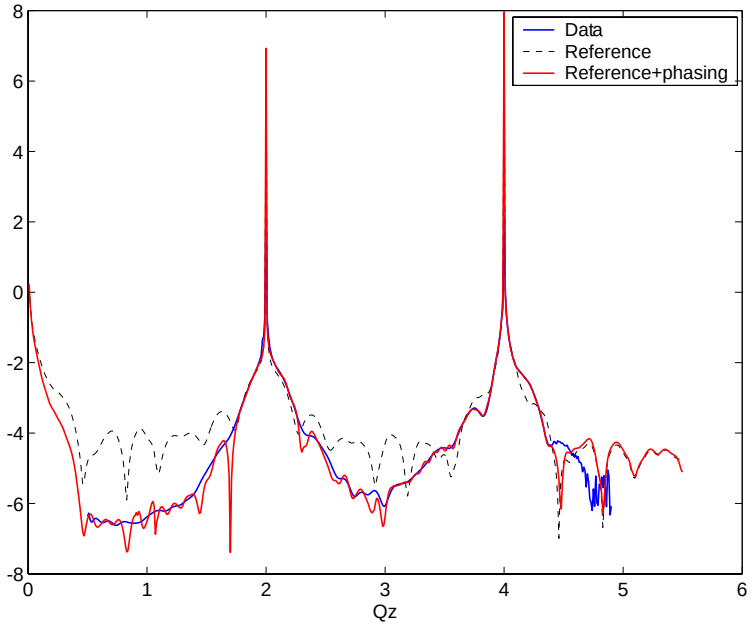

Figure 3.29: Rod $-42L$ of InAs film on GaSb, sample r811

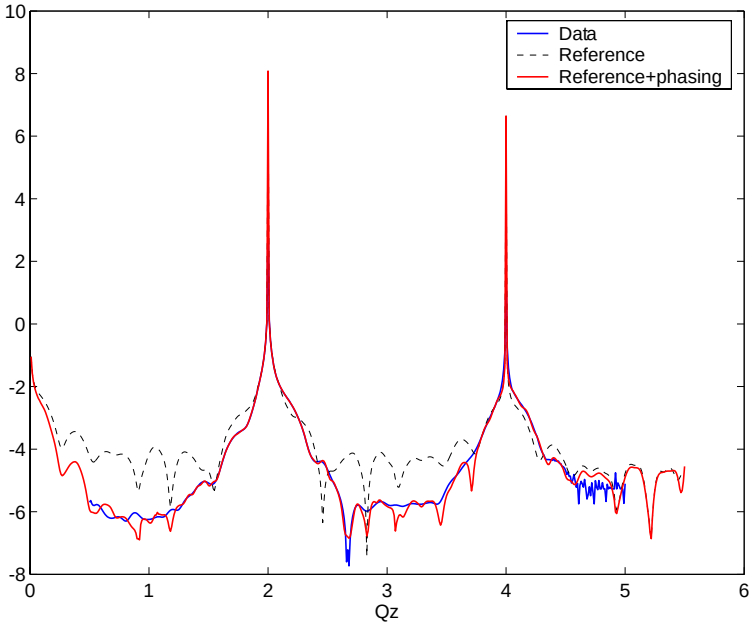

3.12.2 InAs Film, Sample *s812*

For all the rods–except 00–the normal was set along a fixed axis given by [0.0504, -0.9975, -0.05038] giving a fixed angle of 3.5° between the incident beam and sample (100) planes. For rod 00L sample $\langle 010 \rangle$ axis was oriented along the fixed axis [0.7071, 0, 0.7071].

Figure 3.30: Rod 00L of InAs film on GaSb, sample s812

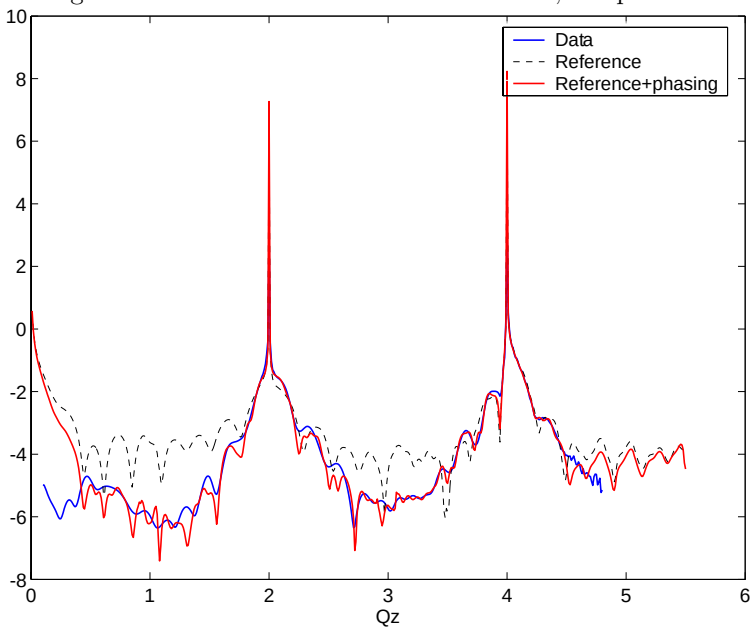

Figure 3.31: Rod $-11L$ of InAs film on GaSb, sample s812

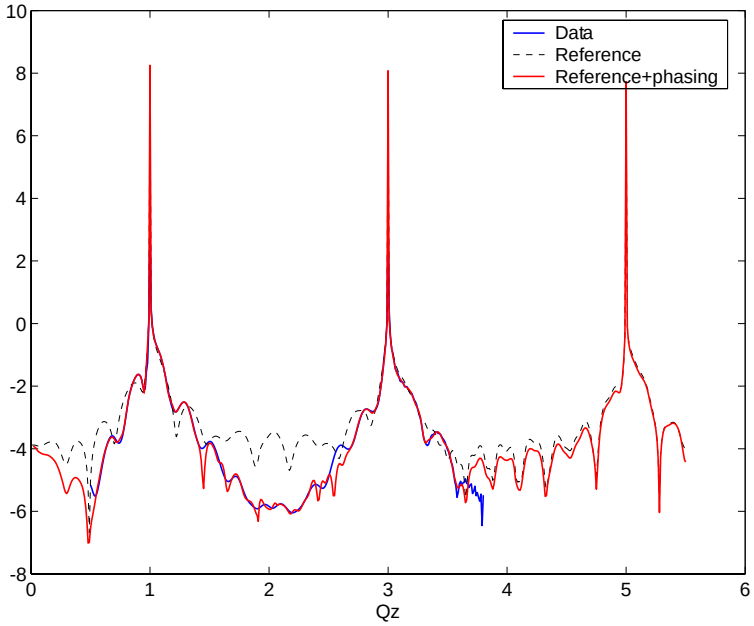

Figure 3.32: Rod $-20L$ of InAs film on GaSb, sample s812

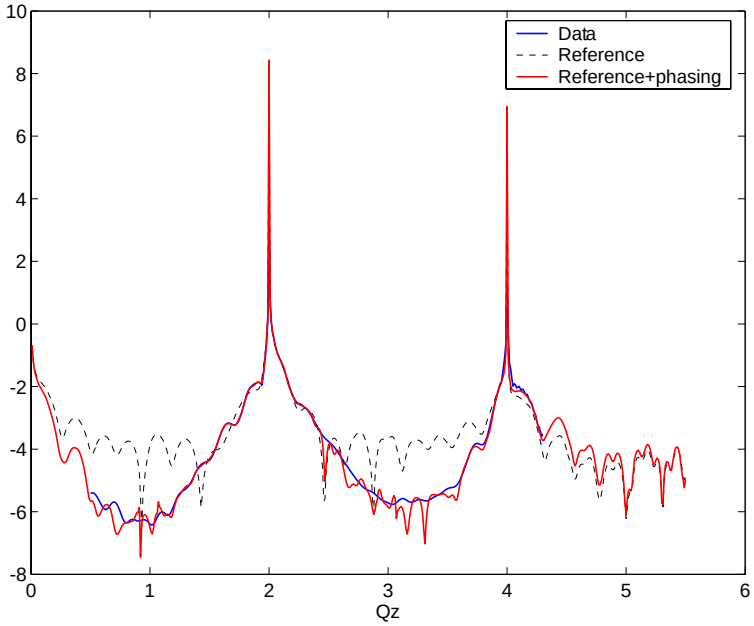

Figure 3.33: Rod $-22L$ of InAs film on GaSb, sample s812

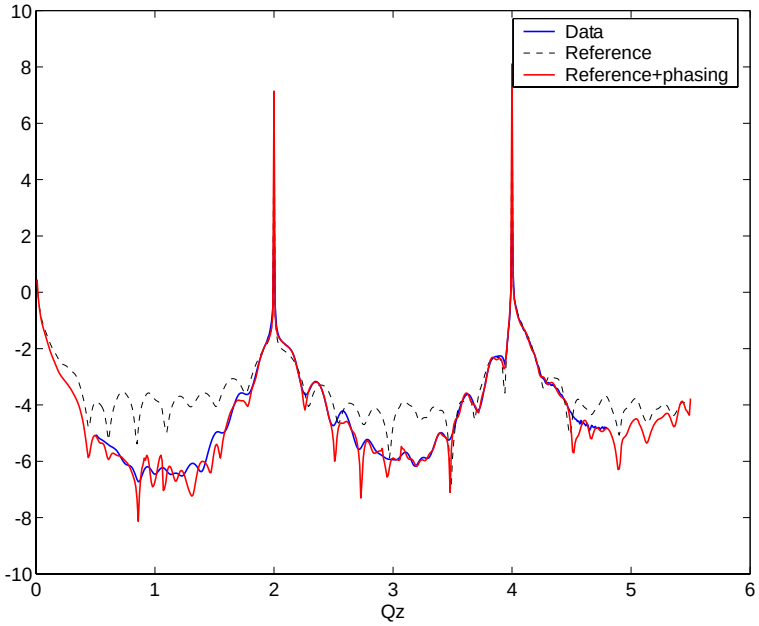

Figure 3.34: Rod $-31L$ of InAs film on GaSb, sample s812

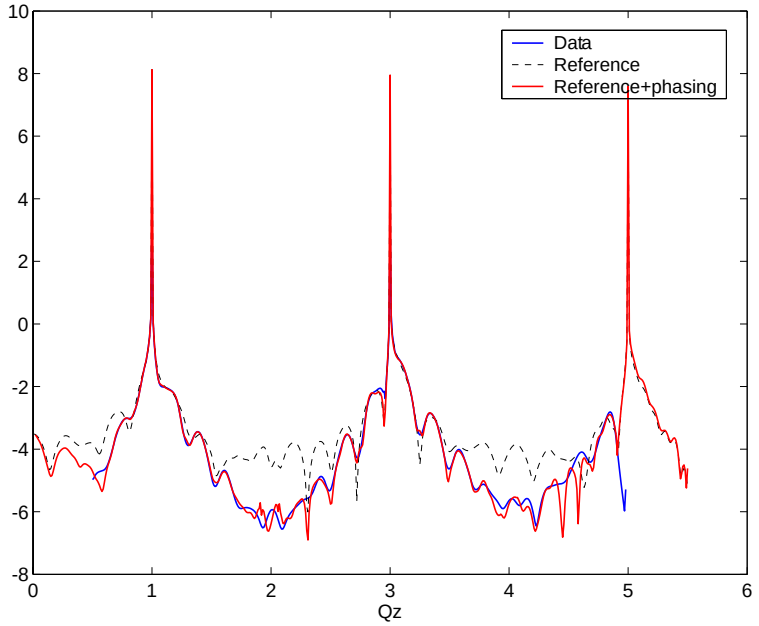

Figure 3.35: Rod $-33L$ of InAs film on GaSb, sample s812

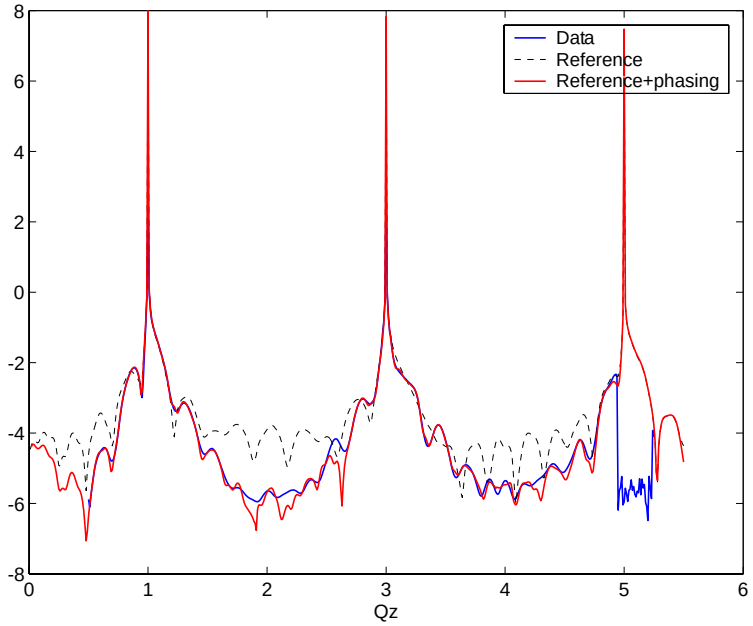

Figure 3.36: Rod $-40L$ of InAs film on GaSb, sample s812

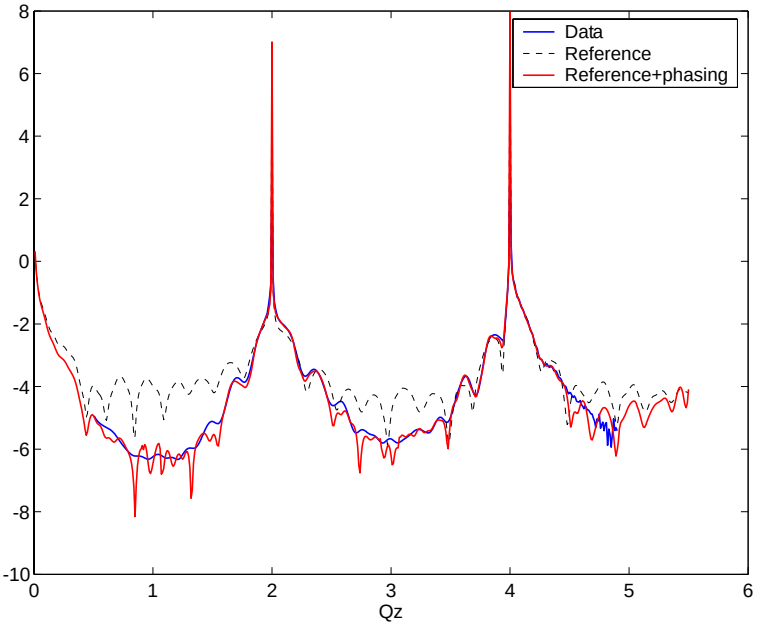

Figure 3.37: Rod $-42L$ of InAs film on GaSb, sample s812

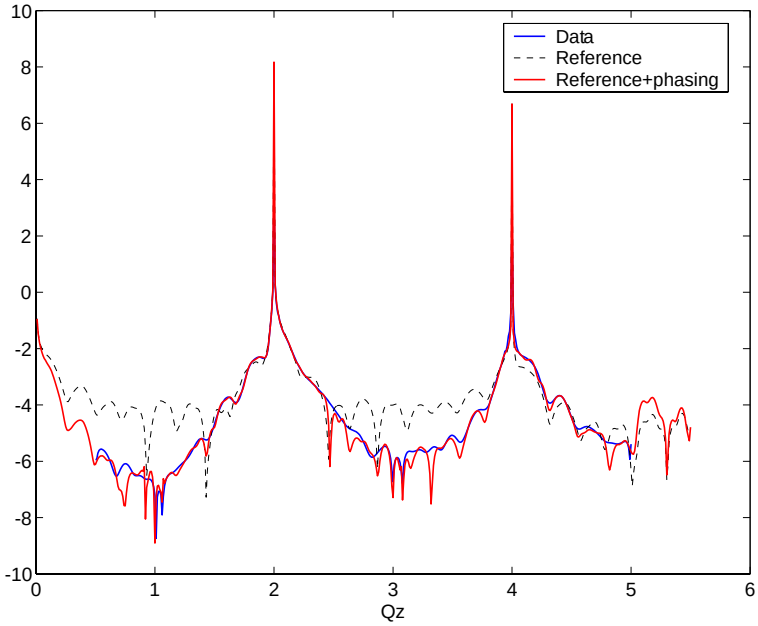

Figure 3.38: Rod $-44L$ of InAs film on GaSb, sample s812

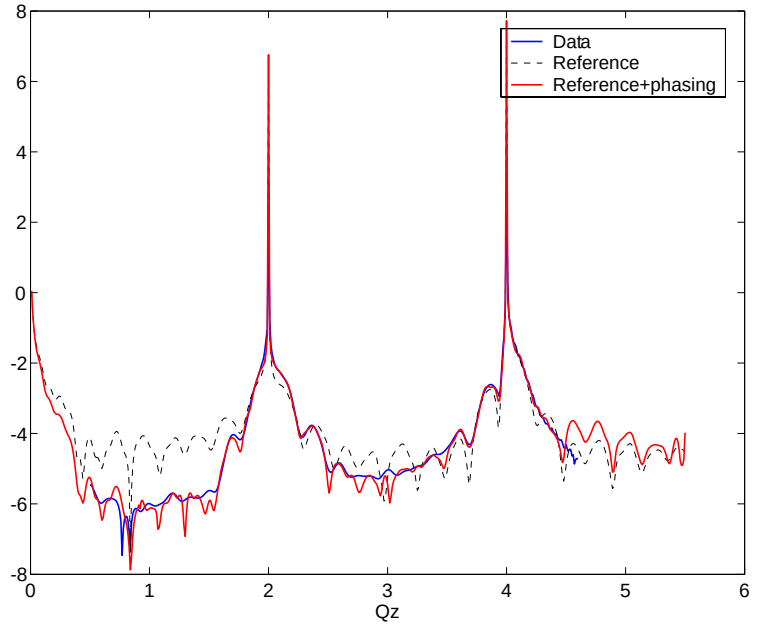

3.12.3 GaSb Film, Sample *p768*

For all the rods different than $00L$ the sample $\langle 100 \rangle$ axis was set along a fixed axis given by [0.0537, -0.9972, -0.05185]. This gave a fixed angle of 3.7° with the sample [100] plane. For rod $00L$ sample $\langle 010 \rangle$ axis was oriented along the fixed axis [0.7071, 0, 0.7071].

Figure 3.39: Rod $00L$ of GaSb film on InAs, sample p768

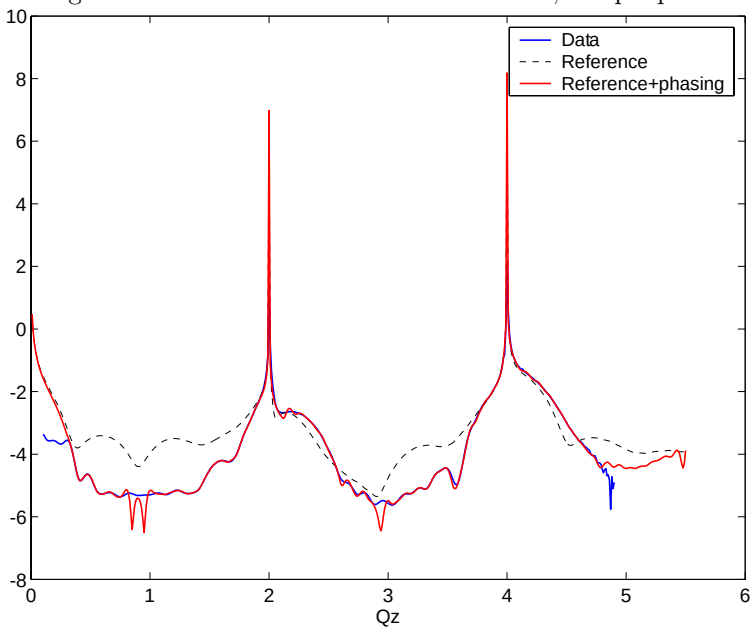

Figure 3.40: Rod 11L of GaSb film on InAs, sample p768

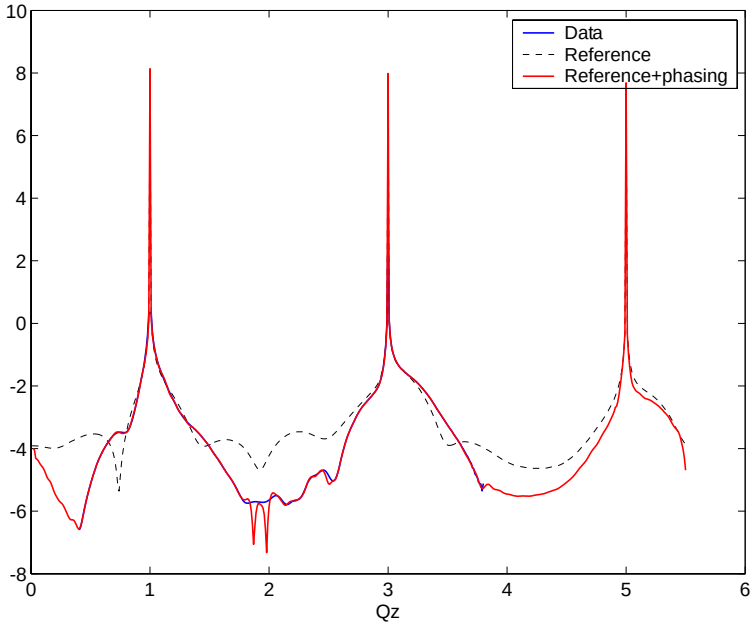

Figure 3.41: Rod 20L of GaSb film on InAs, sample p768

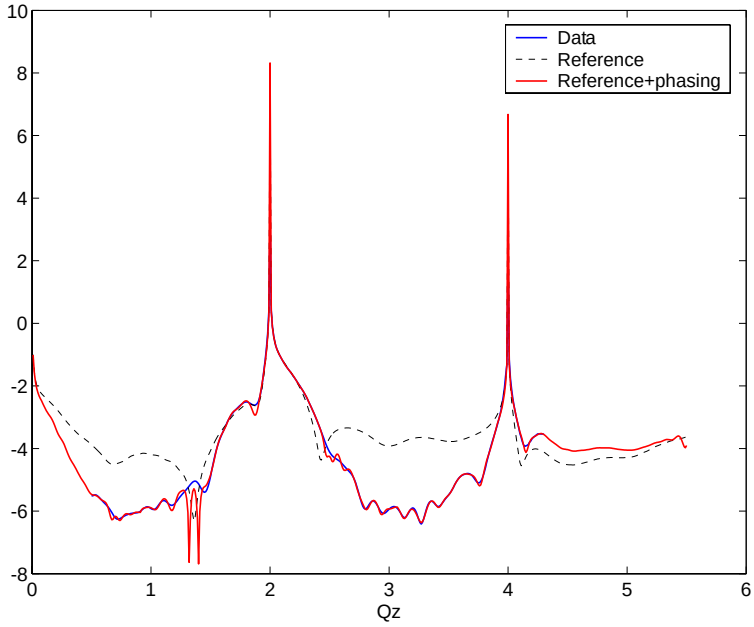

Figure 3.42: Rod 22L of GaSb film on InAs, sample p768

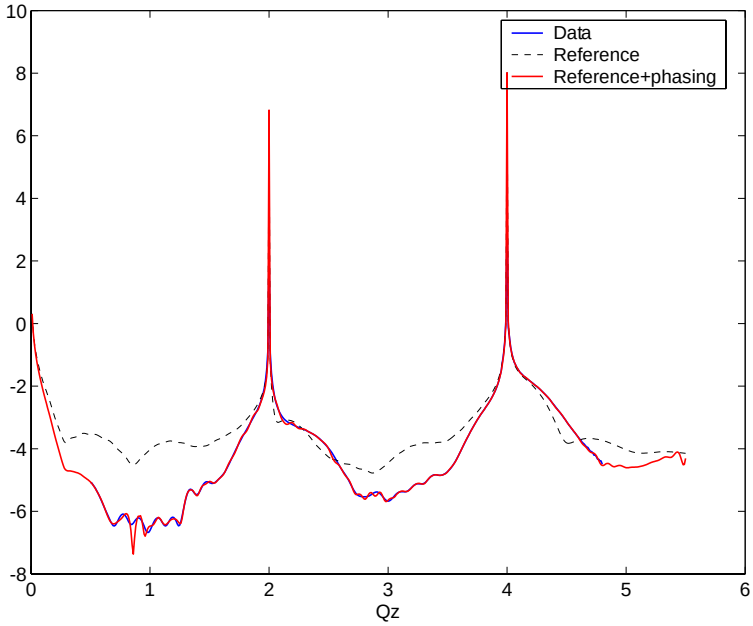

Figure 3.43: Rod 31L of GaSb film on InAs, sample p768

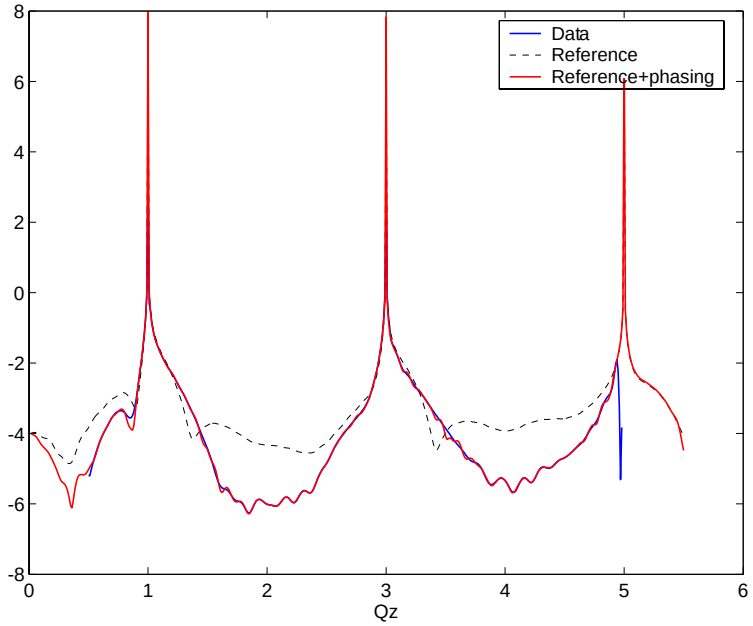

Figure 3.44: Rod 33L of GaSb film on InAs, sample p768

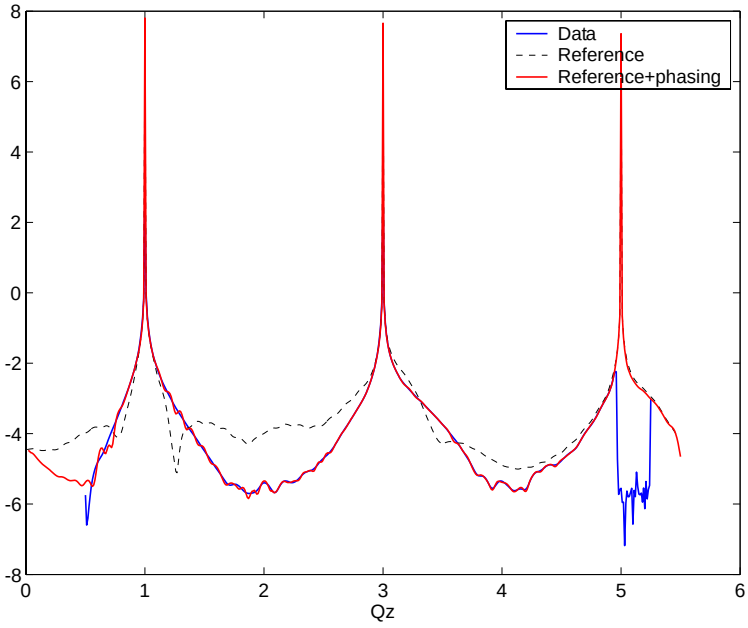

Figure 3.45: Rod 40L of GaSb film on InAs, sample p768

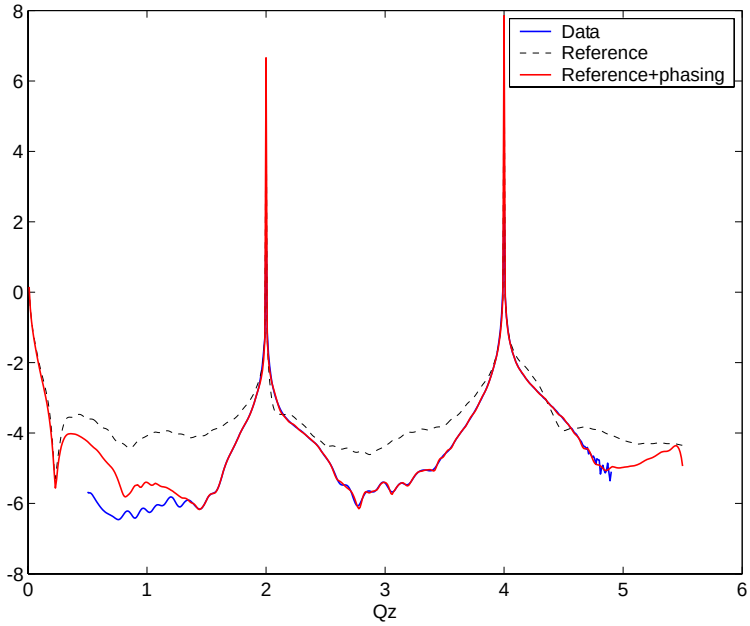

Figure 3.46: Rod 42L of GaSb film on InAs, sample p768

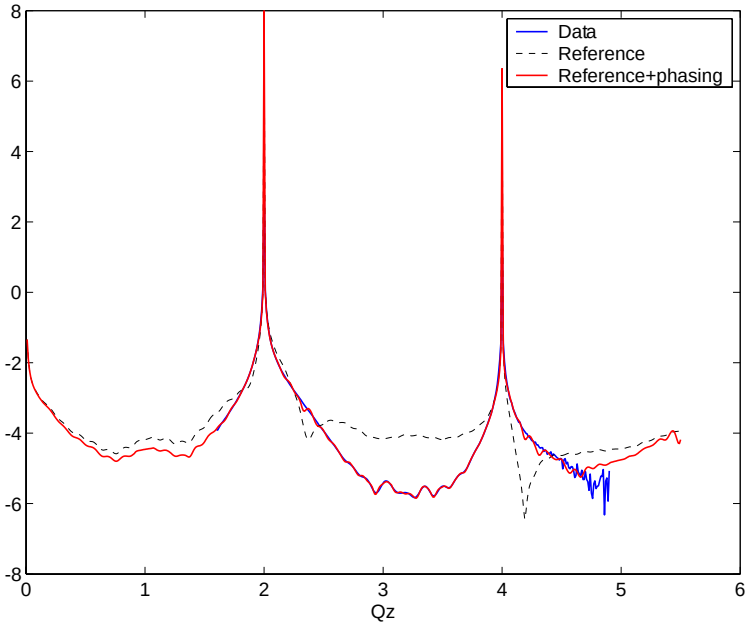

3.12.4 GaSb Film, Sample *s814*

For all the rods other than 00L the $\langle 001 \rangle$ axis was set along a fixed axis given by [0.0505, -0.9975, -0.0502], meaning a fixed value of 3.5° for the angle between the incident beam and the sample (100) planes. For rod 00L, sample $\langle 010 \rangle$ axis was oriented, again, along the fixed axis [0.7071, 0, 0.7071].

Figure 3.47: Rod 00L of GaSb film on InAs, sample s814

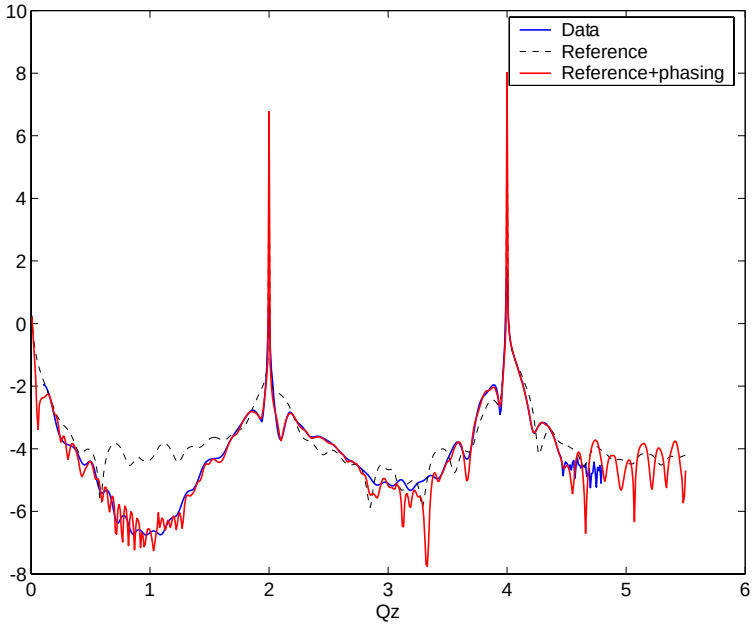

Figure 3.48: Rod 11L of GaSb film on InAs, sample s814

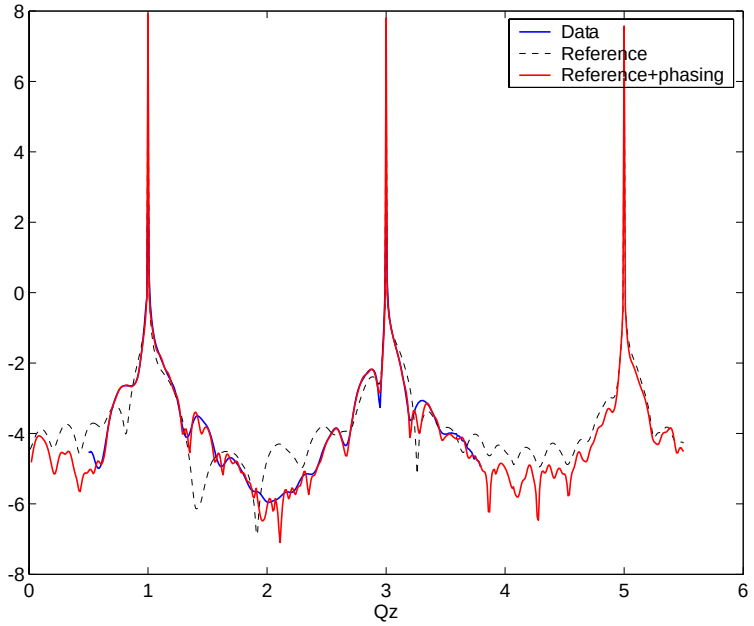

Figure 3.49: Rod $20L$ of GaSb film on InAs, sample s814

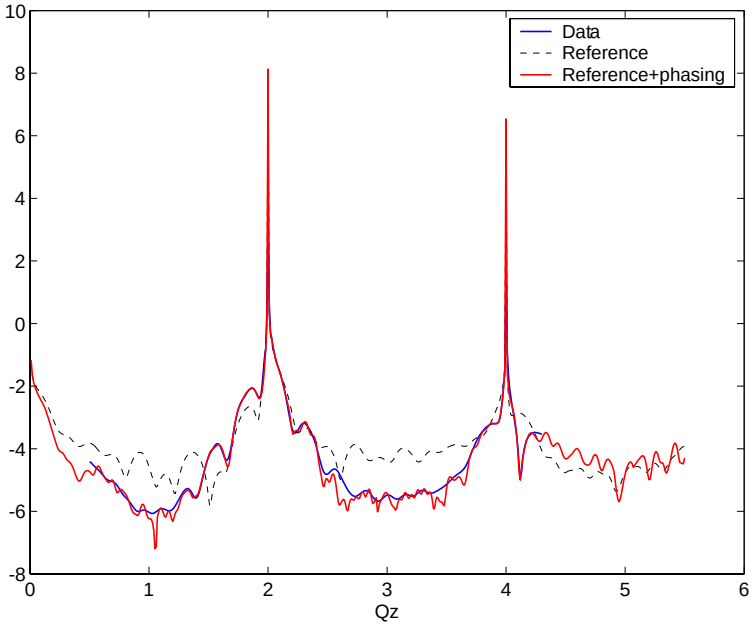

Figure 3.50: Rod $22L$ of GaSb film on InAs, sample s814

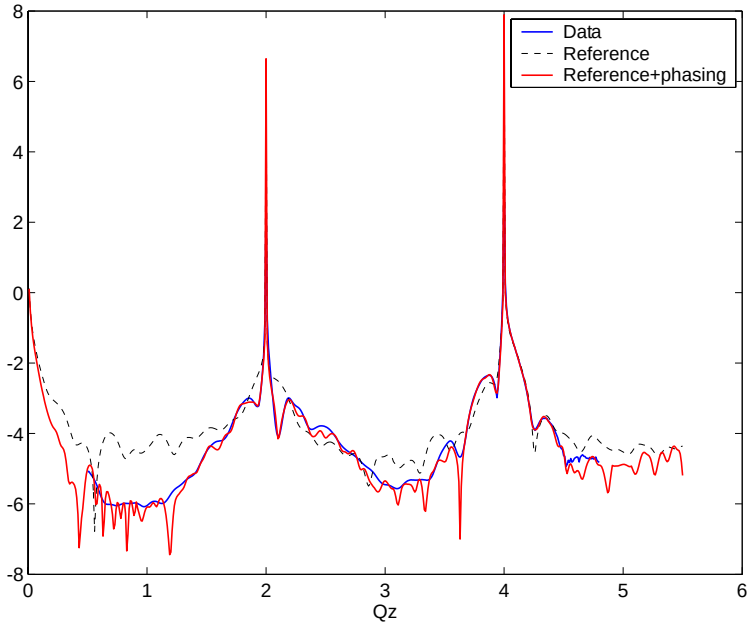

Figure 3.51: Rod 31L of GaSb film on InAs, sample s814

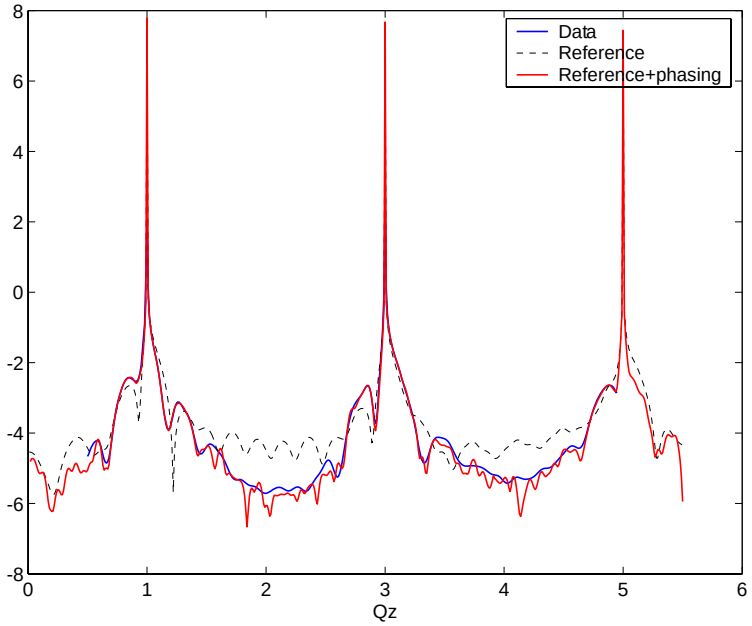

Figure 3.52: Rod 33L of GaSb film on InAs, sample s814

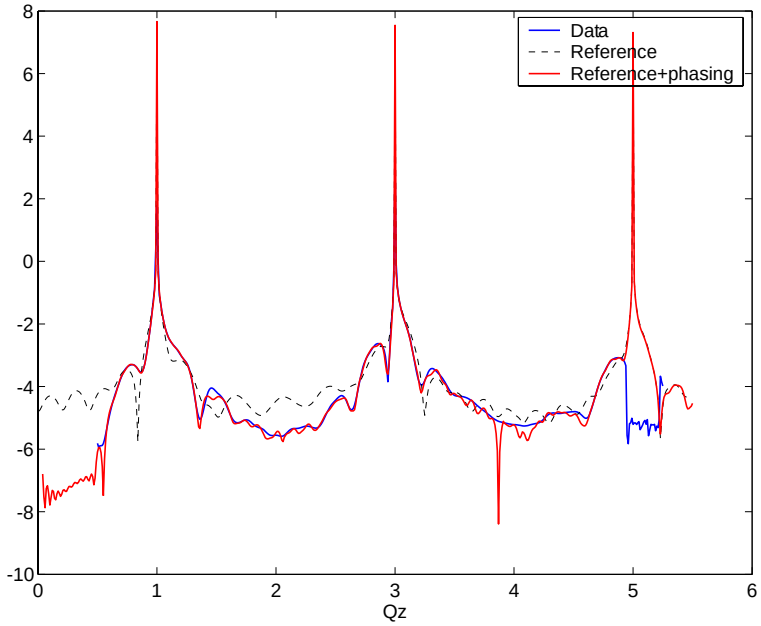

Figure 3.53: Rod 40L of GaSb film on InAs, sample s814

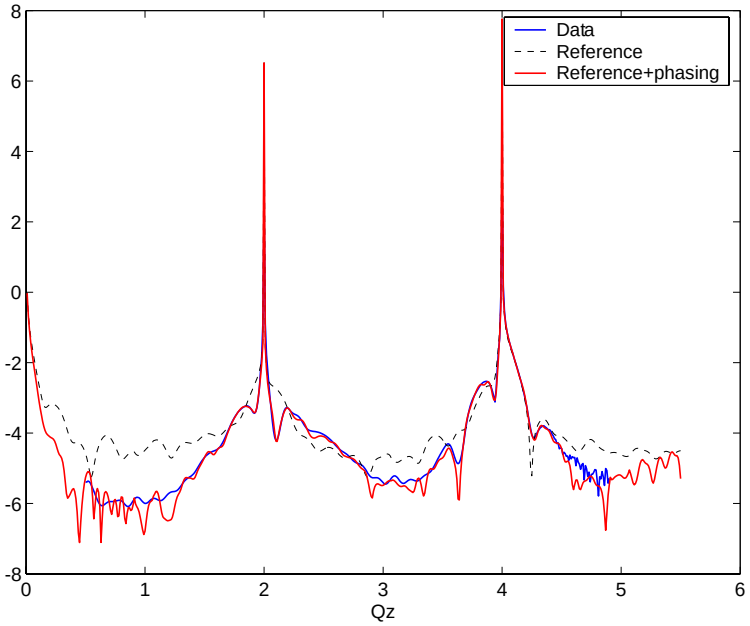

Figure 3.54: Rod 42L of GaSb film on InAs, sample s814

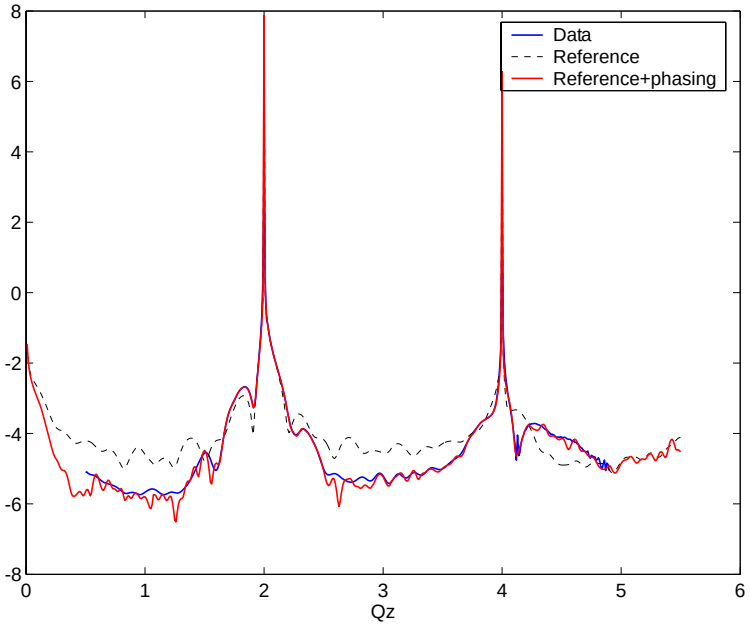

Figure 3.55: Rod 44L of GaSb film on InAs, sample s814

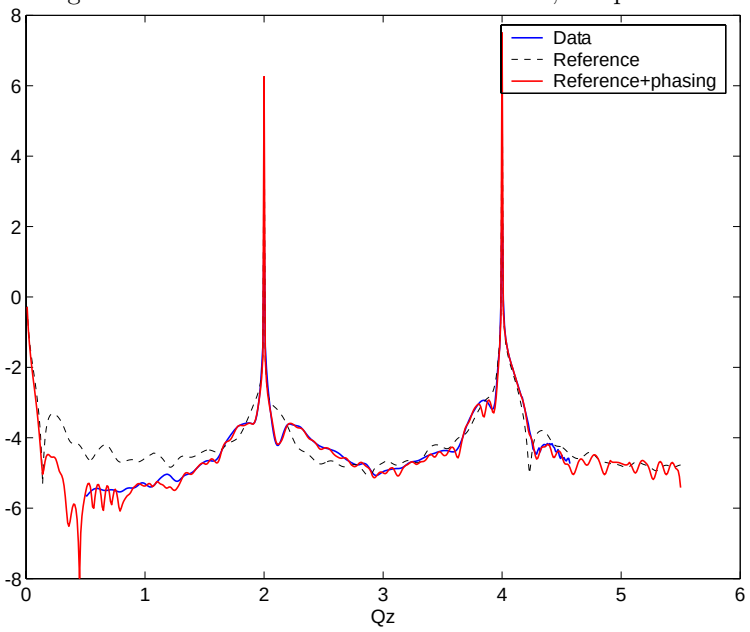

CHAPTER IV

The Morphological Influence of the Electrode Layer on the $PbTiO_3$-$SrTiO_3$ Interface

4.1 Motivation of the Study

Ferroelectricity was discovered in 1921 in Rochelle salt (potassium sodium tartrate), originally produced in France in 1665 and present since in every pharmacy. Ferroelectricity originates from relative shifts of the anion sublattice with respect to the cation sublattice, generating a net dipole moment along a direction that can be correlated with that of the displacement. If an external field is applied, the direction of the polarization can be switched. Ferroelectrics are, in general, polar materials. Their piezoelectricity can be used in sensor/actuator type applications; their pyroelectricity property can be employed in infrared detectors. And it was obvious to many engineers that the capacity to store 2 different polarization states could be used as an encoding basis for the booleans 1 and 0 that form the basis of the memory and the circuitry of today's computers.

It took almost a century for the ferroelectric materials to advance from mild purgative to high tech device, and the path was not always smooth. In the early seventies (1972), a group within IBM wrongfully claimed–intentionally or not–that ferroelectric films will be unstable below a critical thickness [61] and that prevented ferroelectrics from being considered by the civilian industry as serious candidates

for memory applications. Of course, this did not discourage at all the military from using ferroelectric memories on its fighters during the eighties [62].The bonus was that they were resistant to radiation damage. The breakthrough was due, mainly, to the development of new materials like PZT (lead zirconate titanate), a solid solution of ferroelectric $PbTiO_3$ and antiferroelectric $PbZrO_3$ described by $Pb(Zr_xTi_{1-x})O_3$. Its applications include the following: cantilever actuators, probes for atomic force microscopy, micropumps, ultrasonic transducers for medical imaging and linear actuators [63].

The subject of this investigation is $PbTiO_3$ thin films deposited on $SrTiO_3$ $\langle 001 \rangle$ substrates, the pure ferroelectric limit of PZT. Aside from the potential for practical applications, the reasons for choosing this system are the large spontaneous polarization and, most important, the fact that $PbTiO_3$ grows coherently with this substrate.

Given the wide range of applications for this material, significant experimental [64, 65, 66, 67, 68, 69, 70, 36, 71] and theoretical [72, 73] work has been done to characterize its properties. The polarization is closely related to atomic displacements in the unit cell. Since these are, usually, asymmetric with respect to the unit cell, it is in general difficult to use conventional x-ray diffraction to study them due to the center of symmetry introduced by Friedel's law. Thus, it becomes difficult to distinguish between up and down displacements. Although conventional diffraction can be used to investigate assemblies like stripe domains [68, 69], alternative techniques have to be used to characterize properly the atomic displacements, like x-ray standing waves [66], Bragg rod diffraction [70] or phase resolved COBRA [36].

The properties of the thin films differ, in general, from the those of the bulk materials and, as devices get smaller, the relative importance of the interface in-

creases. One of the issues of debate is whether the ferroelectric state is stable below a certain thickness. In the case of ferroelectrics, in the vicinity of the interface with the substrate, at room temperature, the film was found to be in monodomain state [36, 70, 71] whereas at higher temperature, 180° stripe domains form to reduce the free energy [71, 69, 36].

The presence of the interface can induce stress–related [74] and electrostatic [73, 75] effects on the polarization of the ferroelectric film. The interface can also control the orientation of the film, allowing the tailoring of its properties [76].

The purpose of this study is to investigate the structural changes induced by an additional electrode layer on top of a coherent film. Since the layer is conductive, it will alter the ferroelectric film both electrically and mechanically.

Figure 4.1: Diagram of the Ti and the O octahedron cage

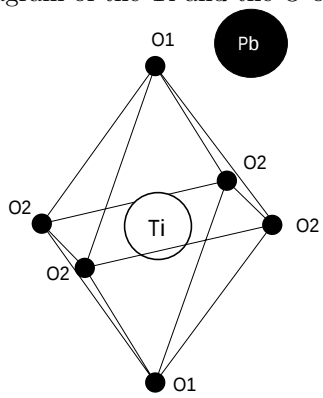

4.2 The Bragg Rods of the Perovskite System

The atomic positions in the unit cell for the perovskite structures to be investigated are as follows (fractions of unit cell): Ti atom at $(0, 0, 0)$, O atoms at $(\frac{1}{2}, 0, 0)$, $(0, \frac{1}{2}, 0)$,$(0, 0, \frac{1}{2})$ and Sr/Pb atom at $(\frac{1}{2}, \frac{1}{2}, \frac{1}{2})$. The oxygen atoms situated on the same vertical line as Ti atoms will be referred to as O1 and the oxygen atoms in the same horizontal plane with the Ti atoms will be referred to as O2.

The Equation 2.9 can we rewritten for this particular unit cell and the particular expression for the structure factor becomes:

$$\mathcal{F}(Q_x,Q_y,Q_z)=\int_V d^3r\sum_{j_x,j_y=-\infty}^{+\infty}\sum_{j_z=1}^{N_{uc}}[f_{1j_z}(\vec{r}\cdot\vec{e}_z)+ \\ +f_{2j_z}(\vec{r}\cdot\vec{e}_z)\cdot e^{2\pi i\frac{1}{2}Q_x}+f_{3j_z}(\vec{r}\cdot\vec{e}_z)\cdot e^{2\pi i\frac{1}{2}Q_y}+ \\ +f_{4j_z}(\vec{r}\cdot\vec{e}_z)\cdot e^{2\pi i\frac{1}{2}Q_z}+f_{5j_z}(\vec{r}\cdot\vec{e}_z)\cdot e^{2\pi i(\frac{1}{2}Q_x+\frac{1}{2}Q_y+\frac{1}{2}Q_z)}]\cdot \\ \cdot e^{\frac{-(2\pi DW_{factor}|\vec{Q}|)^2}{2}} \quad (4.1)$$

Throughout all the next sections, the Bragg rods will be referred to as hkL, with the new indices given by:

$$Q_x=h;\ Q_y=k;\ Q_z=L, \qquad \text{where} \quad h,\,k\in\mathbf{Z}, \quad L\in\mathbf{R} \tag{4.2}$$

The Bragg peaks of the perovskite structure will be situated at integer values of the h,k,L indices and Bragg rods will have significant features along all rods.

As far as symmetry is concerned, Eq. 4.1 states that the surface preserves the four fold symmetry of the bulk. The symmetry equivalence works as described in Eq.4.3.

$$hkL\equiv khL\equiv\overline{h}kL\equiv h\overline{k}L\equiv\overline{h}\,\overline{k}L\equiv\overline{k}hL\equiv k\overline{h}L\equiv\overline{k}\,\overline{h}L \tag{4.3}$$

The symmetry equivalence for the rods with indices in the interval $[-3,3]$ is showed in Fig.4.2. To be able to completely describe a reciprocal lattice volume consisting of rods with indices in $[-3,3]$, based on the symmetry equivalence given by the Eq.4.3 and Figure 4.2, 10 rods need to measured, namely $00L$, $10L$, $11L$, $20L$, $21L$, $22L$, $30L$, $31L$, $32L$ and $33L$.

4.3 The Experiment

For this experiment, a six circle Kappa-Newport goniometer [77] was used. All measurements were made at room temperature. The value of ψ was set to $-44.285°$

and was not changed throughout the duration of the experiment. The distance between the detector and the center of the goniometer was ~ 0.93 m.

4.3.1 Energy Setting

The energy setting followed, in general, the same considerations as described in Section 3.3.2. Table 4.1 lists the binding energies for different atomic shells present in the sample to be investigated. In order to avoid fluorescence, a reasonable value

Table 4.1: Binding energy for the atomic species present in the sample (eV)

Element	Z	$K1s$	$L_1 2s$	$L_2 2p_{1/2}$	$L_3 2p_{3/2}$
O	8	543.1			
Ti	22	4,966			
Sr	38	16,105	2,216	2,007	1,940
Pb	82	88,005	15,861	15,200	13,035

of the energy was be below the value of L_3 shell of Pb. Since the symmetry of the systems allowed for Bragg points at every integer value of L, the requirement to maximize the radius of the Ewald sphere was not as stringent as in the case of the

Figure 4.2: Symmetry equivalence for the Bragg rods of perovskite structure

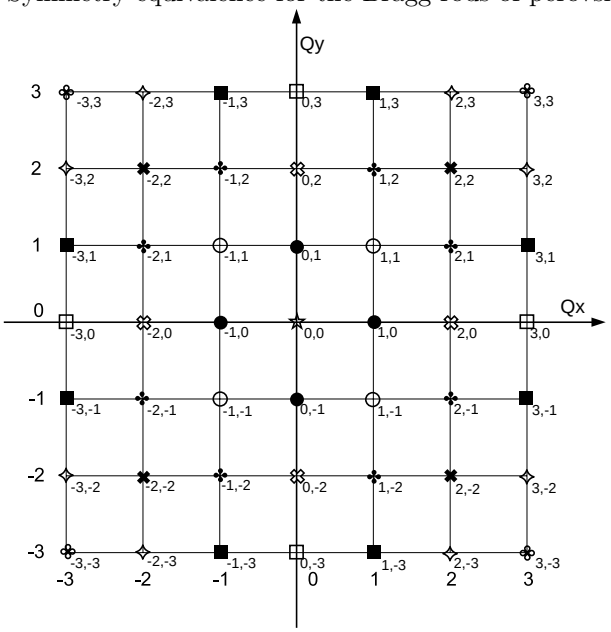

zinc–blende. Similar to the value chosen in previous experiments carried out on this system, the energy of choice was 11.4 keV.

To get this value, the undulator gap was set at 24.674 mm corresponding to an energy setting of 11.45 keV. To calibrate the monochromator, the transmission of a thin Ge foil was recorded as the energy was scanned around the value 11.4 keV. A feature at 11.1064 keV in the absorption spectrum was used as reference to correct the setting of the monochromator.

4.3.2 Filters

As already discussed in detail Section 3.3.1, the choice of energy dictates the choice of material and thickness of the filters. Figure 3.2 describes the attenuation behavior of a Cu foil 10 μm thick. As in the case of the semiconductors, four Cu attenuator foils were used, with thicknesses of 10, 20, 40 and 80 μm. To calibrate them, the (221) reflection was used following the same procedure as in the case of semiconductors (see, again, Section 3.3.1). The attenuation values for the 16 possible filtration settings obtained with the 4 attenuators are listed in the Table 4.2.

The amount of third harmonic in the beam relative to the first increases when increasing the filtration. The effect is predominant in the region of the Bragg peaks but those regions are excluded from the calculation. Unfortunately, attenuation data corresponding to the energy of 34.20 keV was not available. A rough estimate, though, can be made using the data available for 30.0 keV presented in Table 3.1.

4.3.3 Preparation of the Incident Beam

The monochromated beam was passed through a set of slits confining it horizontally to 400 μm. To confined it vertically, a focusing mirror was used. The height of the resulting beam was reduced to 50 μm.

Table 4.2: The attenuation values for the Cu filters at 11.4 keV

Filter #	Foils	Transmission at $11.4keV$
0	none	1
1	I	$2.7557 \cdot 10^{-1}$
2	II	$7.4906 \cdot 10^{-2}$
3	$I + II$	$2.0691 \cdot 10^{-2}$
4	III	$5.7806 \cdot 10^{-3}$
5	$I + III$	$1.6114 \cdot 10^{-3}$
6	$II + III$	$4.3320 \cdot 10^{-4}$
7	$I + II + III$	$1.1976 \cdot 10^{-4}$
8	IV	$3.9154 \cdot 10^{-5}$
9	$I + IV$	$1.0985 \cdot 10^{-5}$
10	$II + IV$	$5.3215 \cdot 10^{-6}$
11	$I + II + IV$	$1.4664 \cdot 10^{-6}$
12	$III + IV$	$4.0411 \cdot 10^{-7}$
13	$I + III + IV$	$1.1136 \cdot 10^{-7}$
14	$II + III + IV$	$3.0688 \cdot 10^{-8}$
15	$I + II + III + IV$	$8.4566 \cdot 10^{-9}$

Figure 4.3: Calculated mirror reflectivity at E=11.40 keV

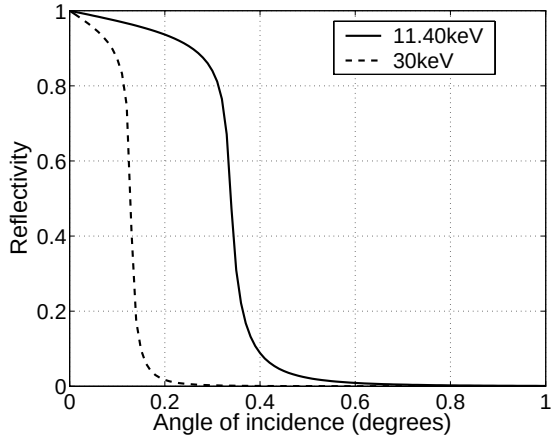

The critical angle of the Rh mirror varies with the energy. Lack of data availability beyond 30 keV only allowed a reflectivity comparison in Fig.4.3 between 11.4 keV and 30 keV–used to estimate the behavior of the third harmonic.

4.3.4 Sample Alignment

After bouncing off the K–B mirror, the incident beam vector was [-4.0831, 0.0147, 4.0799] $Å^{-1}$. To align the sample, first the (200) and (13-1) reflections were found. They were used to calculate the first orientation matrix which helped finding the following reflections: (131), (111), (120), (103), (131), (131) rotated 10° about the incident beam vector and (221). With these reflections the orientation matrix was optimized.

To precisely determine its height, the sample was set perpendicular to the optical axis of the camera. Next, using the lateral translation stage of the sample, the center of pad was overlapped with the monitor marking corresponding to the center of the goniometer. Next, a Pt (111) reflection was located in symmetric configuration setting $\theta = 5°$, $\chi = -90°$, $\nu = -45°$ and scanning 2θ until the peak was identified. With this geometry and the x-ray beam on, the sample height was scanned until different region of the sample got into the beam. If we imagine a section through the sample using the plane determined by the vertical and the incident beam and correlate it with the result of the scan we can very accurately determine the height of the sample.

4.4 The $PbTiO_3$-$SrTiO_3$ Sample

The sample was grown epitaxially by sputtering on a conductive $SrTiO_3$ $\langle 001 \rangle$ substrate ($a_{PbTiO_3} = 3.905$ Å) with a miscut smaller than 0.15°. The ferroelectric samples were all grown in the laboratory of Prof. Chang–Beom Eom at the University

of Wisconsin. The substrate was Nb doped. 500 Å insulating $SrTiO_3$ was sputtered first. On top of the homoepitaxial layer, 50 Å of $PbTiO_3$ was deposited. The films remained coherently strained with the substrate, as shown by the Bragg rods. Circular Pt contact pads as thick as $\sim$ 150 nm with a diameter of 1 mm were deposited on top using a shadow mask. The Pt electrode was polycrystalline.

Figure 4.4: $PbTiO_3$ sample structure

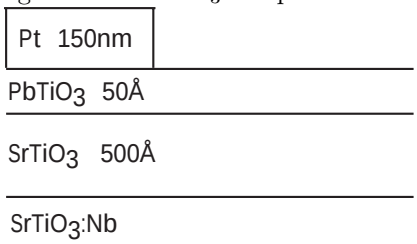

4.5 The $PbTiO_3$ Film with the Electrode

4.5.1 The Data Acquisition

To position the contact pad at the center of the goniometer we aligned the sample perpendicular on the optical axis of the telescope. Using the sample lateral translation motors we brought the chosen pad in the spot marked on the monitor as the center of the goniometer (see Section 2.5.4).

On the electrode region, four Bragg rods were measured and they are listed in Table 4.3 along with the L limits. The integration time had different values for every rod and they are listed in the same table.

Table 4.3: Rods measured for the electrode region and the corresponding L intervals (in reciprocal space units)

Rod index	L_{start}	L_{end}	Int. Time(s)
$10L$	0.5	2.75	5.0
$11L$	0.5	3.10	4.5
$20L$	0.5	3.40	4.5
$21L$	0.5	3.40	4.5

Figure 4.5: Rod 10L of $PbTiO_3$–$SrTiO_3$ with electrode layer on top

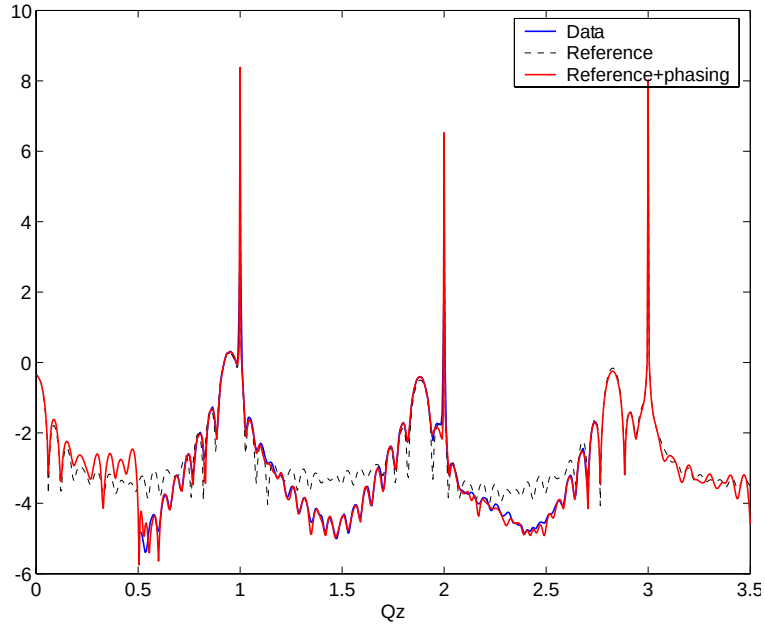

Figure 4.6: Rod 11L of $PbTiO_3$–$SrTiO_3$ with electrode layer on top

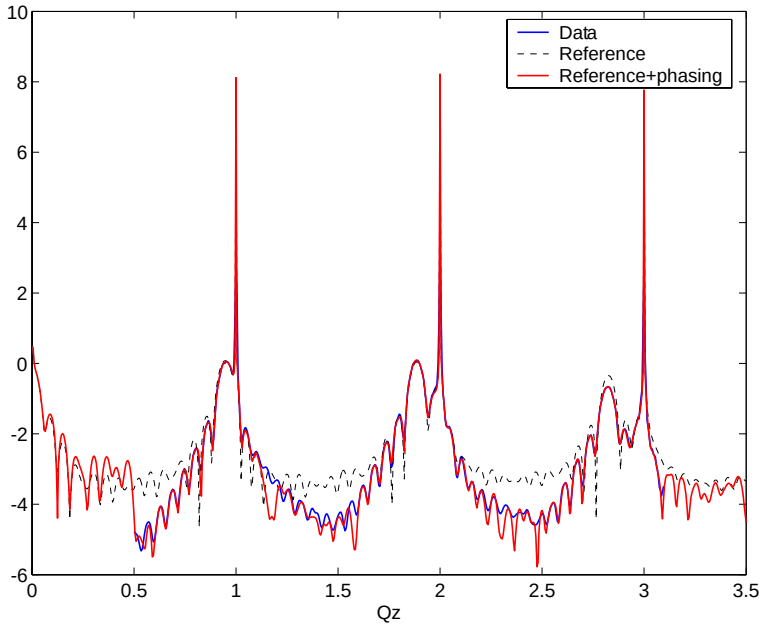

Figure 4.7: Rod 20L of $PbTiO_3$–$SrTiO_3$ with electrode layer on top

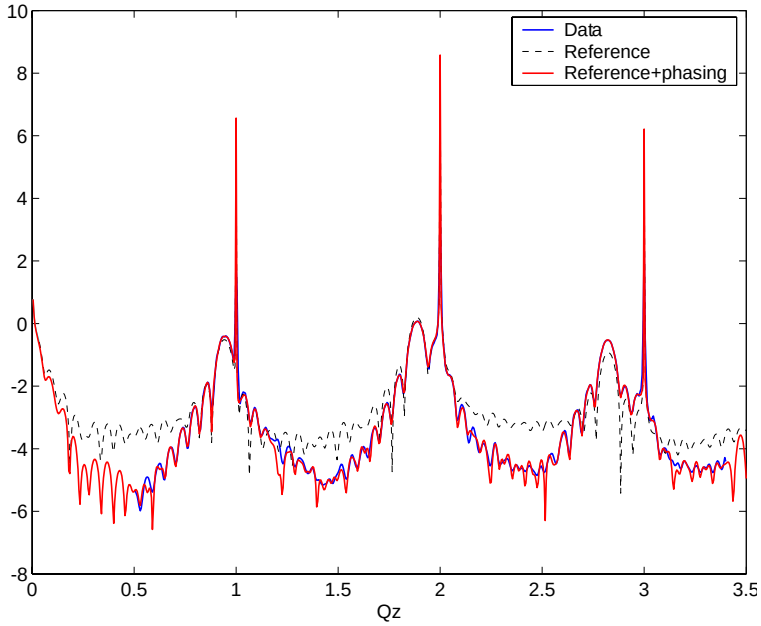

Figure 4.8: Rod 21L of $PbTiO_3$–$SrTiO_3$ with electrode layer on top

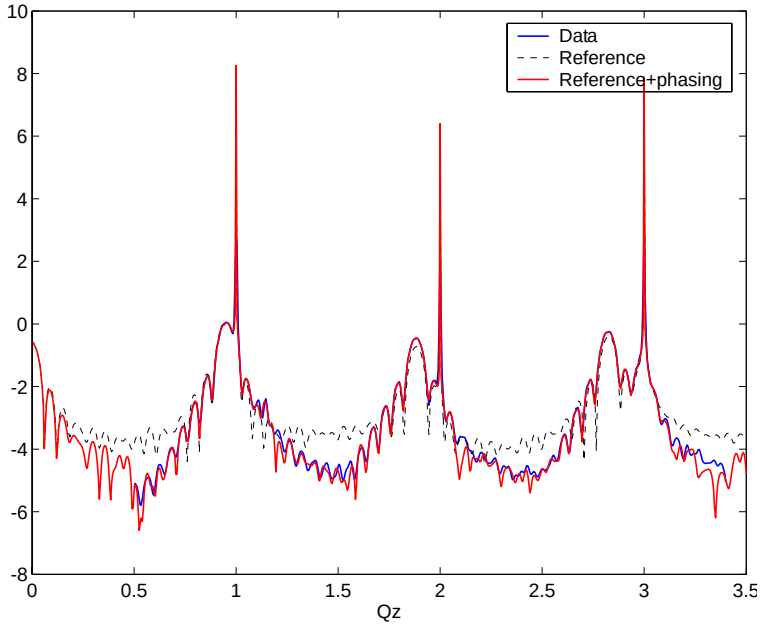

Table 4.4: Parameters used to generate the reference for the electrode region, before and after the fit

	UC dist.	Mult. factor factor	in plane DW bulk subs.	vertical DW bulk subs.	DW film	DW explicit subs.	interf. gauss. position	interf. gauss. width
units		RLU^{-1}	RLU^{-1}	RLU^{-1}	RLU^{-1}	UC	UC	
initial	1.050	9.50×10^{-4}	0.0500	0.0500	0.0500	0.0500	3.00	3.00
fit	1.062	1.04×10^{-3}	0.0508	0.0424	0.0496	0.0580	3.00	2.76

Again, the sample $\langle 001 \rangle$ axis was oriented along a fixed axis, given by [0.0505 -0.9974 -0.0505]. This corresponded to a fixed angle of incidence of 4.2°. A density of 200 points for every reciprocal space unit cell was used.

4.5.2 Data Analysis

First step of the analysis is to generate the reference (see Section 2.2.1). The model must take into account all the data available about the sample, presented in Section 4.4. The nominal thickness of $PbTiO_3$ sample was 50 Å. One of the issues that had to be addressed was the true film thickness. The samples were grown by sputtering and the thickness control was not nearly as good as in the case of the MBE growth. The fit was performed for different values of the sample thickness. The value of the thickness that generated the best reference was 17 unit cells. 1200 iterations were performed to determine the best reference and the fit parameters are listed in Table 4.4.

With the optimized parameters the reference was generated and then passed along to the phasing procedure. For the phasing procedure the data was resampled with a density of 100 points/rec.space.unit cell. The complex structure factor was fed into the phasing routine as the new reference. Three iterations were performed to obtain the final result.

Figures 4.5–4.8 present the experimental data, the initial reference and the fit

Figure 4.9: 2d electron distribution map of horizontal Ti-O2 plane in $PbTiO_3$–$SrTiO_3$ with electrode layer on top

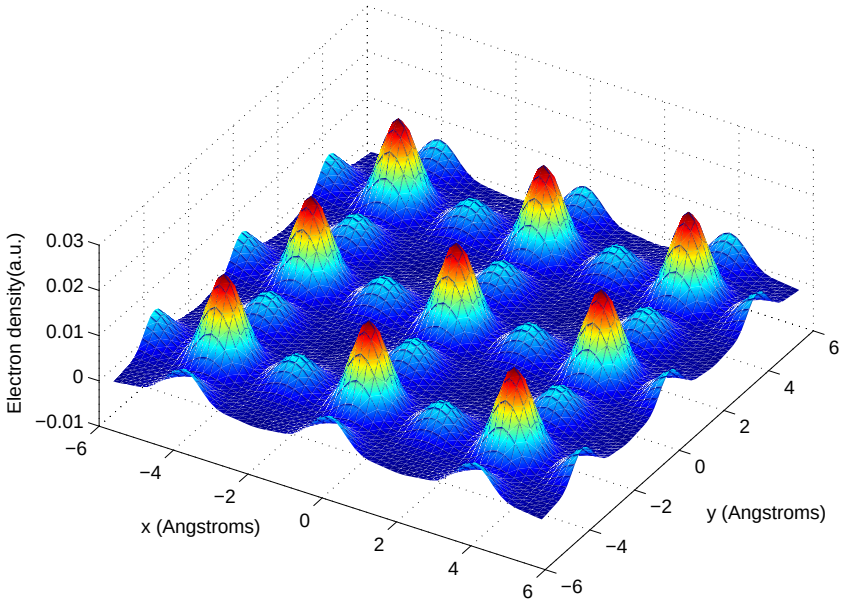

Figure 4.10: Position of the Pt (222) reflection as measured on the 11L rod

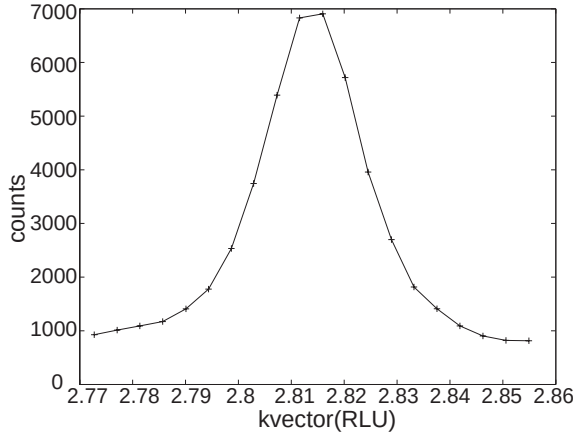

after 3 iterations. Figure 4.9 represents an in–plane profile through the 3D electron density (ED). The plane, parallel to the sample surface, contains the Ti and O2 atoms. Figure 4.11(a) displays the total ED along the vertical direction. Figure 4.11(b) represents the ED vertical profile along the Ti–O1 line, Fig.4.11(c) represents the profile along O2–O2 line and Fig.4.11(d)–along the Sr(Pb)–Sr(Pb) line. Figure 4.12 represents the width of the ED peaks and Figure 4.13–the integrated values of these peaks. Figure 4.14 shows the vertical spacing between equivalent atoms in two consecutive unit cells. In order to display the atomic positions in an intuitive manner, in Figure 4.15 are plotted the out-of-plane atomic displacements relative to their corresponding positions in an $SrTiO_3$ crystal, as if the substrate would extend into the film region. We will refer to this profile as the substrate relative displacement (SRD).

Since the Pt electrode is polycrystalline, it is expected that the measured rods will intersect its powder diffraction shells. Figure 4.10 shows the corresponding Pt (222) reflection as measured at the intersection with the $11L$ rod. The horizontal axis units represent the total Q position in the reciprocal space, in $PbTiO_3$ reciprocal space units.

The $PbTiO_3$ film was coherent with the substrate. Thus, a borrowed the lattice constant value of $SrTiO_3$. In the vertical direction, the lattice spacing c was 4.13Å.

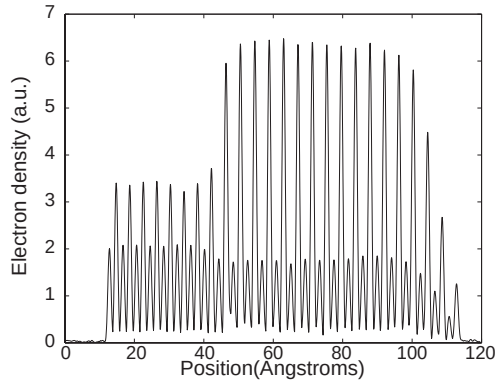

(a) Total electron density

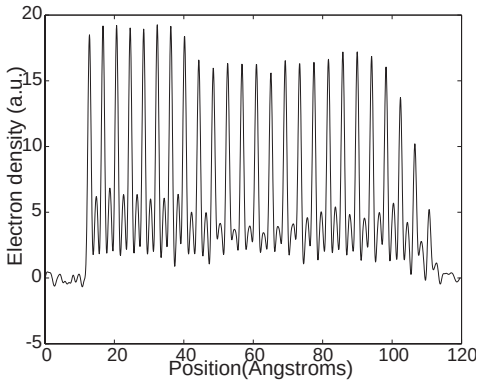

(b) Electron density along Ti–O1 line

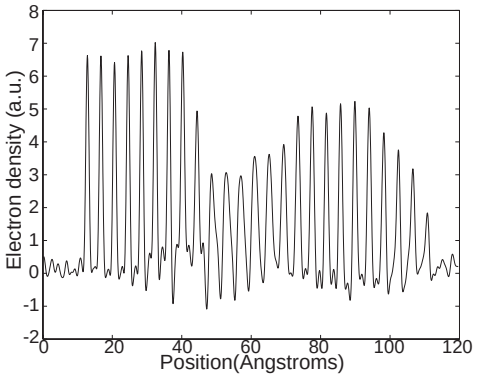

(c) Electron density along O2-O2 line

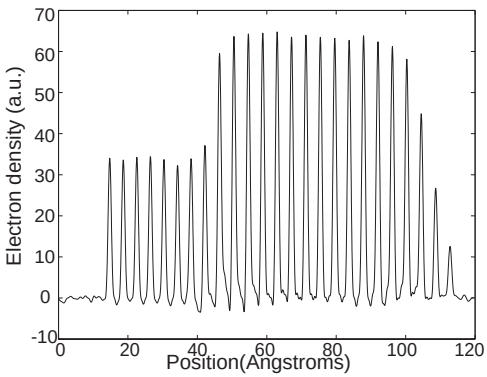

(d) Electron density along Sr(Pb)–Sr(Pb) line

Figure 4.11: Electron density profiles along z in $PbTiO_3$–$SrTiO_3$ sample with Pt electrode

Figure 4.12: The width of the electron density peaks in $PbTiO_3$–$SrTiO_3$ sample with electrode layer on top

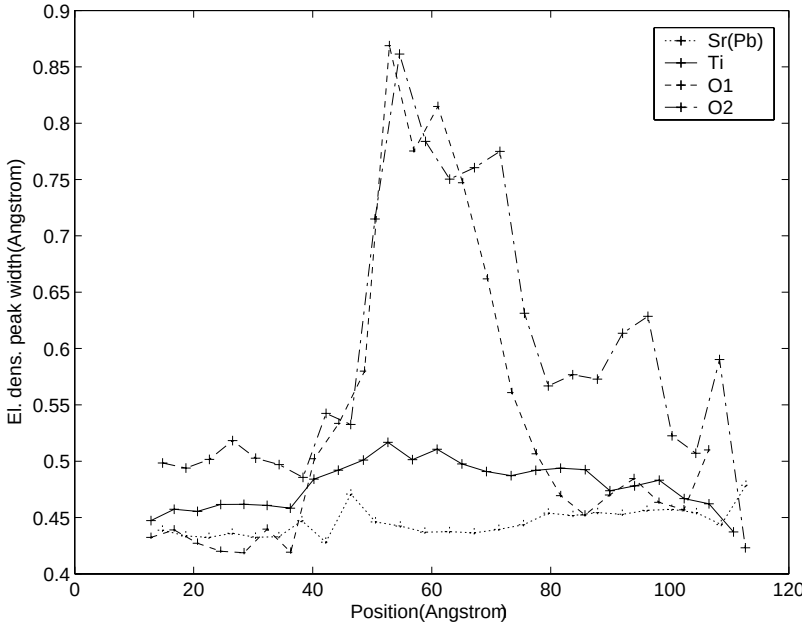

Figure 4.13: Integrated electron density peaks in $PbTiO_3$–$SrTiO_3$ sample with electrode layer on top

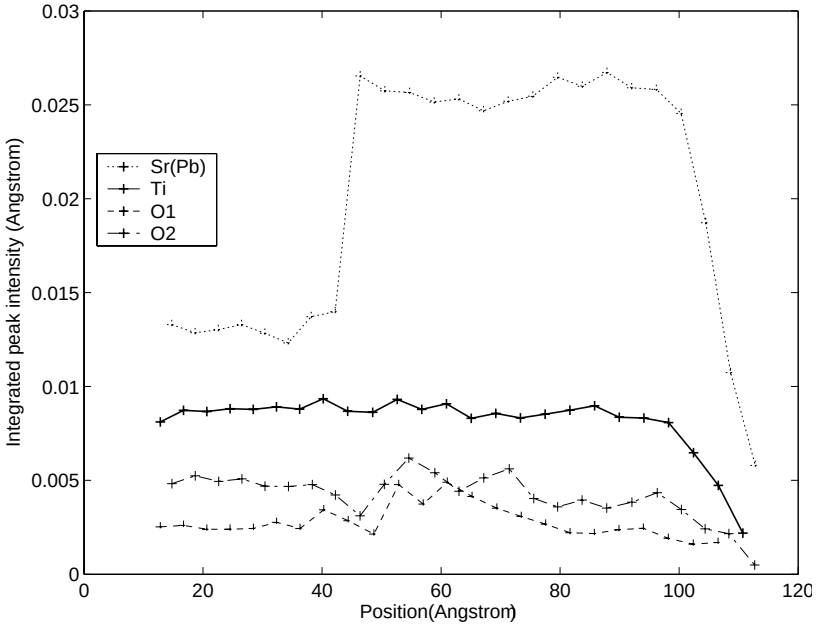

Figure 4.14: Vertical distance between same species atoms in $PbTiO_3$–$SrTiO_3$ sample with electrode layer on top

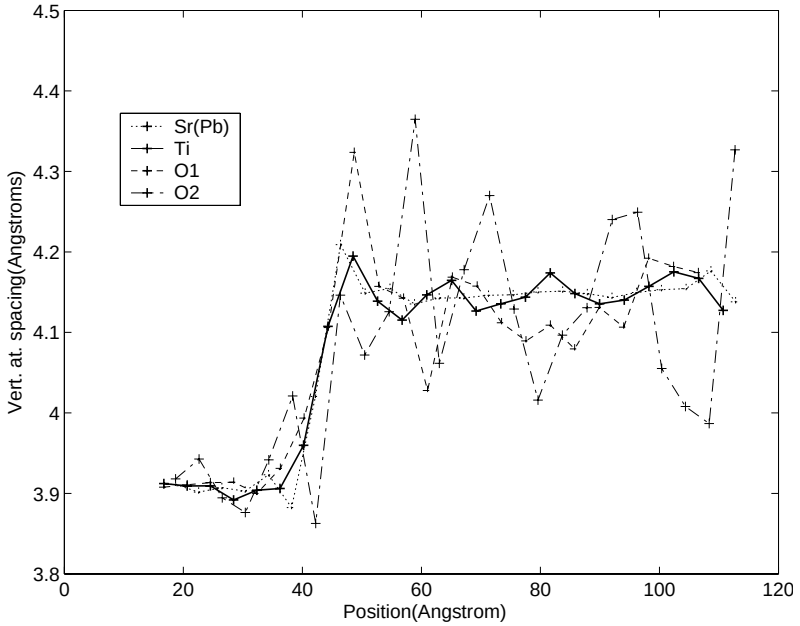

Figure 4.15: Atomic displacement in $PbTiO_3$–$SrTiO_3$ sample with electrode layer on top

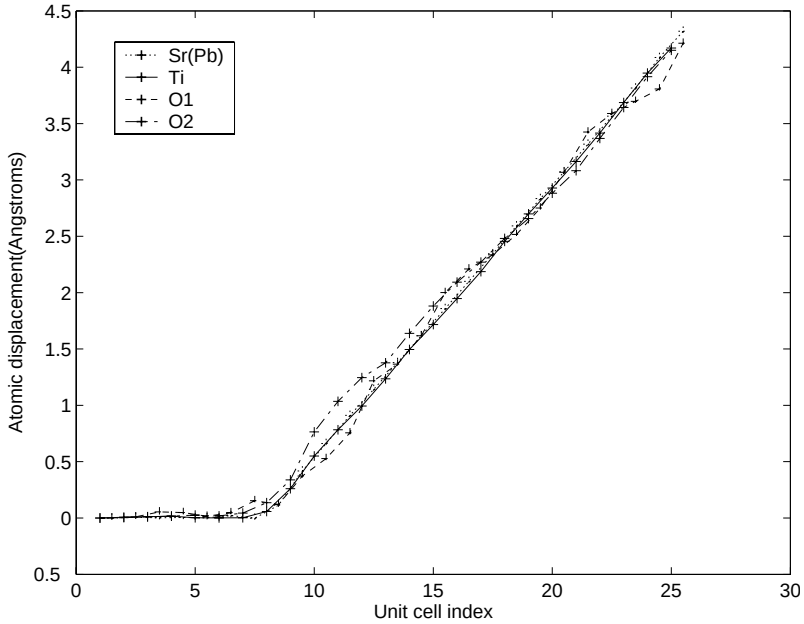

4.6 The Bare $PbTiO_3$ Film

4.6.1 The Data Acquisition

The first step was to set a bare region of the sample in the center of the goniometer. To do that, we brought the sample approximately perpendicular on the optical axis of the telescope. Since the center of the goniometer was marked on the display (see Section 2.5.4), we used the sample horizontal translation stage overlap it with the bare region decided to be scanned.

On the bare region 3 Bragg rods were acquired, listed in Table 4.5 along with the high and low limits for L and the values of the integration times. 200 points were acquired per reciprocal space unit in the rod scans.

Table 4.5: Rods measured for the bare region the corresponding L intervals (in reciprocal space units)

Rod index	L_{start}	L_{end}	Int.time(s)
$10L$	0.5	2.75	4.0
$11L$	0.5	3.10	3.0
$20L$	0.5	3.50	3.5

The sample $\langle 001 \rangle$ axis was oriented along the fixed axis [0.07034 -0.9950 -0.0703], corresponding to a fixed angle of incidence of 5.85°.

4.6.2 Data Analysis

To model the reference we considered the structure of the sample as described in the Section 4.4. As in the case of the electrode area, the thickness of the film was found to be 17 unit cells (66.4 Å). After 1200 iterations, the fit parameters were found to have the values listed in the Table 4.6.

With these values, all rods with indices in the interval $[-3, 3]$ were generated and the result was transfered to the phasing procedure. To use the COBRA approximation, the data and the reference were resampled with a density of 100 points/rec.space.unit

Table 4.6: Parameters used to generate the reference for the bare region, before and after the fit

	UC dist.	Mult. factor factor	in plane DW bulk subs.	vertical DW bulk subs.	DW film	DW explicit subs.	interf. gauss. position	interf. gauss. width
units		RLU^{-1}	RLU^{-1}	RLU^{-1}	RLU^{-1}	UC	UC	
initial	1.060	3.00×10^{-4}	0.0500	0.0500	0.0500	0.0500	2.00	3.00
fit	1.057	1.04×10^{-3}	0.0535	0.0355	0.0514	0.0779	1.51	1.12

cell. The result (reference + phasing) was introduced again in the phasing routine as the new reference and the procedure was repeated 4 times until the final result was achieved.

Figures 4.16–4.18 show the data, the initial reference after 1200 iterations and the final result (phasing + reference). Figure 4.19(a) displays a vertical profile of the total ED. Figures 4.19(b), 4.19(c) and 4.19(d) show vertical ED profiles along Ti–O1, O2–O2 and Sr(Pb)–Sr(Pb) lines, respectively. Figure 4.20 displays the vertical witdh of the ED peaks, Figure 4.21 displays their integrated values, Figure 4.22 displays the vertical spacing between 2 consecutive equivalent atomic positions and Figure 4.23–the SRD.

Due to the film coherence with the substrate, the in-plane lattice parameter of $PbTiO_3$ a was that of the substrate, 3.905 Å. In the vertical direction, using the position of the Pb peaks, the lattice spacing c can be estimated from the Figure 4.19(d) and its value is4.1Å.

4.7 Interpretation of Results

An examination of the ED behavior in planes parallel to the sample surface did not show any atomic displacement both in the film and the substrate. This is expected because the polar (ferroelectric) axis is normal to the planes and therefore ionic displacements are only expected in this direction. Therefore, all the discussion will

Figure 4.16: Rod 10L of bare $PbTiO_3$–$SrTiO_3$

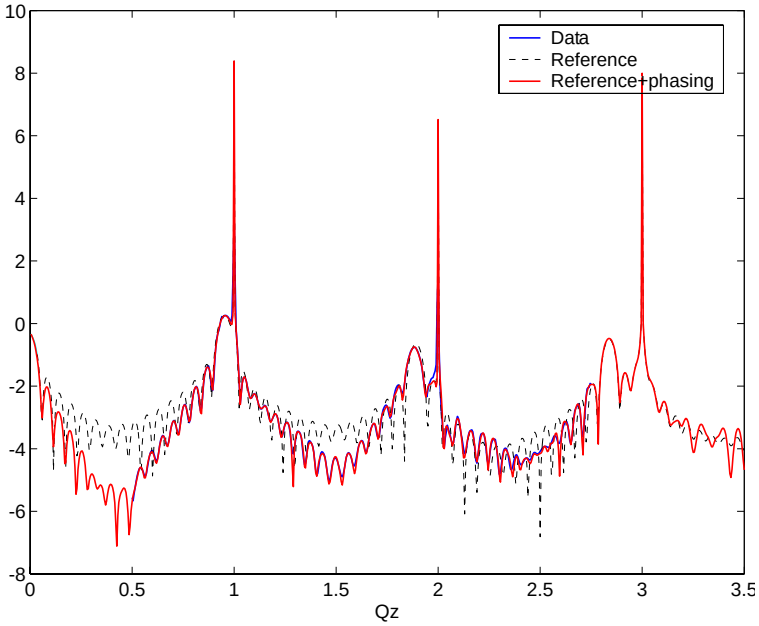

Figure 4.17: Rod 11L of bare $PbTiO_3$–$SrTiO_3$

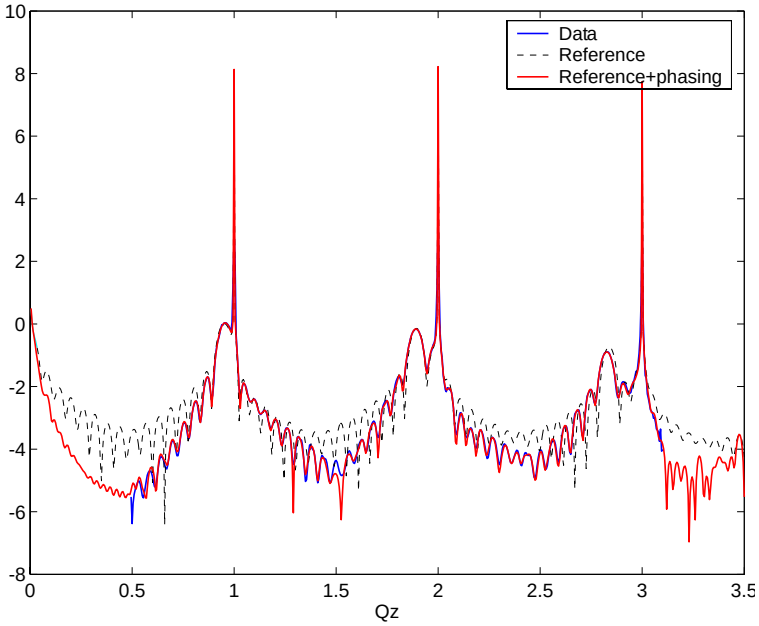

Figure 4.18: Rod $20L$ of bare $PbTiO_3$–$SrTiO_3$

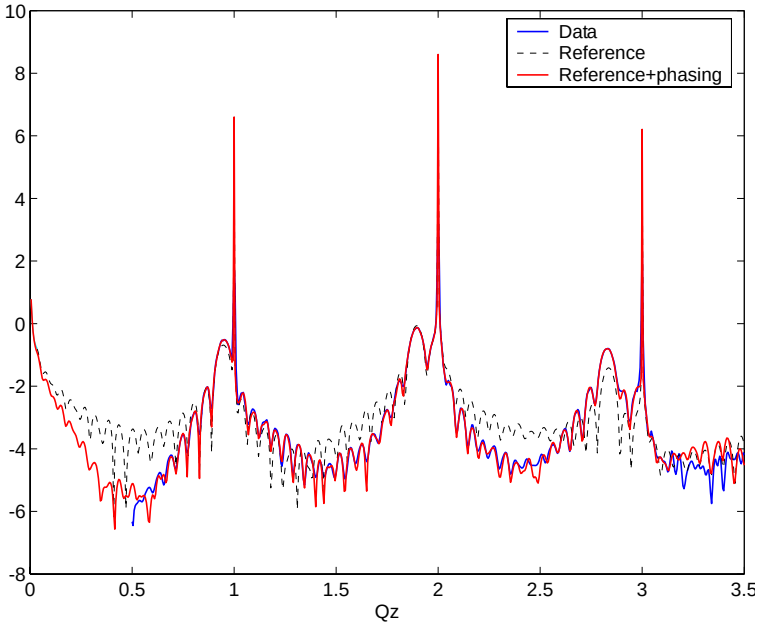

focus on the atomic behavior in the vertical direction.

The film unit cell is tetragonal, as expected, and the lattice spacing values are similar in both case to those of the bulk , $a^{bulk}_{PbTiO_3} = 3.904$ Å and $c^{bulk}_{PbTiO_3} = 4.152$ Å [78]. In addition to that, the measured lattice constant of the Pt electrode $a_{Pt} = 3.925$ Å is very similar to the one of the bulk, 3.924 Å. (It is worth mentioning that the setup was optimized for single crystal diffraction–large detector slits–and that limits the resolution in the case of powder diffraction measurements.)

In the case of the bare region (without the electrode), the O1 sublattice appears to be consistently shifted toward the substrate/film interface for ~ 8 unit cells (Figure 4.24(a)). The distortion does not persist beyond that. In the presence of the electrode, the displacements appear to have a more complicated distribution.

In the regions close to the substrate, data on both bare and Pt electrode seems consistently to indicate that the O2 sublattice is displaced away from the substrate (Figure 4.24(b)), producing a polarization pointing in the opposite direction, toward

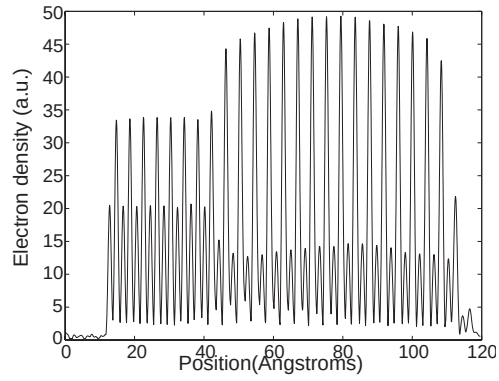

(a) Total electron density

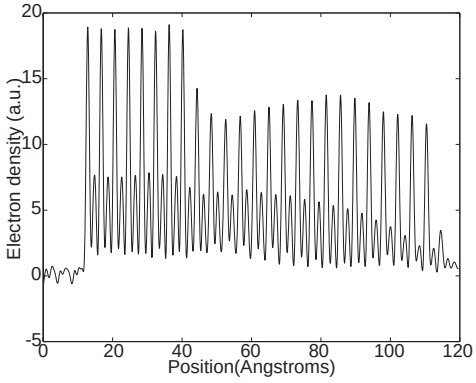

(b) Electron density along Ti–O1 line

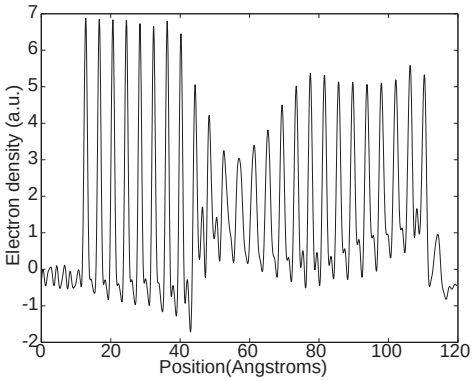

(c) Electron density along O2-O2 line

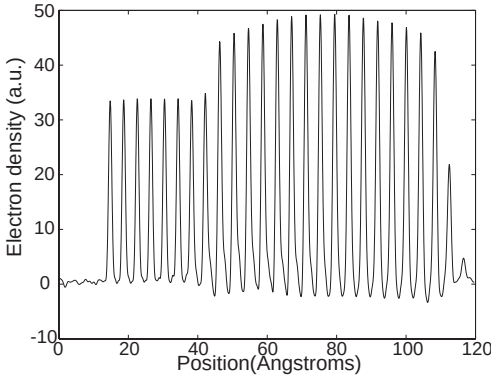

(d) Electron density along Sr(Pb)–Sr(Pb) line

Figure 4.19: Electron density profiles along z in bare $PbTiO_3$–$SrTiO_3$ sample

Figure 4.20: The width of the electron density peaks in bare $PbTiO_3$–$SrTiO_3$

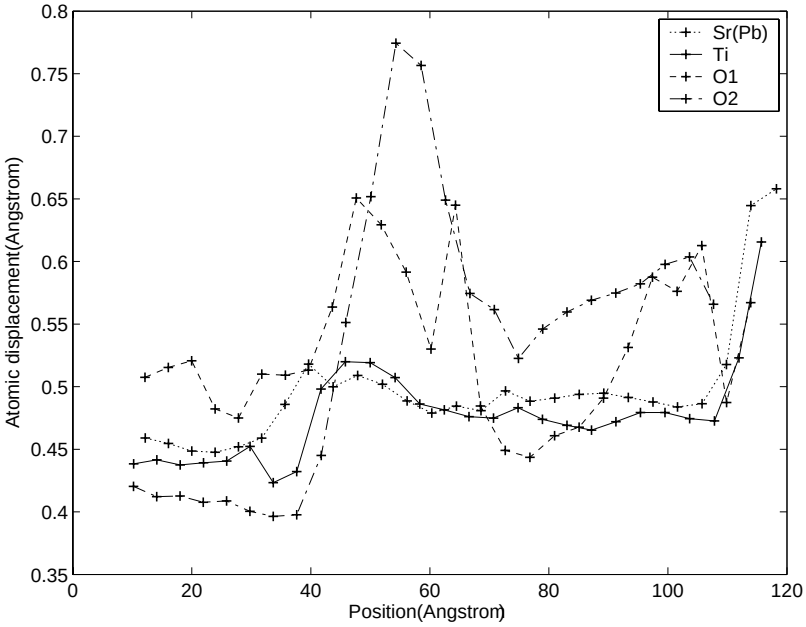

Figure 4.21: Integrated electron density peaks in bare $PbTiO_3$–$SrTiO_3$

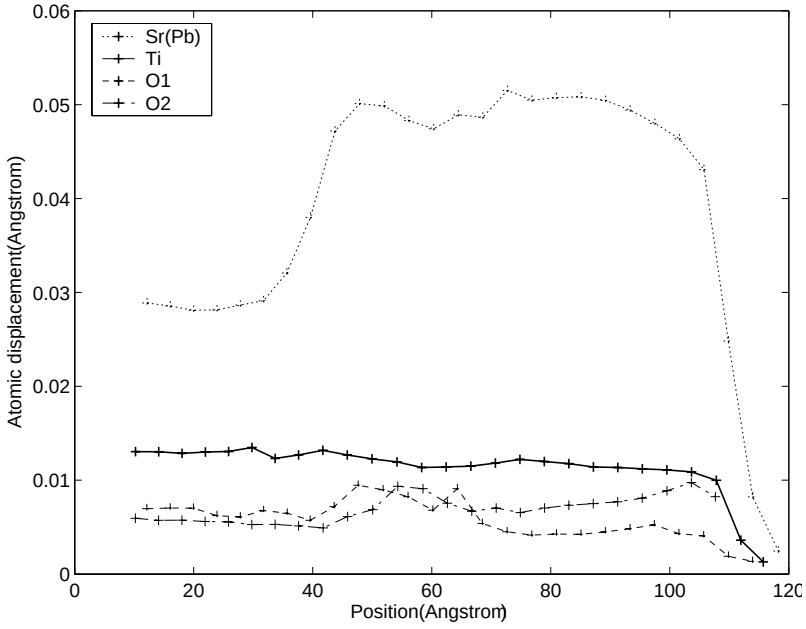

Figure 4.22: Vertical distance between same species atoms in bare $PbTiO_3$–$SrTiO_3$

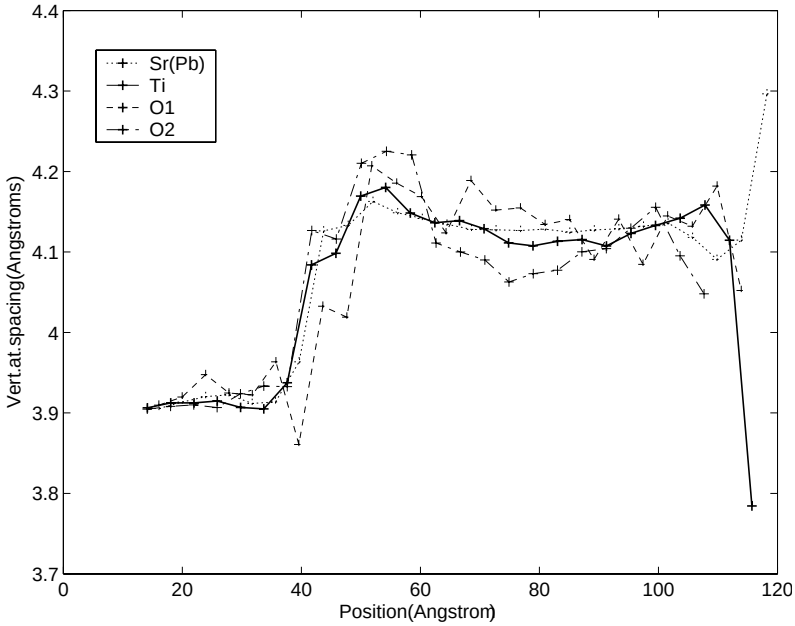

Figure 4.23: Atomic displacement in bare $PbTiO_3$–$SrTiO_3$

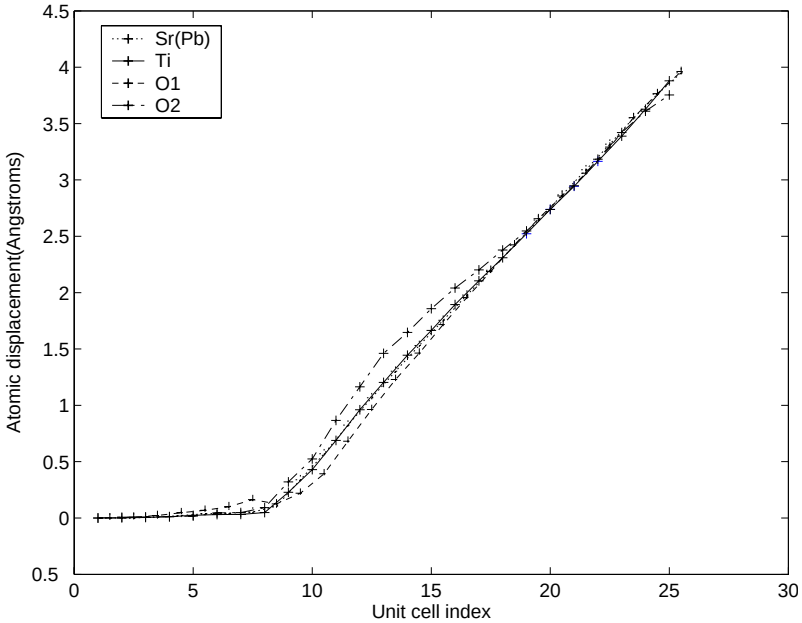

the substrate (Figures 4.15 and 4.23). The sublattice displacement starts in the immediate vicinity of the interface and reaches maximum at a distance of 4–5 unit cells and it vanishes toward the surface of the film. The O2 displacements are similar in both cases, the bare film and the film covered with the Pt electrode.

Two parameters were explored in the case of Ti atoms. The peak width for the two cases was compared in Figure 4.25(a). Widths were normalized to the corresponding value in the substrate. Their behavior does not seem to be influenced by the presence of the Pt electrode except in the regions corresponding to the substrate–film interface and film–vacuum interface, where the width corresponding to the bare film is slightly larger. This modification can be explained by the fact that Pt electrode inhibits the existence of the surface charge induced by the polarization.

The position of the Ti, measured with respect to the Pb sublattice, is slightly different also. The spacing between the Pb and Ti atoms is constant in the case of the Pt covered film. In the case of the bare film, the Ti atoms are slightly displaced away from the substrate, with a maximum of 0.07 Å approximately 9 UC away from the substrate (Figure 4.25(b)).

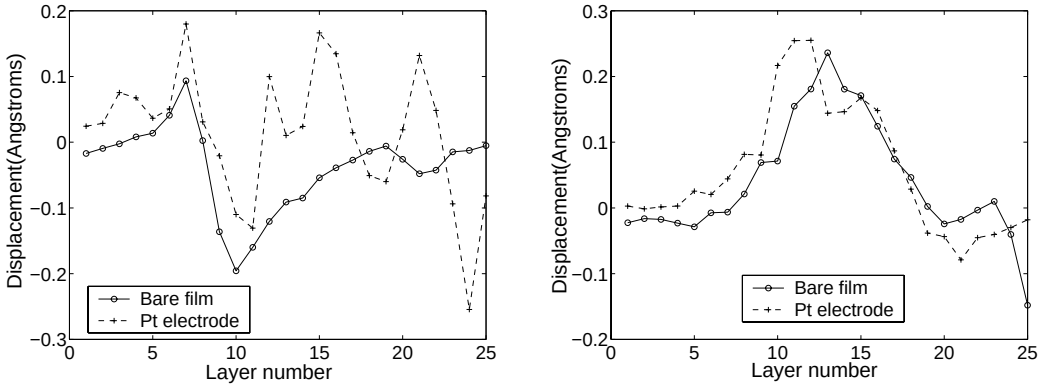

(a) O1 displacement

(b) O2 displacement

Figure 4.24: Oxygen atom displacement in the case of bare and Pt covered $PbTiO_3$ film

In both cases, the O1 and O2 peaks corresponding to the film region in the vicinity of the interface with the substrate suffer a significant broadening.

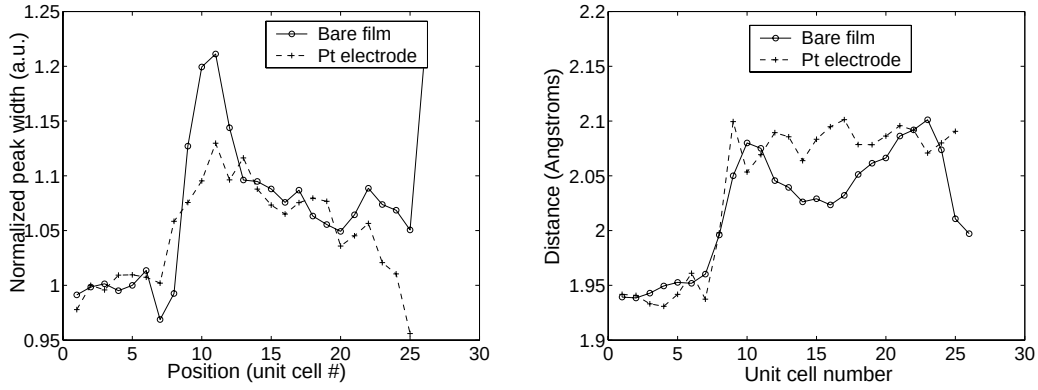

(a) Ti peak width

(b) Ti–Pb distance

Figure 4.25: Ti behavior in the bare and Pt covered film

The width behavior cannot be completely attributed to the substrate surface roughness since it is not consistent for O1, O2, Pb and Ti. Therefore, we can conclude that the increase in the width originates in the existence of regions in which the positions of the Ti (in both bare and electrode covered film), O (film region, in the vicinity of the interface with the substrate) and Pb (mostly in the case of the bare film) are different and, since the probing size is large, this is observed as an additional peak width. These regions are, most likely, domains in which the polarization has different orientation and values. In the bare region all atoms appear shift position–in different regions of the film–to accomodate the minimization of the energy and thus to participate in the formation of the domains. In the Pt region, the Pb atoms do not seem become split and thus only Ti and O atoms seem to be responsible for the domain formation.

An explanation for this behavior will consider the fact that the electrode provides mobile charge that gets redistributed to minimize the energy of the system

creating depolarization fields. A rigorous modelling will be, however, the job of the theoreticians.

CHAPTER V

Conclusions and Future Directions

In this study, two different crystallographic structures have been investigated. Coherent Bragg Rod Analysis (COBRA) was applied on epitaxial thin film samples with zincblende and perovskite structures and morphology distortions were observed. Hitherto unseen details of the interface structure, including ionic displacements, strains and structural distortions have been revealed by the new structure determination technique.

5.1 Advantages of the Method

The method is probably the only phasing reconstruction method that was reliably used for thin film characterization. It has been tested on ferroelectrics, semiconductors and there is an ongoing project attempting to use it for biological structural characterization.

No Sample Preparation Required

Like all x-ray scattering methods, the method is non destructive. It does not require any heavy atom substitutions, the crystal structure does not have to be altered chemically and the sample does not need to be subject to any special preparation procedures like in the case of the Transmission Electron Microscopy (TEM).

No Structural Information Required

The most important advantage is that COBRA is a direct method requiring no *a priori* knowledge of details of the structure other than the basic crystal structure of the substrate which is generally very well known.

The most common way to use the information provided by Bragg rod scattering is to fit the intensity profiles with a model. For the ferroelectric structure, the electron density (ED) peaks can be shifted significantly from the corresponding bulk position. Also, the electron density peaks can suffer broadening and become split. The lattice constant and the chemical composition can change significantly from the nominal values. In addition, the surface roughness alters the occupancy of the uppermost atomic layers. Thus, the number of variables required to fully describe a real interfacial structure can be quite large and unwieldy. And practice tells us that it is difficult to obtain convergence for a model involving a large number of variables.

In comparison to that, the Coherent Bragg Rod Analysis does not require any initial guess regarding the investigated structure. The COBRA *ansatz* involved requires only rough estimates of parameters (roughness, crystal symmetry) that can be provided by the grower or by conventional x-ray diffraction studies. The less knowledge we have about the structure, the more useful the method is. Since the output of the method is the true three–dimensional electron density (ED) of the sample, it is easy to explore the structure along different directions and represent the ED as a

Table 5.1: Minimum feature size resolvable

	direction	Q_{max} (RLU)	Min. feature size
semiconductor	vertical	5.5	$\sim 0.55\,\mathring{A}$
	in–plane	4	$\sim 0.75\,\mathring{A}$
ferroelectric	vertical	3.5	$0.558\,\mathring{A}$
	in–plane	3	$0.651\,\mathring{A}$

map on any chosen plane.

High Resolution

Two parameters describe the resolution of the method. The first one is the minimum feature size resolvable by the method. It has the value of $\frac{a}{2\,Q_{max}}$, where a is the lattice constant of the substrate and Q_{max} is the maximum value of the diffraction vector. Note that this parameter is different in different directions. The in–plane value is described by *no*–the maximum in–plane index (see Section 2.2.1)–and the vertical one by $Q_{z_{max}}$. The Table 5.1 shows the minimum resolvable feature size for the two types of systems investigated, for both in–plane and vertical directions.

The second parameter that is important when assessing the resolution of the method is sampling density of the final ED. The zero paddings increase its value allowing for a better location of the ED peaks.

The value of the in–plane data sampling density is given by $\frac{2\,M_{xy}\,no}{a}$, with a–the substrate lattice constant and M_{xy}–the lateral multiplication coefficient defined as the ratio of the in–plane reciprocal space extent before and after zero padding.

In the vertical direction, the data sampling density is given by $\frac{2\,M_z Q_{z_{max}}}{a}$. Table 5.2 summarizes the final ED sample densities for both cases, of the ferroelectric and semiconductor samples. The sampling density can be artificially increased by increasing the values of the multiplication factors M_{xy} and M_z. However, increasing the density will not provide additional information and creates significant demands for computing resources like memory and processor speed.

5.2 Weaknesses of the Method

As with any other structural characterization method, there are also significant limitations. A few, encountered by the author, will be listed below.

Sample Requirements

In order to be able to use the technique, the main requirement that the system to be investigated has to meet is the coherence (registry) with the substrate. If this requirement is not met, the interference between the film scattered wave and substrated scattered wave will be destroyed. This confines the systems that can be studied to epitaxial systems, in which there is a registry between the film and the substrate.

Roughness is a limiting factor. As the surface roughness increases, the intensity decay around the Bragg peaks becomes very steep. Because the dynamic range of the setup is, ultimately, finite–limited by the incident beam fluence, detector noise and quantum efficiency–the thin film sample must have a roughness as small as possible.

Thickness of the film determines the Bragg rod fringe density. Since the scanning density is finite due to goniometer finite resolution it limits the maximum film thickness that can be scanned.

All these requirements make the method applicable only to a certain type of samples. Nevertheless the class of materials is so important in modern technology that any technique that can provide atomic scale information is extremely useful and important.

When interpreting the results, one must keep in mind that COBRA has a large probing area, determined by the correlation length of a few microns [83] and the

Table 5.2: Final ED sampling density

	direction	Q_{max} (RLU)	M factor	Sample density
semiconductor	vertical	5.5	7	$\sim 12.8\,\mathring{A}^{-1}$
	in–plane	4	3	$\sim 4.0\,\mathring{A}^{-1}$
ferroelectric	vertical	3.5	7	$12.5\,\mathring{A}^{-1}$
	in–plane	3	3	$4.6\,\mathring{A}^{-1}$

angle of incidence.

X–ray Source not Widely Available

Since the intensity ratios between the Bragg peak values and the anti-Bragg peak values are very high (commonly 10^8–10^9), x–ray sources with fluences of the order of $\sim 10^{12}$ photons·s^{-1} are required. Unfortunately, this fluence can be achieved currently only by synchrotron sources. This type of source is not widely available and this prevents the method to become as routinely used as classical x–ray diffraction. However, many structural characterizations are routinely performed at synchrotron sources, so if the information required is important to obtain, use of synchrotron facilities is certainly justified, as exemplified by protein crystallography and its role in the pharmaceutical industry.

Measurement Difficulty

The method consists of a succession of procedures to be executed with very high precision. It is no exaggeration to say that, in order to acquire the data, the instruments–especially the goniometer–are being pushed close to their resolution limits.

The alignment procedures have to be followed religiously otherwise the acquisition path in the reciprocal space will fall off the Bragg rod. Therefore, a potential user needs significant training before beeing able to reliably use COBRA.

5.3 Technique Developments

Since the technique is new, there is a significant potential for improvement. Various stages need rigorous characterization and better understanding.

5.3.1 Characterization of Uncertainties

This is, perhaps, the most significant development to be done. The mathematical approach is not trivial. However, we can distinguish a few types of errors among which we can mention those induced by the limited resolution of the goniometer and the rest of the experimental apparatus, those induced by the imperfect outcome of the phasing procedure and the artifacts introduced by the sharp boundaries with the zero padding domains.

To eliminate these artifacts generated by the borders with the zero padding regions, one possible approach is to eliminate the artificial Debye-Waller factor completely and to replace the zero regions by gradually interpolating the measured regions to the calculated values. This will eliminate the sharp boundaries, particularly important in the case of semiconductors. Unfortunately, generating the required volume of the reciprocal space is very demanding from the computational point of view and this will be the first challenge of the development in this particular direction.

5.3.2 Convergence Study

Another important study for improving the procedure is to relate the convergence of the structure factor to the final solution with the convergence of the ED. It is reasonable to assume that the ED will converge to the real structure when the intensity corresponding to the structure factor converges to the measured intensity. The question that has to be answered is, what structural distortions correspond to given errors in measured data and, thus, in the structure factor.

5.3.3 Anomalous Scattering Bragg Rod Analysis

A way to improve the power of the method, especially in the case of materials using atoms with small differences in the atomic number, is to try to exploit the

anomalous dispersion. It is known that the atomic scattering factor varies a lot when the energy of incident beam is close to the binding energy of inner, completed electronic shells (the absorption edges). One way to exploit this phenomenon, widely used in other phase reconstruction techniques used for bulk crystals (see Section 1.2), is to acquire the Bragg rods with the incident beam energy set at two values for which the difference in scattering factors of the atoms to be separated is significant.

5.3.4 Hardware Developments

A few hardware developments can prove useful for the Bragg rod measurements required for this method. The most significant would be the replacement of the paddle and detector assembly with a linear detector array that will acquire the background and the signal simultaneously. This would reduce the acquisition time significantly as in the present setup the signal and the background are acquired sequentially.

An area detector would be an additional improvement, allowing the acquision of an interval in the reciprocal space, rather than a single point as done with the present setup.

5.4 Future Experiments

As far as ferroelectric samples are concerned, to fully understand their behavior in the presence of an interface, one experiment to be done is to measure the Bragg rods with an external electric field applied. Two sets of Bragg rods have to be acquired, one for every orientation of the field. The experiment would help understanding whether the interface has a polar or a ferroelectric behavior.

An obvious experiment would be to characterize the structural behavior as a function of the temperature. Structural data for the ferroelectric–paraelectric phase

transition would be a significant step for understanding the ferroelectricity of thin film materials. Our previous attempts at temperature measurements met with limited success due to inadequate in–situ heating equipment. An intrinsic difficulty to overcome in this experiment is given by the fact that the surface loses lead at temperatures $> 550°C$. Ideally, the experiment will be carried out in Pb vapor overpressure or the sample will have to be terminated with an amorphous or polycrystalline cap layer.

Another interesting development might result from considering the application of the method to neutron and electron diffraction.

Many experiments on semiconductor samples can be envisioned. This is probably going to be one of the most important applications of COBRA. Many heterostructures devices, such as High Electron Mobility Transistors (HEMTs) rely for their operation on a detailed knowledge of the interface structure. COBRA will be able to address the need directly and provide key information that can be used to improve the design and performance of heteroepitaxial electronic devices.

APPENDICES

APPENDIX A

Routines Used for COBRA Analysis

Once the data acquired, a series of MATLAB programs have to be executed in order to extract the desired structural information. The data is conditioned and corrected for the polarization effects. An iterative fit is performed next in order to find some parameters used to generate the *reference* structure. This structure is used next to generate a number of rods in the reciprocal space. An artificial Debye-Waller factor is applied to this structure and the data, followed by the phasing procedure.
A complete analysis requires the use of following routines, in the order mentioned: *data_clean.m*, *rod_fit.m*, *model3Dgen.m*, *abgg_spike_rem.m*, *art_DW.m*, *model_zFT.m*, *phaser.m* and *plane_2dFT.m*. The result of this sequence is a 3D electron density which can be displayed/analyzed using some additional routines: *surfer.m*, *plots.m*, *gauss_width.m*, *gauss_plot.m*.

A.1 Configuration Files

Each data set must be accompanied by a set of 3 files which contain specific information about the sample and the data set: *an_param.m*, *struct_param.m* and *bragg_data.m*. These files have to be modified for each particular case before proceeding any further with another analysis step as all of the routines will use parameters specified here. In addition to that, there is a file containing constants used in some

of the routines and functions, *constants.m*.

The parameters declared as *global* will be used in the function bodies as well.

A.1.1 bragg_data.m

This is the first of the three files that have to be specific for every experiment. It is basically the configuration file that contains information about the Bragg data. It contains a set of parameters which will be described individually.

c1-c18: Every scan is stored in a file and the first set of parameters indicate the meaning of the relevant columns: `c1`-the point index in the file; at the time being is not used; might be in future versions; `c2`-the value of Q_z; `c3`-the signal; `c4`-the total number of counts of the ion chamber during the time the signal was integrated (signal reference); `c5`-the background; `c6`-the total number of counts of the ion chamber during the time the background was integrated (background reference); `c7`-the total transmission of the filters used for the current data point.

str indicates the ratio between the signal integration time and the total integration time (signal + background). It has to be determined experimentally.

rods is an array containing the scan ID number–used by the program to build the file name–rod index and the orientation of the fixed axis for every scan.

ki is the incident beam vector.

data_dens is the number of points per reciprocal space unit along Q_z direction.

In the bottom part of the file a couple of other parameters (`Nrods`, `data_rods_index`-an internal index for the rods) are calculated; this part is not experiment specific and the user does not need to modify it.

A.1.2 struct_param.m

This file contains all the information about the structure of the sample. All the parameters specified here will be used in the calculation of the model.
It is worth mentioning that the program has the capability of dealing with different structures of the substrate and the film. In this particular case, the position of the film atoms in the *reduced unit cell* has to be defined (see Section 2.3 .

subs_pos is a matrix containing the atomic positions in the unit cell of the substrate. Each line, which represents an atom, has three columns corresponding to the *(x,y,z)* coordinates in the real space unit cell.

subs_els is a vector containing the number of the electrons for every atom in the unit cell. The atomic positions (`subs_pos`) and the Z-values (`subs_els`) have to be specified in the same order.

film_pos is a matrix containing the atomic positions in the unit cell or reduced unit cell, if the substrate and film have different unit cell structures of the film (see Section 2.3).

film_els is a vector containing the number of the electrons for the atoms in the film unit cell. Again, the atomic positions (`film_pos`) and the Z-values (`film_els`) have to be specified in the same order.

nsubs is the number of substrate unit cells, in vertical direction, that will be described explicitly when generating the model.

nfilm is basically the thickness of the film, in film unit cells (a film unit cell equals the substrate unit cell times the unit cell distortion, which will be described in detail in the next section).

sizeUC is the size of the substrate unit cells, in Å.

structure is a constant that specifies the structure type. It will be used mainly to determine the symmetry of the system and the allowed Bragg reflections. The possible values are: FCC, PEROSKITE, ZINCBLEND, CUBIC. These constant values are stored in *constants.m*; if the programs are to be used with a different structure the user must add a new value in the last mentioned file as well as modify the function *allowed_ref*.

occ_last_film is a vector describing the occupancy of the last unit cell. This vector is meant to help generate structures grown with different structures than an integer number of unit cells. Toward the end of the file a couple of other parameters (`nUCsub`-the number of atoms in the substrate unit cell, `nUCfilm`-the number of atoms in the substrate unit cell) are calculated based on the information contained in the previous variables since they will be quite often used in the analysis routines. Since they are not independent the user needs not modify them.

A.1.3 an_param.m

This file contains parameters that are specific to different operations done in the data analysis.

no is the maximum value for a rod index.

nAnalysis is the number of points per reciprocal space unit used for phasing, after interpolating the original data. It is used is *phaser.m*.

Lstart All rods are eventually represented as having the same length; `Lstart` is the Q_z start value. It is usually set to 1/`data_dens`-one sampling distance from the

plane $Q_z = 0$.

Lend is the Q_z end value of the rod, in the reciprocal space.

bgOffset is a value that is used to offset the signal in *FFT_data_filt* with the purpose to make sure that all data is positive; after filtration it is removed.

passRange is the pass value of the Hanning filter applied to the data in *FFT_data_filt*; it varies in the interval $[0, 1]$.

assx the in plane component of the artificial Debye-Waller factor applied to the data and model. It is measured in reciprocal space unit cells.

assz the out of plane component of the artificial Debye-Waller factor.

ner is the number of data points around the Bragg peaks to be excluded from the sum of squares used to evaluate the quality of the fit of the model with the measured data.

mfc is the start value for the multiplication constant that will be determined during the fitting procedure.

uc_dis is the start value for the ratio between the out of plane component of the film unit cell size and the substrate unit cell size.

zDW_subs_bulk is the start value for the out of plane component of the Debye-Waller factor of the bulk substrate. It is measured in reciprocal space unit cells.

xyDW_subs_bulk is the start value for the in plane component of the Debye-Waller factor of the bulk substrate. It is measured in reciprocal space unit cells.

DW_subs is the start value for the Debye-Waller factor of the explicit part of the substrate. Measured in reciprocal space unit cells.

DW_film is the start value for the Debye-Waller factor of the film. Measured, again, in reciprocal space unit cells.

interface2 is the start value for the number of film unit cells with less than one occupancy. Measured in unit cells.

occupancy_par is the start value for the parameter that describe the roughness (assumed gaussian). Measured in unit cells.

rodparam is a vector containing the start values for all the the fit parameters. Users have not to modify it.

rodparbits a vector of zeros and ones, indicating whether a parameter is to be varied or not.

LL is a scalar describing the extent of reciprocal space volume to be calculated at a time; the value is specific to the amount of memory of the system.

nsamp is the distance, in measured data points, between two consecutive point along the rod use for the phasing approximation (default value is 1).

pol_range is the number of points used for interpolation around each Bragg peak; used in *u_interp.m*.

pol_excl is the number of pixels to be excluded around the Bragg peaks; used in *u_interp.m*.

pol_deg is the degree of the polynom used for interpolation. used in *u_interp.m*.

u_passRange is the pass range of the Hanning filter applied to the structure factor component calculated by phasing. Used in *u_filt.m*.

ignored_left is the number of points ignored at the left of the Bragg point. Used in *u_filt.m*.

ignored_right is the number of points ignored at the right of the Bragg point. Used in *u_filt.m*.

mult_z is the coefficient used to determine the size of zero-padding along z direction.

mult_xy is the coefficient used to determine the size of zero-padding along xy direction.

z_bFT_start is the index of the start point of the significant region in the 3D electron density.

z_bFT_end is the index of the end point of the significant region in the 3D electron density.

no_displayed is the lateral number of unit cells explicitly considered in the final 3D electron density. Used in *surfer.m*.

mf_d is a multiplication factor used to artificially increase the density of points in the fit of the electron density. Used in *gauss_plot.m*.

colors is an arrays of strings used to specify the plot color. Used in *gauss_plot.m*

A.2 Routines for Data Analysis Itself

A.2.1 init_all.m

This file clears the MATLAB environment of all residual variables from previously executed routines. Also, loads the parameter files.

It is usually called in the beginning of every routine.

A.2.2 data_clean.m

The first step to be done is conditioning the data.

It is possible that data for a single rod was taken in multiple scans so the routine puts them all together. Then, the signal and the background are displayed separately and the user can correct the values of individual points selected with a cursor. In order to do that, the cursor horizontal position must correspond to the index of the point to be corrected and the vertical value-to the desired new value. After all the desired points have been corrected the user must hit return.

The incident x-ray beam is polarized in the horizontal plane and the signal have to be corrected for it. This step is done calling a dedicated function, *pol_correct*, which will be discussed in detail later in this chapter. The background is next subtracted and the result normalized for the attenuation and displayed on a logarithmic plot. The negative values have the sign swapped and are displayed in red; the user can correct them using, again, a cursor. Since the result is noisy, especially in the valleys between the Bragg peaks where the signal level is significantly reduced, a Hanning filter is applied. This is done using the function *FFT_data_filt*.

The result is displayed again and, using a cursor, one has the posibility of selecting intervals to be eliminated from the sum of squares. Next, the start point and the end point of the acquired rod can be selected.

The files and routines used:

- Input: The input is basically the acquired data, each scan in a separated file.

- Output: *data.dat* - contains all the rods, normalized and background corrected; *mask0.dat* - containing a mask of zeros and ones that keeps track of the position

of the Bragg peaks (that will be eliminated from the sum of squares along with an area around them) and the limits of the data; *mask1.dat* - another mask of zeros and ones keeping track of the data intervals to be eliminated from the fit; *limits.dat* - file that contains the index for first and the last point of every rod.

- Functions called: *FFT_data_filt* - used for filtering; *pol_correct* - to correct for polarization effects.

A.2.3 rod_fit.m

Is the routine used to fit the Bragg rods of the reference structure with the acquired data using the function *rod_calc*. The routine can use, as start values, the parameters saved in *an_param* or results from previous fits, saved in *vpr.dat*. Also, the routine can generate the structure factor without performing the fit and using the initial conditions instead. A maximum number of 400 iterations is performed for every execution. During the fit only the parameters corresponding to unit values in *rodparbit* are varied; the sum of squares of the differences between the data and generated rods is minimized using *sq_sum*. A typical fit involves multiple executions of this routines with different values in *rodparbit*.

The files and routines used:

- Input: The file with previous fit parameters, *vpr.dat*; the file containing the measured rods, *data.dat*.

- Output: There are two outputs files containing the real and imaginary party of the structure part of the film and explicit part of the substrate (the *reference*) - *svtr0.dat*, *svti0.dat* - and one containing the parameters that give the best fit, *vpr.dat*.

- Functions called: *rod_calc* - to generate the model; *sq_sum* - to calculate the sum of squares.

A.2.4 model3Dgen.m

In this routine all the rods with indices in the interval $[-no, no]$ are generated using the parameters saved in the last execution of *rod_fit*. All the rods are calculated in the function *rod_calc_all*.
The files and routines used:

- Input: *vpr.dat* - the results of the fit.

- Output: *model_r0.dat*, *model_i0.dat* - containing the real and imaginary party of the structure part of the film and explicit part of the substrate (the *reference*); *model_bulk_r0.dat*, *model_bulk_i0.dat* - containing the real and imaginary part of the structure factor of the bulk substrate without the explicit part ;

- Functions called: *rod_calc_all* - to calculate all the rods.

A.2.5 abgg_spike_rem.m

Because the unit cell gets incomplete due to roughness, peaks might occur at anti-Bragg points - especially in FCC type structures. They are removed and the region around them interpolated.

- Input: *svtr0.dat*, *svti0.dat* - containing the structure factor along the measured rods; *model_r0.dat*, *model_i0.dat* - structure factor of the *reference* along all rods;

- Output: *svtr0.dat*, *svti0.dat*; *model_r0.dat*, *model_i0.dat*;

A.2.6 art_DW.m

In this part, an artificial Debye-Waller factor is applied to the measured rods and the rods calculated from the reference structure. The in-plane component and the out-of-plane components are, in general, different and given by the parameters `assx` and `assz`. The files are loaded, a Debye-Waller matrix calculated and then applied. The files and routines used:

- Input: *svtr0.dat*, *svti0.dat* - containing the structure factor along the measured rods; *model_r0.dat*, *model_i0.dat* - structure factor of the *reference* along all rods; *model_bulk_r0.dat*, *model_bulk_i0.dat* - structure factor of the bulk substrate along all rods; *data.dat* - the data.

- Output: *svtr.dat*, *svti.dat*, *model_r.dat*, *model_i.dat*, *model_bulk_r.dat*, *model_bulk_i.dat*, *data_DW.dat* - same quantities with Debye-Waller on; *edsv.dat* - the Debye-Waller factor for the rod indices for which data has been acquired.

A.2.7 model_zFT.m

Takes the Fourier transform of all the rods with indices in interval $[-no, no]$.
The files and routines used:

- Input: *model_r.dat*, *model_i.dat* - real and imaginary components of structure factor for all the rods.

- Output: *bfmr.dat*, *bfmi.dat* -real and imaginary part of the 1d inverse Fourier transform of the structure factor along the out of plane direction; *sitr.dat*, *siti.dat* -real and imaginary part of the structure factor of the substrate.

A.2.8 phaser.m

The phasing procedure is performed in this part. The data rods are brought all at the same length using a progressive extrapolation to the intensity of the calculated structure. Next, both data and the structure factor of the model are loaded. They might be resampled at a different density.

The files and routines used:

- Input: *limits.dat* - containing the indices of the first and the last experimental data point in the rod; *data_DW.dat* - contains the data with the DW factor on; *svtr.dat*, *svti.dat* - the real and imaginary part of the structure factor of the *reference* for the measured rods.

- Output: *ndata.dat* - file with all the data rods at the same length; *udr.dat*, *udr.dat* - the real and imaginary part of the unknown term determined by phasing; *svtrt.dat*, *svtit.dat* - the real and imaginary part of the total structure factor, the structure factor of the *reference* summed with the term found by phasing: $svtrt = svtr + udr$, $svtit = svti + udi$; *bfor.dat*, *bfoi.dat* - the real and imaginary part of the 1d inverse Fourier transform of the phasing term of the structure factor; *bftr.dat*, *bfti.dat* - the real and imaginary part of the 1d inverse Fourier transform of the total (reference + phasing) structure factor;

- Subroutines called: *l_adjust.m* - used to bring all rods at the same length; *u_filt* - used to filter the high frequency components in the structure factor term determined with phasing; *u_interp* - used to interpolate the phasing term in the regions around the Bragg peaks; *u_zFT* - used to use copy the phasing term in symmetry equivalent positions and generate the Fourier transform along the rods.

A.2.9 plane_2dFT.m

This routine completes the transformation of the complex structure factor to the electron density. It takes the inverse 2D Fourier transform, in the Q_x–Q_y plane, of the results of the 1d inverse Fourier transform-along the Q_z direction-of the total (reference + phasing) structure factor along the Bragg rods. The files and routines used:

- Input: *bfmr.dat*, *bfmi.dat* - the real and imaginary part of the 1d inverse Fourier transform of the *reference* structure factor; *bftr.dat*, *bfti.dat* - the real and imaginary part of the 1d inverse Fourier transform of the total (reference + phasing) structure factor;

- Output: *bfcr1.dat*, *bfci1.dat* - real and imaginary part of the electron density of the explicit part of the substrate and the film with a density factor of 1 (The parameter that describes what area will be padded with zeros before the 2d inverse Fourier transform). Although the electron density is a real quantity, the 2d inverse Fourier transform may return a small imaginary part; *bfcr.dat*, *bfci.dat* - real and imaginary part of the electron density of the explicit part of the substrate and the film with a density factor greater than 1;

A.2.10 nzmft.m

The routine has the capability of setting to zero all the negative parts of the electron density with unity density factor and takes the 2d Fourier transform of the electron density. It must be be run before *remodel.m*.
The files and routines used:

- Input: *bfcr1.dat*, *bfci1.dat* - real and imaginary part of the electron density of the explicit part of the substrate and the film with a density factor of 1;

- Output: *bfzr.dat*, *bfzi.dat* - the real and imaginary part of the 2d Fourier transform of the total electron density.

A.2.11 remodel.m

This routine opens the possibility of executing the phasing procedure more than once; what it does, it sums up the structure factor of the reference and the term found by phasing and saves the result as the new *reference*. Then, the 1d inverse Fourier transform is applied to get *bfmr.dat*, *bfmi.dat* - which will be used in reconstructing the total electron density after a new phasing procedure. Once this routine is applied, the old structure factor of the *reference* is lost, this is why it might be a good idea to create a new folder for the analysis using the new model.
The files and routines used:

- Input: *bfzr.dat*, *bfzi.dat* - ;*sitr.dat*, *siti.dat* - the real and imaginary part of the bulk substrate without the explicit part;

- Output: *svtrt.dat*, *svtit.dat* - the real and imaginary part of the total structure factor of the explicit part of the substrate and the film for the rods measured; *svtr.dat*, *svti.dat* - the real and imaginary part of of the explicit part of the substrate and the film for the rods measured (Since the *reference* has been redefined based on the results of the phasing procedure, the total structure factor and the structure factor of the *reference* are equal); *bfmr.dat*, *bfmi.dat* - the real and imaginary part of the 1d inverse Fourier transform of the new *reference* structure factor.

A.3 Routines Used to Display the Data

A.3.1 rod_simulate.m

Routine used to calculate the structure factor along a rod. The user is prompted to choose between the default values of the model stored in *an_param* and the stored values of the last fit stored in *vpr.dat*. Also, the user must introduce the indices u and v of the rod to be calculated.

The files and routines used:

- Input: *vpr.dat* - stored parameters of the model after the fit.

A.3.2 surfer.m

The routine is used to analyze and display the resultant electron density. The initial step is to plot the total electron density (the central column in *bfmr.m*) to let user select an atomic plane. The next plot, showing the 2d electron density map in the selected plane, offers the capability to select a particular point in the plane which will be contained by the subsequent selected plot. A few types of plots are available; *horizontal*, *vertical*, *rising*, *falling* are all plane sections through different directions in the electron density; X is a 1d out of plane profile of the electron density which can be saved in a data file for later processing.

The files and routines used:

- Input: *xf_image.dat* - the value of the density factor selected in *plane_2dFT*; *bftr.dat* - the real part of the 1d inverse Fourier transform of the total structure structure factor; *bfcr.dat*, *bfci.dat* - real and imaginary part of the electron density - calculated with density factor different than 1.

- Output: *zstr.dat* - contains the out of plane electron density profile through different points in the lattice.

A.3.3 plots.m

This routine plots the different terms of the structure factor and the data.
The files and routines used:

- Input: *svtro.dat*, *svtio.dat* - real and imaginary part of the reference *structure* factor along the measured rods without the Debye-Waller factor applied; *data.dat* - measured rods without the artificial Debye-Waller applied; *svtr.dat*, *svti.dat* - real and imaginary part of the reference *structure* factor along the measured rods with the Debye-Waller factor applied; *data_DW.dat* - measured rods with the artificial Debye-Waller applied; *ndata.dat* - data with artificial Debye-Waller factor on and rod ends extrapolated to the *reference*; *udr.dat*, *udi.dat* - the real and imaginary part of the phasing term of the structure factor.

A.3.4 gauss_width.m

This routine does a gaussian fit on the electron density profiles saved in *zstr.dat*. One needs first to select the desired peaks and next to specify a width used for fitting (it must not exceed the width of a single peak!). A set of 3 parameters will be saved for every peak: the real position, the amplitude and the width. Peaks are modeled as $amplitude \times e^{-\frac{(x-realposition)^2}{width^2}}$.
NOTE: MATLAB environment needs to have the Curve Fitting Toolbox installed to be able execute this routine
The files and routines used:

- Input: *xf_image.dat* - the value of the density factor selected in *plane_2dFT*; *bftr.dat* - the real part of the 1d inverse Fourier transform of the total structure structure factor; *bfcr.dat*, *bfci.dat* - real and imaginary part of the electron density - calculated with density factor different than 1.

- Output: file containing the gaussian fit parameters for all the peaks; the name is user-defined;.

A.3.5 gauss_plot.m

This routine builds a plot with the gaussians defined in *gauss_width.m*. The point density is increased with the factor `mf_d`. The colors of the plots are defined in `colors`.

The files and routines used:

- Input: the files containing the gaussian parameters.

- Output: file containing the generated gaussians.

A.4 Routines and Functions Indirectly Called in the Main Analysis

A.4.1 l_adjust.m

The measured rods have, quite often, different lengths which depend on the experimental conditions (wavelength, diffractometer geometry etc.). They all have to be brought at the same length defined by `Lstart` and `Lend`. This routine takes the measured data between the points specified (in *data_clean.m*) as the lower and upper end and then gradually extrapolates the remaining interval to the reference structure.

The files and routines used:

- Input: *svtr.dat*, *svti.dat* - real and imaginary part of the reference *structure* factor along the measured rods with the Debye-Waller factor applied; *data_DW.dat* - measured rods without the artificial Debye-Waller applied; *limits.dat* - file that contains the index for first and the last point of every rod.

- Output: *ndata.dat* - data with artificial Debye-Waller factor on and rod ends extrapolated to the *reference*;

A.4.2 u_interp.m

The phasing term might exhibit some discontinuities in the vicinity of the Bragg peaks. This routine eliminates those regions completely and replaces them with a polynomial interpolation.
The files and routines used:

- Input: *udr.dat*, *udi.dat* - real and imaginary part of the phasing term.

- Output: *udr.dat*, *udi.dat*.

- Functions called: *allowed_ref* - used to identify the Bragg peaks.

A.4.3 u_filt.m

The phasing term might exhibit some high frequency noise which can be easily removed using a Hanning filter. The routine moves from one Bragg point to another and applies the filter on the region between them.
The files and routines used:

- Input: *udr.dat*, *udi.dat* - real and imaginary part of the phasing term.

- Output: *udr.dat*, *udi.dat*.

- Functions called: *allowed_ref* - used to identify the Bragg peaks.

A.4.4 u_zFT.m

Routine that takes the 1d inverse Fourier transform of the unknown term of the structure factor determined by phasing.
The files and routines used:

- Input: *udr.dat*, *udi.dat* - real and imaginary part of the phasing term.

- Output: *bfor.dat*, *bfoi.dat* - real and imaginary part of the 1d inverse Fourier transform of the phasing term of the structure factor; *bftr.dat*, *bfti.dat* - real and imaginary part of the 1d inverse Fourier transform of the total (phasing + *reference*) of the structure factor;

- Functions called: *allowed_ref* - used to identify the Bragg peaks; *symm_per* - used to copy the phasing term in symmetry equivalent positions considering a PEROSKITE structure; *symm_zincblend* - used to copy the phasing term in symmetry equivalent positions considering a ZINCBLEND structure; *fill_u* in the case not all the symmetry independent rods with indices in the interval $[-no, no]$ have been measured it is possible to approximate them; this function gives an approximate of the phasing term for the the missing rods for each particular crystal type.

A.4.5 pol_correct.m

It is the function used to correct for polarization effects. It assumes the beam polarized horizontally.

complete form pol_correct(meas_signal, H, K, L, ki_v, faxis_v,uc).

meas_signal vector containing the rod part to be corrected.

H vector containing the corresponding values of Q_z.

K,L the rod indices.

ki_v incident beam vector.

faxis_v vector indicating the orientation of the fixed axis.

uc the size of the unit cell, in Å.

output vector, same size as the input $meas_signal$.

A.4.6 FFT_data_filt.m

Function used to apply the Hanning filter to the data. It moves from one Bragg point to another and filters the intervals in between.

complete form FFT_data_filt(inpt,minL,maxL,u,v).

inpt vector containing the rod (or part of the rod) to be filtered.

minL, maxL the start and end value of the corresponding Q_z.

u, v the rod indices, needed to identify the Bragg peaks.

output a vector of the same size as *inpt*.

Functions used *allowed_ref* to identify the Bragg peaks.

A.4.7 allowed_ref.m

It is a function that identify the Bragg peaks of the substrate.

complete form allowed_ref (H,K,L).

H,K,L the coordinates in the reciprocal space of the point we need to investigate.

output 1 if Bragg point, 0 otherwise.

A.4.8 sq_sum.m

It is a function that calculates the sum of squares of the difference between the measured rod and the rod of the *reference*. The parts of the rod that have been eliminated from the fit do not participate in the sum.

complete form sq_sum(xx, vpr).

xx vector containing the parameters to be varied during the fit in *rod_fit*.

vpr vector containing the all the parameters needed in the calculation of the *reference*.

output a real, positive number.

A.4.9 rod_calc.m

Function used to generate the structure factor of the *reference* along the rods measured.

complete form rod_calc(xpr, vpr).

xpr vector containing the parameters to be varied during the fit in *rod_fit*.

vpr vector containing the all the parameters needed in the calculation of the *reference*.

output is a $((Lend - Lstart)data\_dens + 1) \times N_{rods} \times 2$ matrix, where: $(Lend - Lstart)data\_dens + 1$ is the number of points along Q_z direction; N_{rods} is the number of measured rods; at index 1 of the last dimension is saved the structure factor of the film and explicit substrate; at index 2 - the structure factor of the bulk substrate minus the explicit part.

A.4.10 rod_calc_all.m

The function that calculates the structure factor along all the *reference* rods with indices in the interval $[-no, no]$.

complete form rod_calc_all(vpr).

vpr vector containing the all the parameters needed in the calculation of the *reference*.

output is a $(2Lend \times data\_dens + 1) \times (2no + 1)^2 \times 2$ matrix, where: $2Lend \times data\_dens + 1$ is the number of points along Q_z direction; $(2no + 1)^2$ is the total number of rods with indices in the interval $[-no, no]$; at index 1 of the last dimension is saved the structure factor of the film and explicit substrate; at index 2 - the structure factor of the bulk substrate minus the explicit part.

A.4.11 symm_per.m

A function that copy the phasing term in symmetry equivalent positions considering the system has a PEROSKITE structure.

complete form symm_per(input_vol,K,L, rod_value).

input_vol is a $(2Lend \times data\_dens + 1) \times (2no + 1)^2$ matrix, where: $2Lend \times data\_dens + 1$ is the total number of points along Q_z and $(2no + 1)^2$ is the total number of rods.

K,L the indices of the rod.

rod_value is a $(Lend - Lstart)data\_dens + 1$ vector that contains the phasing term to be copied in the symmetry equivalent positions.

output is a matrix of the same dimensions as *input_vol*.

A.4.12 symm_zincblend.m

A function that copy the phasing term in symmetry equivalent positions considering the system has a ZINCBLEND structure.

complete form symm_zincblend(input_vol,K,L, rod_value).

input_vol is a $(2Lend \times data\_dens + 1) \times (2no + 1)^2$ matrix, where: $2Lend \times data\_dens + 1$ is the total number of points along Q_z and $(2no + 1)^2$ is the total number of rods.

K,L the indices of the rod.

rod_value is a $(Lend - Lstart)data\_dens + 1$ vector that contains the phasing term to be copied in the symmetry equivalent positions.

output is a matrix of the same dimensions as *input_vol*.

A.4.13 fill_u.m

This function calculates the phasing term for the independent rods that have not been measured.

complete form fill_u(vol_in).

vol_in is a $(2Lend \times data\_dens + 1) \times (2no + 1)^2$ matrix, where: $2Lend \times data\_dens + 1$ is the total number of points along Q_z and $(2no + 1)^2$ is the total number of rods.

files used the function needs to load *vpr.dat* to get the Debye-Waller factors.

output is a matrix of the same dimensions as *vol_in*.

APPENDIX B

Goniometer Axis Determination for Kappa Geometry

B.1 Offsets and Positive Directions

In general, it is assumed that the goniometer axis represent a set of directions either perpendicular or parallel to each other (see axis definition on page 22). As it easily guessed, this assumption is true only to some extend. To turn the goniometer in a very precise navigation tool in the reciprocal space, the precise orientation of every axis needs to be known. The Generalized Goniometer Control (GGC) software allows the calculation of the position in the reciprocal space starting from the assumption that the goniometer axis have not the ideal orientation. The reasons for the difference from the ideal orientation are the imprecision in the zero position and, to a lesser extent, the imperfection in the mechanical execution.

To take full advantage of the feature in the GGC software first we need to precisely determine the orientation of the goniometer axis. First each motor has to be brought to a referece position chosen by the manufacturer as the *home* position. This is an arbitrary position on each axis chosen as a reference. To get the axis orientation to satisfy the definition on page 22, certain offset values have to be set followed by the definition of the positive direction. Both steps are completed adjusting the appropriate settings in EPICS, as described in Table B.1.

B.2 Autocollimator Mirror Alignment

First step is to set the autocollimator (AC) on the 2θ arm and the mirror on a goniometer head (GH) placed on ϕ axis, with all the goniometer angles set to zero. The procedure considers that all the axis point through the center of the goniometer (within a sphere of confusion that we will consider negligible) but their orientation is unknown. The ω axis is considered reference.

Next, the mirror has to be set perpendicular on the ω axis. To do that, the AC indication is brought to 0 using its adjustment screws. ω is rotated 180° and the AC indication is brought back to 0 in the following way: AC screws are adjusted until the deviation is brought to half and then GH adjusted to get to 0. After this, ω is rotated $-180°$ and the procedure repeated until the mirror and the AC are aligned.

B.3 Determination of the Orientation of ϕ Axis

With $\phi = 0°$, $\kappa = 0°$, $\omega = 0°$, $\psi = 0°$, $2\theta = -90°$ and $\nu = -90°$ the AC indication is observed, it should be very small.ϕ is rotated 180°. Next, 2θ and ν are adjusted until the AC indication is zero again on both directions. The precise orientation of ϕ axis is given by $A \times [1, \sin(\frac{(2\theta)_0+90°}{2}), -\sin(\frac{\nu_0+90°}{2})]$, with A the normalization constant and $2\theta_0$ and ν_0 the values that zero the indications of the autocollimator. This value should be recorded in the GGC.

Table B.1: Offsets and axis orientation for Kappa geometry

	ϕ	κ	ω	ψ	2θ	ν
offset	0°	0°	270°	−45°	90°	−45°
direction	−	−	−	+	−	+

B.4 Adjustment of the ν and 2θ Offsets

Once the mirror aligned perpendicular to the ω axis, the autocollimator has to be oriented perpendicular to the 2θ axis. To do that, the angles are set to $\phi = 0°$, $\kappa = 0°$, $\omega = 0°$,$\psi = 0°$, $2\theta = -90°$ and $\nu = -90°$. The AC orientation is tweaked until it is aligned with the mirror. Next, both ν and 2θ are set 90°. The Ac screws are adjusted until the deviation reduces to half. The offsets of ν and 2θ are next adjusted (keeping the values of 2θ and ν set to 90°) until the indication of the AC is brought back to zero.

B.5 Determination of the Orientation of κ Axis

Start from $\phi = 0°$, $\kappa = 0°$, $\omega = 0°$, $\psi = 0°$, $2\theta = -90°$ and $\nu = -90°$. At this orientation, the AC screws are adjusted until is aligned with the mirror. Set $\kappa = 179.99°$. Using *c02* pseudomotor in GGC (after setting the previous position as the reference), the detector arm has to be rotated around the direction of the κ axis with 180°. The orientation of the rotation axis is adjusted until the autocolimator indication is brought back to zero. At this point, the orientation of the rotation axis coincides with true κ axis.

APPENDIX C

Goniometer Axis Determination for Eulerian Geometry

C.1 Offsets and Positive Directions

The Generalized Goniometer Control (GGC) software used has the capability of dealing with goniometer axis that do not have the ideal orientation. In the case of Eulerian geometry, the goniometer used did not have the homing function implemented, making the imprecision in the zero axis position the main reason for their non-ideal behavior.

The Eulerian geometry is definitely the most straightforward goniometer configuration. The alignment steps are identical with those described in the case of Kappa geometry (Appendix B), the only difference given by the different orientation of χ axis with respect with κ in the previous case and some different axis nomenclature (θ instead of ω). For Eulerian geometry users the complete procedure will be described, in spite of the fact that some of the paragraphs will be redundant with the corresponding ones in Appendix B. The offsets and axis positive directions assumed by the reference system mentioned above involved the offsets and positive axis directions listed in Table C.1.

C.2 Autocollimator Mirror Alignment

First step is to set the autocollimator (AC) on the 2θ arm and the mirror on a goniometer head (GH) placed on ϕ axis, with all the goniometer angles set to zero. The procedure considers that all the axis point through the center of the goniometer (within a sphere of confusion that we will consider negligible) but their orientation is unknown. The θ axis is considered the reference.

Next, the mirror has to be set perpendicular on the θ axis. To do that, the AC indication is brought to 0 using its adjustment screws. *theta* is rotated 180° and the AC indication is brought back to 0 in the following way: AC screws are adjusted until the deviation is brought to half and then GH adjusted to get to 0. After this, θ is rotated $-180°$ and the procedure repeated until the mirror and the AC are aligned.

C.3 Determination of the Orientation of ϕ Axis

With $\phi = 0°$, $\chi = 0°$, $\theta = 0°$, $\psi = 0°$, $2\theta = -90°$ and $\nu = -90°$ the AC indication is observed, it should be very small.ϕ is rotated 180°. Next, 2θ and ν are adjusted until the AC indication is zero again on both directions. The precise orientation of ϕ axis is given by $A \times [1, \sin(\frac{(2\theta)_0+90°}{2}), -\sin(\frac{\nu_0+90°}{2})]$, with A the normalization constant and $2\theta_0$ and ν_0 the values that zero the indications of the autocollimator. This value should be recorded in the GGC.

Table C.1: Offsets and axis orientation for Eulerian geometry

	ϕ	χ	θ	ψ	2θ	ν
offset	0°	0°	0°	−45°	90°	−45°
direction	−	−	−	+	−	+

C.4 Adjustment of the ν and 2θ Offsets

Once the mirror aligned perpendicular to the ω axis, the autocollimator has to be oriented perpendicular to the 2θ axis. To do that, the angles are set to $\phi = 0°$, $\chi = 0°$, $\theta = 0°$,$\psi = 0°$, $2\theta = -90°$ and $\nu = -90°$. The AC orientation is tweaked until it is aligned with the mirror. Next, both ν and 2θ are set 90°. The Ac screws are adjusted until the deviation reduces to half. The offsets of ν and 2θ are next adjusted (keeping the values of 2θ and ν set to 90°) until the indication of the AC is brought back to zero.

C.5 Determination of the Orientation of χ Axis

Start from $\phi = 0°$, $\chi = 0°$, $\theta = 0°$, $\psi = 0°$, $2\theta = -90°$ and $\nu = -90°$. At this orientation, the AC screws are adjusted until is aligned with the mirror. Set $\chi = 180°$. Using *c02* pseudomotor in GGC (after setting the previous position as the reference), the detector arm has to be rotated around the direction of the χ axis with 180°. The orientation of the rotation axis is adjusted until the autocolimator indication is brought back to zero. At this point, the orientation of the rotation axis coincides with true χ axis.

BIBLIOGRAPHY

BIBLIOGRAPHY

[1] Online calculator at LBNL, www-cxro.lbl.gov.

[2] A. Thompson et al. *X-ray data booklet*. Technical and Electronic Information Department, Lawrence Berkeley National Laboratory, Berkeley, second edition, 2001.

[3] M.F.DeCamp et al. Coherent control of pulsed x-ray beams. *Nature*, 413:825–828, 2001.

[4] A.Cavalleri, C.Blome, and P.Forget et al. Femtosecond x-ray studies of photoinduced structural phase transitions. *Phase Transitions*, 75(7–8):769–777, 2002.

[5] D.K. Saldin, R.J. Harder, V.L. Shneerson, and W. Moritz. Phase retrieval methods for surface x-ray diffraction. *J. Phys.:Condens. Matter*, 13(47):10689–10707, 2001.

[6] J.D.Watson and F.H.C.Crick. A structure for Deoxyribose Nucleic Acid. *Nature*, 171(4536):737–738, 1953.

[7] D.Harker. The determination of the phases of the structure factors of non-centrosymmetric crystals by the method of double isomorphous replacement. *Acta Cryst.*, 9:1–9, 1956.

[8] R.M.Sweet. X-ray crystallography as an optical technique. Technical report, Biology Department, Brookhaven Nat'l Lab, Upton, NY11973, 2002.

[9] D.C.Hodgkin, J.Kamper, and J.Lindsey et al. The structure of vitamin B12.1. An outline of the crystallographic investigation of vitamin-B12. *P.Roy.Soc.Lond.B.Bio.*, 147(928):422, 1957.

[10] D.C.Hodgkin, J.Pickworth, and J.H. Robertson et al. The structure of vitamin B12.2 The crystal structure of a hexacarboxilic acid obtained by the degradation of vitamin-B12. *P.Roy.Soc.Lond.B.Bio.*, 150(941):590, 1959.

[11] D.C.Hodgkin, J.Kamper, and J.Lindsey et al. The structure of vitamin B12.1. An outline of the crystallographic investigation of vitamin-B12. *P.Roy.Soc.Lond.Ser.A*, 242(1229):228, 1957.

[12] D.C.Hodgkin, J.Pickworth, and J.H. Robertson et al. The structure of vitamin B12.2 The crystal structure of a hexacarboxilic acid obtained by the degradation of vitamin-B12. *P.Roy.Soc.Lond.Ser.A*, 251(1266):306–352, 1959.

[13] D.C.Hodgkin. The x-ray analysis of complicated molecules, 1964. Nobel Lecture.

[14] D.K. Saldin, R.J. Harder, and H.Vogler et al. Solving the structure completion problem in surface crystallography. *Comp.Phys.Com.*, 137:12–24, 2001.

[15] H.Hauptman. On integrating the techniques of direct methods and isomorphous replacement I. the theoretical basis. *Acta Cryst.*, A38:289–294, 1982.

[16] H.Hauptman, S. Potter, and C.M.Weeks. On integrating the techniques of direct methods with anomalous dispersion I. the theoretical basis. *Acta Cryst.*, A38:632–641, 1982.

[17] D.Gabor. A new microscopic principle. *Nature*, 161(4098):777, May 1948.

[18] A. Szöke. Holographic methods in x-ray crystallography. II. detailed theory and connection to other methods of crystallography. *Acta Cryst.*, A49:853–866, 1993.

[19] G.J.Maalouf, J.C.Hoch, and A.S.Stern et al. Holographic methods in x-ray crystallography. III. first numerical results. *Acta Cryst.*, A49:866, 1993.

[20] A. Szöke. Electron-diffraction spectroscopy and the holographic inverse problem. *Phys. Rev.B*, 47:14044–14048, 1993.

[21] K.Heinz, A.Seubert, and D.K. Saldin. Holographic low-energy electron diffraction. *J. Phys.:Condens. Matter*, 13(47):10647–10663, 2001.

[22] T.Gog, P.M.Len, and G.Materlik et al. Multiple-Energy X-Ray Holography: Atomic Images of Hematite (Fe_2O_3. *Phys.Rev.Lett.*, 76(17):3132–3135, 1996.

[23] M. Tegze and G.Faigel. X-ray holography with atomic resolution. *Nature*, 380:49–51, 1996.

[24] M. Tegze and G.Faigel. X-ray holography: theory and experiment. *J.Phys.: Condens.Matter*, 13:10613–10623, 2001.

[25] M. Tegze, G.Faigel, and S.Marchesini et al. Imaging light atoms by x-ray holography. *Nature*, 407:38, 2000.

[26] H.Winick. *Synchrotron Radiation Research*, chapter Chapter 2: Properties of Synchrotron Radiation, pages 11–25. Plenum Press, NewYork, 1980.

[27] G.Rosenbau, K.C.Homes, and J.Witz. Synchrotron radiation as a source for x-ray diffraction. *Nature*, 230(5294):434, 1971.

[28] R.Clarke. *Encyclopedia of Modern Optics*, chapter Synchrotron Sources. Elsevier, 2004.

[29] A.Subramanian L.D.Marks, N.Erdman. Crystallographic direct methods for surfaces. *J.Phys: Condens. Matter*, 13:10677–10688, 2001.

[30] B.D. Cullity and S.R. Stock. *X-ray diffraction*. Prentice Hall, New Jersey, third edition, 2001.

[31] I.K.Robinson. Crystal truncation rods and surface roughness. *Phys.Rev.B*, 33:3830–3836, 1985.

[32] I.K.Robinson and D.J.Tweet. Surface x-ray diffraction. *Rep.Prog.Phys*, 55:599–651, 1992.

[33] Y.Yacoby, R.Pindak, R.MacHarrie, L.Pfeiffer, L.Berman, and R.Clarke. Direct structure determination of systems with two-dimensional periodicity. *J.Phys:Condens.Matter*, 12:3929–3938, 2001.

[34] Y.Yacoby et al. Direct determination of epitaxial interface structure in Gd_2O_3 passivation layer of GaAs. *Nature Mat.*, 1:99–101, 2002.

[35] M.Sowwan et al. Direct atomic structure determination of epitaxially grown films: Gd_2O_3 on GaAs (100). *Phys.Rev.B*, 66:205311, 2002.

[36] D.D.Fong, C.Cionca, and Y.Yacoby et al. Direct structure determination in ultrathin ferroelectric films. Submitted for publication to Phys.Rev.B.

[37] M.Sowwan. *Investigation of solid-solid interface structure using a novel X-ray diffraction method*. PhD thesis, Hebrew University, 2002.

[38] E.Vlieg. Integrated intensities using a six–circle surface x-ray diffractometer. *J.Appl.Cryst*, 30:532–543, 1997.

[39] J.G.Proakis and D.Manolakis. *Digital Signal Processing*. Prentice Hall, Englewood Cliffs, NJ, third edition, 1996.

[40] B.L.Henke, E.M.Gullison, and J.C.Davis. X-ray Interactions: Photoabsorption, Scattering, Transmission and Reflection at E=50–30,000eV, Z=1–92 . *Atomic Data and Nuclear Data Tables*, 54(2):181–342, 1993.

[41] E.Vlieg. ROD: a program for surface X-ray crystallography. *J.Appl.Cryst.*, 33:401–405, 2000.

[42] D.Barker and S.Lewis. Epics tutorial, 1998. TJNAF and LBNL.

[43] D.A.Walko. Basic spec commands for a diffraction experiment. Technical report, MHATT-CAT, Advanced Photon Source, ANL, Argonne, IL 60439, 2003.

[44] D.A.Walko. Very basic spec commands. Technical report, MHATT-CAT, Advanced Photon Source, ANL, Argonne, IL 60439, 2003.

[45] Certified Scientific Software. Technical report, Cambridge, MA.

[46] Y.Yacoby, D.A.Walko, and D.Brewe et al. Diffractometer-Control Software For Bragg-Rod Measurements. In *AIP Conference Proceedings*, volume 705, pages 1221–1224, May 2004.

[47] W.R. Busing and H.A. Levy. Angle calculations for 3- and 4- circle x-ray and neutron diffractometers. *Acta Cryst.*, 22(4):457, 1967.

[48] I.K.Robinson. Four-circle diffractometry for surfaces. *Rev.Sci.Instrum.*, 60(7):1541, 1989.

[49] M.Lohmeier and E.Vlieg. Angle calculations for a six-circle surface x-ray diffractometer. *J.Appl.Cryst*, 26:706, 1993.

[50] S.G.J.Mochrie. Four-circle angle calculations for surface diffraction. *J.Appl.Cryst*, 21:1–3, 1987.

[51] P. Roblin, R.C. Potter, and A. Fathimulla. Interface roughness scattering in AlAs/InGaAs resonant tunneling diodes with an InAs subwell. *J. Appl. Phys.*, 79(5):2502, 1996.

[52] M.S. Daly, D.M. Symons, M. Lakrimi, R.J. Nicholas, N.J. Mason, and P.J. Walker. Interface composition dependence of the band offset in InAs/GaSb. *Semicond. Sci. Technol*, 11(5):823–826, 1996.

[53] S.M.Sze. *Physics of Semiconductor Devices*. John Wiley, New York, second edition, 1981.

[54] R.H. Miles, D.H. Chow, Y.H. Zhang, P.D. Brewer, and R.G. Wilson. Midwave infrared stimulated emission from a GaInSb/InAs superlattice. *Appl. Phys. Lett.*, 66(15):1921, 1995.

[55] G.B. Stringfellow and P.E. Greene. Calculation of III-V ternary phase diagrams: In-Ga-As and In-As-Sb. *J. Phys. Chem. Solids*, 30(7):1779–1791, 1969.

[56] R Magri and A Zunger. Effects of interfacial segregation and intermixing on the electronic properties of InAs/GaSb. *Phys. Rev. B*, 65(16):165302, 2002.

[57] R.M.Feenstra, D.A. Collins, and T.C.McGill. Scanning tunneling microscopy of InAs/GaSb superlattices with various growth conditions. *Superlat. and Microstr*, 15(2):215, 1994.

[58] B.Z. Nosho, W.Barvosa-Carter, M.J. Yang, B.R.Bennet, and L.J. Whitman. Interpreting interfacial structure in cross-sectional STM images of III-V semiconductor heterostructures. *Surface Science*, 465(3):361–371, 2000.

[59] J. Steinshnider, J. Harper, M. Weimer, C.H. Lin, S.S. Pei, and D. H. Chow. Origin of antimony segregation in GaInSb/InAs strained-layer superlattices. *Phys. Rev. Lett*, 85(21):4562, 2000.

[60] O.Dehaese, X.Wallart, and F.Mollot. Kinetic model of element III segregation during molecular beam epitaxy of III–III'–V semiconductor compounds. *Appl.Phys.Lett*, 71(1):52–54, 1995.

[61] I.P.Batra, P.Wurfel, and B.D.Silverman. Phase–transition, stability and depolarisation field in ferroelectric thin–film. *Phys.Rev.B*, 8(7):3257–3265, 1973.

[62] J.F.Scott. *Ferroelectric Memories*. Springer–Verlag, Berlin, 2000.

[63] P.Muralt. Ferroelectric thin films for micro–sensors and actuators: a review. *J.Micromech.Microeng.*, 10:136–146, 2000.

[64] K.Wasa, Y.Haneda, and T.Sato. Basic sputtering process and ferroelectric properties of single–domain single–crystal thin films of $PbTiO_3$. *Int.Ferroel.*, 21:451–460, 1998.

[65] M.V.Ramana Murty, S.K.Streiffer, and G.B.Stephenson et al. *In situ* x-ray scattering study of $PbTiO_3$ chemical–vapor deposition. *Appl.Phys.Lett*, 80:1809–1811, 2002.

[66] M.J.Bedzyk, A.Kazimirov, and D.L.Marasco et al. Probing the polarity of ferroelectric thin films with x-ray standing waves. *Phys.Rev.B*, 61(12):R7873, 2000.

[67] J.Junquera and P.Ghosez. Critical thickness for ferroelectricity in perovskite ultrathin films. *Nature*, 422:506–509, 2003.

[68] G.B.Stephenson, D.D.Fong, and M.V.Ramana Murty et al. In situ x-ray studies of vapor phase epitaxy of $PbTiO_3$. *Physica B*, 336:81–89, 2003.

[69] S.K.Streiffer, J.A.Eastman, and D.D.Fong et al. Observation of Nanoscale 180° Stripe Domains in Ferroelectric $PbTiO_3$ Thin Films. *Phys.Rev.Lett*, 89(6):067601, 2002.

[70] C.Thompson, C.M.Foster, and J.A.Eastman et al. Observation of the polarisation of domains in ferroelectric thin films using x-ray interference. *Appl.Phys.Lett*, 71(24):3516–3518, 1997.

[71] D.D.Fong, G.B.Stephenson, and S.K.Streiffer. Ferroelectricity in Ultrathin Perovskite Films. *Science*, 304:1650–1653, 2004.

[72] P.Ghosez and K.M.Rabe. Microscopic model of ferroelectricity in stress–free $PbTiO_3$ ultrathin films. *Appl.Phys.Lett*, 76(19):2767–2769, 2000.

[73] B.Meyer and D.Vanderbilt. *Ab initio* study of $BaTiO_3$ and $PbTiO_3$ surfaces in external electric fields. *Phys.Rev.B*, 63:205426, 2001.

[74] N.A.Pertsev, A.G.Zembilgotov, and A.K.Tagantsev. Effect of mechanical boundary conditions on phase diagrams of epitaxial ferroelectric thin films. *Phys.Rev.Lett*, 80(9):1988–1991, 1998.

[75] R.Kretschmer and K.Binder. Surface effects on phase transitions in ferroelectrics and dipolar magnets. *Phys.Rev.B*, 20(3):1065–1076, 1979.

[76] R.Ramesh and D.G.Schlom. Orienting ferroelectric films. *Science*, 296:1975, 2002.

[77] D.A.Walko. MHATT-CAT's Newport Kappa Diffractometer. Technical report, MHATT-CAT, Advanced Photon Source, ANL, Argonne, IL 60439, 2003.

[78] G.Shirane, R.Pepinsky, and B.C.Frazer. X-ray and Neutron Diffraction Study of Ferroelectric $PbTiO_3$. *Acta Cryst.*, 9:131–140, 1956.

[79] R.J.Francis, S.C.Moss, and A.J.Jacobson. X-ray truncation rod analysis of the reversible temperaturedependent [001] surface structure of $LaAlO_3$. *Phys.Rev.B*, 64:235425, 2001.

[80] Z.W.Hu, P.A.Thomas, and W.P.Risk. Studies of periodic ferroelectric domains in $KTiOPO_4$ using high–resolution x–ray scattering and diffraction imaging. *Phys.Rev.B*, 59(22):14259, 1999.

[81] C.H.Ahn, K.M.Rabe, and J.M.Triscone. Ferroelectricity at the Nanoscale: Local polarization in Oxide Thin Films and Heterostructures. *Science*, 303:488–491, 2004.

[82] E.T.Jaynes. Displacement of oxygen in $BaTiO_3$. *Phys.Rev.*, 79(6):1008–1009, 1950.

[83] I.A.Vartanyants. Partial coherence effects on the imaging of small crystals using x-ray diffraction. *J.Phys: Condens. Matter*, 13:10593–10611, 2001.

ABSTRACT

Imaging Interfaces in Epitaxial Heterostructures

by

Codrin N. Cionca

Chair: Roy Clarke

We present high resolution electron density maps of two types of systems investigated. The first type consists of two InAs films grown on GaSb (001) substrates (one grown using As_4, the other one grown using As_2) and two GaSb films grown on InAs (001). The semiconductor samples were 9 monolayers thick and were grown using MBE. The three dimensional electron densities were obtained measuring the intensities along the Bragg rods and analyzing them with the newly developed Coherent Bragg Rod Analysis (COBRA) phase retrieval method. The study represents the first attempt to use a phase retrieval method in the characterization of a buried semiconductor heterostructure. The semiconductor was treated as a quaternary of form $Ga_mIn_{1-m}As_nSb_{1-n}$.

The $m(z)$ and $n(z)$ compositional fractions and the vertical lattice spacing profiles were extracted. The results tend to indicate that the transition regions have a quaternary composition and are relatively narrow (1.5 unit cells). In the case of the GaSb film, significant presence of As is observed. The lattice constant in the film is

not constant and has a minimum ~ 1.5 unit cells below the surface.

The second type of system investigated consists of a thin film of $PbTiO_3$ on $SrTiO_3$ (001), with and without a Pt electrode on top. The 50 Å thick $PbTiO_3$ film was grown by sputtering. The ED maps were investigated for peak position shifts. The O1 lattice seems to be shifted toward the film substrate interface in the case of the bare film. In the case of the Pt electrode region, its behavior is more complex. The O2 sublattice exhibits a shift toward the surface of the film, with a maximum of ~ 0.25 Å at 12 unit cells away from the substrate. The effect relaxes toward the surface. In the case of the bare film, the Ti peak width is slightly increased in the vicinity of both film interfaces. The presence of the Pt electrode seems to inhibit this behavior, fact that can be correlated with the inhibition of the presence of surface charge.